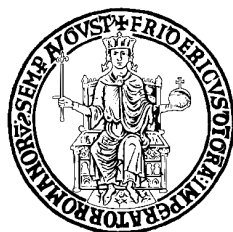


**UNIVERSITY OF NAPLES FEDERICO II**

Polytechnic and Basic Sciences School

Ph.D. School in Chemical Sciences



**FUNCTIONALIZATION OF PROTEIN  
CRYSTALS WITH METAL COMPLEXES**

Domenico Loreto

**Advisors:**

Prof Antonello Merlino

**Examiner:**

Prof Angela Lombardi

**XXXV Cycle**

2019/2022

## ABBREVIATIONS

ArM = artificial metalloenzyme.

bpy = bipyridine.

C $\alpha$  rmsd = root mean square deviation of C $\alpha$  atom position.

CD = circular dichroism.

CL = cross-linked.

CL\_Rh/RNase A = cross-linked [Rh<sub>2</sub>(OAc)<sub>4</sub>]/RNase A adduct crystals.

CLPCs = cross-linked protein crystals.

Cyt C = horse heart cytochrome C.

DFT = density functional theory.

DMSO = dimethyl sulfoxide.

ESI-MS = electrospray ionisation-mass spectrometry.

ECP = effective core potential.

GA = glutaraldehyde.

GC-MS = gas chromatography-mass spectrometry.

HEPES = 2-[4-(2-hydroxyethyl)piperazin-1-yl]ethanesulfonic acid.

HEWL = hen egg white lysozyme.

HOMO = highest occupied molecular orbital.

HSA = human serum albumin.

Im = imidazole.

ICP-OES = inductively coupled plasma-optical emission spectroscopy.

LUMO = lowest unoccupied molecular orbital.

MD = molecular dynamic.

OAc = acetate ion.

PCM = polarizable continuum model.

PDB = protein data bank.

PEG 4K = polyethylene glycol 4000.

POP = prolyl oligopeptidase.

RNase A = bovine pancreatic ribonuclease.

tfa = trifluoroacetate ion.

TFA = trifluoroacetic acid.

$t_R$  = retention time.

UV-vis = UV-visible.

<i>ABBREVIATIONS</i>	2
<i>1. ABSTRACT</i>	9
<i>2. INTRODUCTION</i>	12
2.1. Dimetallic complexes .....	12
2.2. Dirhodium paddlewheel complexes.....	15
2.3. Dirhodium tetracarboxylates: synthesis and reactivity.....	18
2.4. Dirhodium tetracarboxylates: applications.....	20
2.5. Interaction of metal compounds with proteins .....	23
2.6. Interaction of dirhodium tetracarboxylates with proteins.....	25
2.7. Crystals of metal/protein adducts .....	29
2.8. Cross-linked protein crystals (CLPCs) .....	32
2.9. Preparation of CLPCs.....	33
2.10. Glutaraldehyde: a milestone for preparation of CLPCs.....	35
2.11. CLPCs properties and application .....	37
<i>3. AIM OF THE THESIS</i>	40
<i>4. RESULTS AND DISCUSSION</i>	42
4.1. Crystallization of the adducts formed upon reaction of [ $\text{Rh}_2(\text{OAc})_4$ ] with HEWL.....	42
4.2. X-ray structures of the [ $\text{Rh}_2(\text{OAc})_4$ ]/HEWL adducts prepared by cocrystallization.....	42
4.3. X-ray structures of the [ $\text{Rh}_2(\text{OAc})_4$ ]/HEWL adducts prepared by soaking.....	50
4.4. Comparison of the [ $\text{Rh}_2(\text{OAc})_4$ ]/HEWL adducts with literature data .....	52
4.5. Spectroscopic analysis of the interaction of [ $\text{Rh}_2(\text{OAc})_4$ ] with HEWL.....	55
4.6. Summary of the [ $\text{Rh}_2(\text{OAc})_4$ ]/HEWL adduct features .....	57

4.7.	Interaction of <i>cis</i> -[Rh <sub>2</sub> (OAc) <sub>2</sub> (tfa) <sub>2</sub> ] with model proteins .....	58
4.8.	Synthesis and NMR characterization of <i>cis</i> -[Rh <sub>2</sub> (OAc) <sub>2</sub> (tfa) <sub>2</sub> ] ...	59
4.9.	Stability of <i>cis</i> -[Rh <sub>2</sub> (OAc) <sub>2</sub> (tfa) <sub>2</sub> ] in aqueous medium and in solution reactivity with RNase A and HEWL .....	59
4.10.	X-ray structures of the <i>cis</i> -[Rh <sub>2</sub> (OAc) <sub>2</sub> (tfa) <sub>2</sub> ]/RNase A adducts . .....	66
4.11.	X-ray structure of the <i>cis</i> -[Rh <sub>2</sub> (OAc) <sub>2</sub> (tfa) <sub>2</sub> ]/HEWL adduct....	76
4.12.	Summary of the interaction of <i>cis</i> -[Rh <sub>2</sub> (OAc) <sub>2</sub> (tfa) <sub>2</sub> ] with model proteins .....	78
4.13.	Interaction of [Rh <sub>2</sub> (OAc)(tfa) <sub>3</sub> ] with model proteins .....	80
4.14.	Synthesis and characterization of [Rh <sub>2</sub> (OAc)(tfa) <sub>3</sub> ].....	80
4.15.	Stability of [Rh <sub>2</sub> (OAc)(tfa) <sub>3</sub> ] in aqueous media and in solution reactivity with RNase A and HEWL.....	80
4.16.	X-ray structure of the [Rh <sub>2</sub> (OAc)(tfa) <sub>3</sub> ]/RNase A adduct .....	87
4.17.	X-ray structure of the [Rh <sub>2</sub> (OAc)(tfa) <sub>3</sub> ]/HEWL adduct .....	93
4.18.	Summary of the interaction of [Rh <sub>2</sub> (OAc)(tfa) <sub>3</sub> ] with model proteins .....	95
4.19.	<i>In crystallo</i> reactivity of [Rh <sub>2</sub> (OAc) <sub>4</sub> ]/RNase A .....	97
4.20.	X-ray structure of the [Rh <sub>2</sub> (OAc) <sub>4</sub> ]/RNase A adduct upon reaction with imidazole in the solid state.....	97
4.21.	Quantum chemical analysis of the reaction between [Rh <sub>2</sub> (OAc) <sub>4</sub> ]/RNase A and imidazole.....	100
4.22.	Summary of the <i>in crystallo</i> reactivity of [Rh <sub>2</sub> (OAc) <sub>4</sub> ]/RNase A . .....	106
4.23.	Interaction of [Rh <sub>2</sub> (OAc) <sub>4</sub> ]/RNase A with glycine.....	107
4.24.	X-ray structure of the [Rh <sub>2</sub> (OAc) <sub>4</sub> ]/RNase A adduct upon reaction with glycine in the solid state .....	107
4.25.	Summary of the interaction between [Rh <sub>2</sub> (OAc) <sub>4</sub> ]/RNase A and glycine .....	109

4.26.	Development of cross-linked RNase A crystals functionalised with $[\text{Rh}_2(\text{OAc})_4]$ as biohybrid materials for heterogeneous catalysis...	110
4.27.	Selection of suitable experimental conditions for the growth of CL_RNase A crystals.....	111
4.28.	$[\text{Rh}_2(\text{OAc})_4]$ accumulation within RNase A crystals into the $\text{P3}_2\text{21}$ space group.....	113
4.29.	Effect of temperature on CL_ $[\text{Rh}_2(\text{OAc})_4]$ /RNase A adduct crystals .....	117
4.30.	CL_Rh/RNase A as catalysts.....	121
4.31.	Identification of reaction products derived from styrene cyclopropanation promoted by CL_Rh/RNase A crystals.....	124
4.32.	Summary of the development of CL_RNase A crystals functionalised with $[\text{Rh}_2(\text{OAc})_4]$ as biohybrid materials for heterogeneous catalysis.....	125
<b>5.</b>	<b><i>METHODS</i></b>	<b>128</b>
5.1.	Materials .....	128
5.2.	Synthesis of the compounds used in this thesis.....	128
5.3.	UV-vis absorption spectroscopy .....	130
5.4.	Far UV-CD spectroscopy .....	131
5.5.	$^{19}\text{F}$ NMR spectroscopy .....	131
5.6.	$^1\text{H}$ NMR spectroscopy.....	133
5.7.	Crystallization of metal/protein adducts.....	133
5.8.	X-ray diffraction data collection, structure solution and refinement.....	136
5.9.	CLPCs catalysis.....	139
5.10.	GC-MS analysis .....	139
5.11.	ICP-OES measurements .....	140
5.12.	Density functional theory calculations .....	140

6. <i>SUMMARY</i>	142
7. <i>APPENDIX</i>	147
7.1. Data collection and refinement statistics .....	147
8. <i>PUBLICATIONS</i>	165
9. <i>REFERENCES</i>	167

## ABSTRACT

## 1. ABSTRACT

Dirhodium paddlewheel complexes are useful in several application fields, like catalysis, material or medicinal chemistry. Although artificial metalloenzymes based on the dirhodium tetracarboxylate reactivity with proteins have been developed, little is known on their molecular structures. The aim of this thesis is to provide new insights about the dirhodium tetracarboxylates/proteins recognition process and to explore the catalytic properties of dirhodium-conjugated cross-linked protein crystals.

The interaction between dirhodium tetraacetate ( $[\text{Rh}_2(\text{OAc})_4]$ ) and two of its derivatives, *cis*- $[\text{Rh}_2(\text{OAc})_2(\text{tfa})_2]$  and  $[\text{Rh}_2(\text{OAc})(\text{tfa})_3]$  (tfa = trifluoroacetate ion), with the two model proteins hen egg white lysozyme (HEWL) and bovine pancreatic ribonuclease (RNase A) was investigated both in solution and in the solid state. X-ray crystallography studies revealed that the three complexes degrade upon reaction with HEWL, while their dimetallic core is retained upon reaction with RNase A. In the dirhodium tetraacetate/RNase A adduct, the dimetallic centre axially binds His side chains. However, the bridging ligands surrounding the dirhodium core have a significant influence in directing the interaction between these complexes and proteins, since upon reaction of  $[\text{Rh}_2(\text{OAc})(\text{tfa})_3]$  with RNase A equatorial binding of dirhodium core to His side chains can also be observed.

The reactivity of the  $[\text{Rh}_2(\text{OAc})_4]$ /RNase A adduct in the solid state toward imidazole and glycine was also studied. Surprisingly, imidazole binds the dirhodium tetraacetate at equatorial rather than axial position. Three acetate ligands are replaced by six water molecules. DFT studies clarified that this unexpected reactivity is triggered upon hydrolysis of the dirhodium core, once that the metal compound is axially bound to a first molecule of imidazole (provided by His residues). Electronic structure analysis reveals that the Rh atom which is coordinated to the protein acts as a better Lewis acid than the other Rh atom. Glycine also binds the dirhodium core replacing equatorial acetate ligands.

Once verified that dirhodium tetraacetate retains its ability to react with small molecules when bound to RNase A in the solid state, catalysis experiments were carried out. Unfortunately, crystals of RNase A used to verify the binding of  $[\text{Rh}_2(\text{OAc})_4]$ , *cis*- $[\text{Rh}_2(\text{OAc})_2(\text{tfa})_2]$  and  $[\text{Rh}_2(\text{OAc})(\text{tfa})_3]$  to the protein (C2 space

group with two molecules in the asymmetric unit) are not the best choice to perform catalysis experiments since they need long preparation times (3 weeks). For this reason, crystals of the dirhodium/RNase A adduct were prepared in a different space group ( $P3_221$ ), that allows the protein crystal growth and functionalization with  $[\text{Rh}_2(\text{OAc})_4]$  in shorter times (26 h). X-ray structures of the  $[\text{Rh}_2(\text{OAc})_4]$ /RNase A adducts from  $P3_221$  crystals exposed to the dirhodium compound for different times reveal that the protein is extensively metalated by  $[\text{Rh}_2(\text{OAc})_4]$  just after 2 h of soaking. Also in this adduct, the metal compound structure is unperturbed upon 2 h protein binding. The dirhodium core is axially coordinated to His105 and His119 side chains, as observed for the metal/protein adduct crystals obtained into  $C2$  space group.

Cross-linking crystals of the adduct were then prepared using glutaraldehyde as cross-linking agent and the gentle diffusion technique. The structure of the adduct was solved by X-ray crystallography at two different temperatures (-173 and 0 °C). The results reveal no significant differences when the two structures are compared to each other and with the structure of the adduct from crystals in the  $C2$  space group.

The use of the cross-linked crystals of the  $[\text{Rh}_2(\text{OAc})_4]$ /RNase A adduct as catalysts towards olefine cyclopropanation and self-coupling of diazo compounds reactions was investigated using styrene and ethyl diazoacetate as model reagents. The results revealed that they catalyse both the reactions. While several by-products are observed upon ethyl diazoacetate homocoupling reaction, the styrene cyclopropanation occurs producing the ethyl-phenylcyclopropane-1-carboxylate with high selectivity.

Overall, these data provide the proof-of-concept for the catalytic use of cross-linked crystals of proteins in adduct with dirhodium compounds.



## 2. INTRODUCTION

### 2.1. Dimetallic complexes

The existence of dimetallic complexes with metal-to-metal bonds was confirmed for the first time in 1957.<sup>1</sup> These compounds were defined as *non-Wernerian* complexes, because, until the early 1960's, the chemistry of the transition metals was based on the conceptual framework established by Alfred Werner: a single metal ion is surrounded by a set of ligands with chemical and geometrical features described by the nature of the metal atom and its surrounding ligands, although metal complexes could be dinuclear, but with bridging ligands and no metal-metal bonds.<sup>1</sup>

Coordination complexes can form metal-to-metal single, double, triple and quadruple bonds, since *d*-orbitals are involved in the formation of these bonds.<sup>1</sup> Recently, quintuple metal-to-metal bond has been reported.<sup>2</sup> Due to symmetry restraint, only five nonzero overlaps between *d*-orbitals are allowed:

- $d_{z^2} \pm d_{z^2}$ ;
- $d_{xz} \pm d_{xz}$ ;
- $d_{yz} \pm d_{yz}$ ;
- $d_{xy} \pm d_{xy}$ ;
- $d_{x^2-y^2} \pm d_{x^2-y^2}$ .

The first four orbital combinations give rise, respectively, to  $\sigma$  and  $\sigma^*$  orbitals, a pair of  $\pi$  and  $\pi^*$  orbitals and of  $\delta$  and  $\delta^*$  orbitals, while the  $d_{x^2-y^2}$  orbitals interact with the set of ligands of their own metal atom.<sup>3</sup> The orbitals are usually ordered in energy as follows:  $\sigma < \pi < \delta < \delta^* < \pi^* < \sigma^*$  (for some complexes, as diruthenium ones,  $\delta^*$  and  $\pi^*$  orbitals are almost degenerate and can be order inverted)<sup>4</sup> ( 2.1).

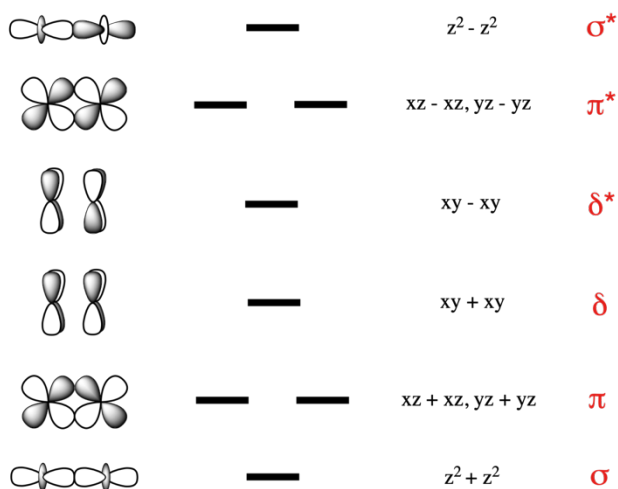


Figure 2.1 Molecular d-orbital scheme for dimetallic complexes.

The  $\sigma$  and  $\pi$  bonds are cylindrically symmetrical, hence, there is free rotation along single, double and triple bonds. However, the  $\delta$  bond reveals a strong angle sensitivity, in fact, the  $d_{xy} \pm d_{xy}$  overlap is maximum for eclipsed configuration of ligands, whereas it is minimum for a staggered configuration, although the bond strength is kept until approximately 30 degrees.<sup>1,5</sup> As a result, an eclipsed configuration of the surrounding ligands is observed with dimetallic centres with a metal-to-metal quadruple bond ( $D_{4h}$  symmetry). On the contrary, ligands are arranged in a staggered configuration around the dimetallic core when the bond order is lower than 3.5, because of their steric hinderance ( $D_{4d}$  symmetry).<sup>6,7</sup>

A common structural motif of dimetallic complexes consists of two metal atoms surrounded by four bridging bidentate ligands, giving rise to a “paddlewheel” dimetallic compound (Figure 2.2).

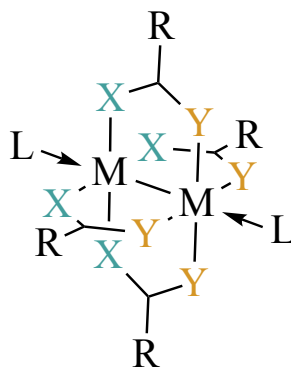


Figure 2.2. Generic paddlewheel dimetallic compound scheme. X and Y are generic electron donor atoms. R = generic organic chain.

Paddlewheel complexes can have axial ligands along the metal-to-metal axis. The presence and the number of axial ligands depend on the nature of the dimetallic unit. The bridging ligands can be symmetrical ( $X = Y$  in Figure 2.2) or asymmetrical ( $X \neq Y$  in Figure 2.2). The asymmetry between the electron donor atom opens the possibility of regioisomers, as depicted in Figure 2.3.<sup>8</sup>

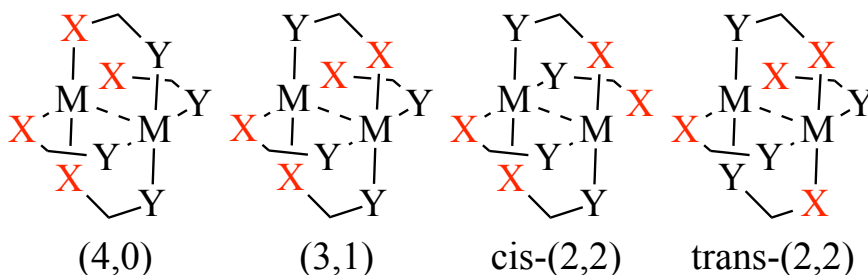


Figure 2.3. Possible regioisomers for dimetallic paddlewheel compounds bearing asymmetric bidentate ligands. The metal-to-metal bond is indicated with a dashed line because it can be a single or a multiple bond.

The complexes are defined “homoleptic” when the four bridging ligands are equal, otherwise, they are called “heteroleptic”.

The oxidation states commonly observed for dimetallic centres ( $M_2^{n+}$ ) in paddlewheel compounds is in the range  $n = 4 - 6$ .

Oxidation numbers of +3 or lower are not observed because transition metal ions in the oxidation state of +1 can be found only in the presence of  $\pi$ -acid ligand and this does not occur in paddlewheel complexes. Few examples of  $M_2^{7+}$  ions have been found but this oxidation state is not common for two reasons:

- The decrease in the size of the metal ion with increasing of the oxidation number weaken the overlap of the metal-to-metal bond;
- The increase of atomic charge leads to a strong repulsion between the metal centres.

Metal centres involved into a metal-to-metal bond have been found for transition metals of group 5 to 10 (with exception of Mn).<sup>3</sup>

## 2.2. Dirhodium paddlewheel complexes

Among the dimetallic complexes, the dirhodium paddlewheel compounds are the most studied ones, due to their versatility in many research fields.<sup>9</sup> Their scaffold consists of two Rh atoms in the oxidation state +2, held together by a single metal-to-metal bond, surrounded by four bridging equatorial ligands and two axial ligands along the Rh-Rh axis (synthesis of dirhodium complexes with one or no axial ligand has been accomplished using bulky equatorial ligands)<sup>10,11</sup> (Figure 2.4).

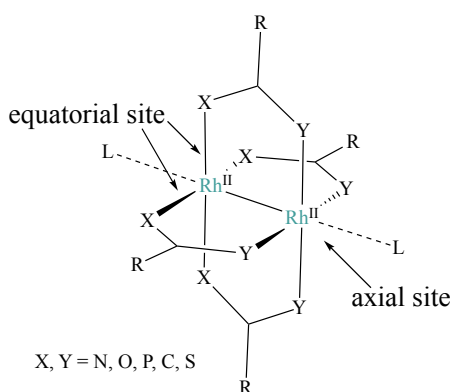


Figure 2.4. Schematic representation of a generic dirhodium paddlewheel compound. X and Y are generic donor atoms that can be equal or different.

The Rh-Rh distance in these complexes ranges from 2.35 to 2.45 Å and is almost insensitive to the nature of the axial ligand: electronic and steric factors combined with packing forces in a crystalline environment prevent the identification of a direct relationship between axial ligands and Rh-Rh distance.<sup>12</sup> The nature of the dirhodium bond has been object of extensive debate but is now commonly accepted that the Rh-Rh is a single bond.<sup>13,6</sup> A simplified version of molecular orbitals involved in the Rh-Rh bond is depicted in Figure 2.5.

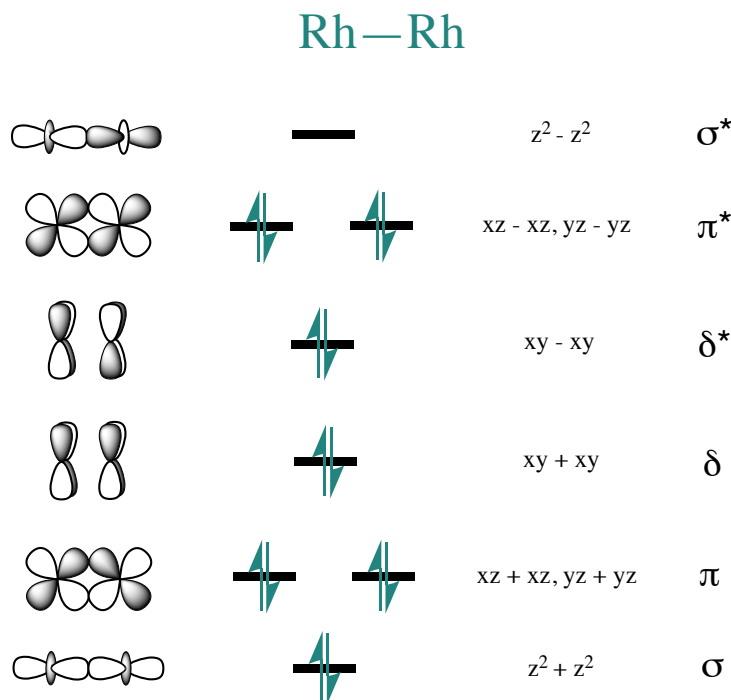


Figure 2.5. Molecular orbital scheme for the metal-to-metal bond in the dirhodium paddlewheel compounds.

The ground state configuration can be represented as  $\sigma^2\pi^4\delta^2\delta^{*2}\pi^{*4}$ , with a bond order of 1, consistent with a single bond.<sup>9</sup> However, this simplified version of ground state molecular orbitals does not explain the strength and shortness of Rh-Rh metal bond properly. To overcome this issue, a model that considers an extensive mixing between rhodium and bridging ligand orbitals and mixing of

higher lying empty orbitals into the ground state of the dimetallic orbital scheme has been proposed.<sup>14</sup>

Dirhodium complexes readily form adducts with a variety of donor ligands at their axial position. The distance between Rh atom and axial ligand is longer than the equatorial one. The Rh-L (L = axial ligand) bond is weakened by the *trans* effect exerted by the Rh-Rh bond.<sup>15</sup> The interaction of axial ligands with the dirhodium core influences the LUMO ( $\sigma^*$ ) orbital energy of the dimetallic centre, which is reflected in the colour of these complexes that depends on the nature of the axial ligand (Figure 2.6).<sup>10,16</sup>



Figure 2.6. Dependence of dirhodium paddlewheel complexes solution by the nature of the axial ligands. Pink or red purple solutions are observed with N ligands, blue or green solutions are obtained through axial coordination of O donors, orange or yellow solution can be observed with S- or P- based axial ligands. Adapted from reference 17.

Dirhodium complexes are classified according to their ligand at equatorial position. Equatorial ligands are usually monoanionic as carboxylates, thiocarboxylates, amidinates, carboxyamidates, phosphinates, phosphates, pyrazolates and triazenides. There are also dianionic bridging ligands and ligands that do not span the Rh-Rh bond.<sup>9</sup> When the donor atoms are not equivalent (e.g., carboxyamidates) isomerism can occur (see session 1.1).

### 2.3. Dirhodium tetracarboxylates: synthesis and reactivity

The most studied dirhodium paddlewheel complexes are the dirhodium tetracarboxylates, in which the dirhodium unit is equatorially contoured with four bridging carboxylate ligands. Dirhodium tetraacetate was the first dirhodium tetracarboxylate whose structure was confirmed by X-ray crystallography (Figure 2.7).<sup>6</sup>

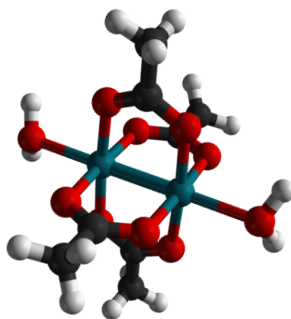


Figure 2.7. X-ray structure of dirhodium tetraacetate  $[\text{Rh}_2(\text{OAc})_4(\text{H}_2\text{O})_2]$  bearing two water molecules as axial ligands. Rh atoms are depicted in green, C atoms in black, O atoms in red and H atoms in white.

The dimetallic complex can be synthesized by refluxing  $\text{RhCl}_3 \cdot 3\text{H}_2\text{O}$  under  $\text{N}_2$  in a mixture of sodium acetate, acetic acid and ethanol<sup>18</sup> (the latter serves as reducing agent)<sup>19,2</sup>. Almost all the other dirhodium tetracarboxylates can be obtained by ligand exchange reactions of the acetate or trifluoroacetate with excess of the desired carboxylate.<sup>20,21</sup> The reaction proceeds in almost quantitative yield and is also useful for preparation of dirhodium tetracarboxylates with mixed ligand set.<sup>8</sup> Post-functionalization of these dimetallic complexes consists of direct modification of the organic moiety of the dirhodium ligands and can be used for the synthesis of complexes that cannot be prepared through ligand exchange reactions.<sup>22</sup>

Heteroleptic complexes are difficult to obtain because partial ligand exchange is difficult to control and usually leads to a mixture of complexes that can be isolated.<sup>23</sup>

Due to the weak bond between Rh atom and its axial ligands, a plethora of dirhodium tetracarboxylates that differ only by axial ligands can be easily obtained.<sup>12</sup> Dirhodium tetracarboxylates with axially bonded weak donor ligands can be prepared with the technique of ‘*solventless synthesis*’,<sup>24,25</sup> taking advantage from the tendency of  $[\text{Rh}_2(\text{tfa})_4]$  to sublime at 350 °C and its very Lewis acid character. Sublimation-deposition in the absence of solvent can provide dirhodium tetracarboxylates axially bound to naphthalene, ethene, benzene and other weak electron donor. The reactivity of dirhodium tetracarboxylates through ambidentate ligands can be tuned by the nature of the equatorial ligands: for example, DMSO interacts with  $[\text{Rh}_2(\text{OAc})_4]$  through the S atom, but it interacts with  $[\text{Rh}_2(\text{tfa})_4]$  using the O atom, because the electron withdrawing tfa group decreases the *softness* of the  $\text{Rh}_2^{4+}$  core.<sup>26</sup>

Dirhodium compounds without bridging equatorial ligands can be formed with water ( $[\text{Rh}_2(\text{H}_2\text{O})_{10}]^{4+}$ ), acetonitrile, porphyrins, and other compounds.<sup>27-29</sup> In these complexes, the Rh-Rh bond is weaker than in the paddlewheel complexes (Rh-Rh distance is around 2.60Å) and equatorial ligands are arranged in a staggered configuration that reduces the ideal  $D_{4h}$  symmetry (Figure 2.8). Staggered conformation is also preferred with small linear ligands as acetonitrile.<sup>7</sup>

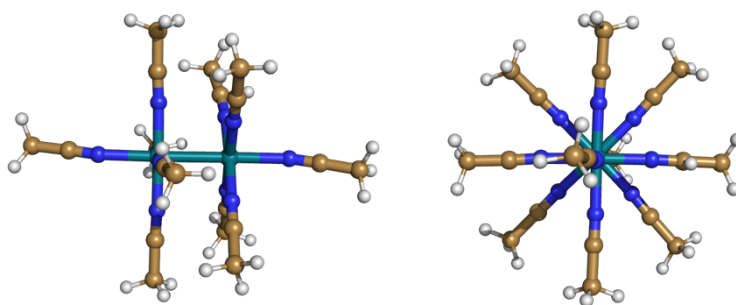


Figure 2.8. Side-on (on the left) and frontal (on the right) view of the X-ray structure of  $[\text{Rh}_2(\text{CH}_3\text{CN})_{10}]^{4+}$  ion. Rh atoms are depicted in green, N atoms in blue, C atoms in dark yellow and H atoms in white.

Despite the strength of Rh-Rh bond, the dimetallic centre can be cleaved in several ways. When dirhodium tetracarboxylates are mixed with one equivalent of an oxidant agent Rh(II)-Rh(III) species are formed. An excess of oxidant results in

dimetallic bond cleavage.<sup>8</sup> The cleavage can provide dirhodium paddlewheel structures with two Rh atoms breaking the metal-to-metal bond. In other cases, monometallic Rh(III) compounds can be produced.<sup>30,31</sup> Oxidation of the dirhodium bond can also produce Rh(III)-O-Rh(III) or Rh(III)-S-Rh(III) species where the two Rh(III) atoms are held together by O or S atoms in a bridging fashion.<sup>32</sup>

Reduction of the dirhodium core leads to the formation of Rh(I) monometallic compounds. Despite dirhodium tetracarboxylates are stable under mild acid solutions, in the presence of high concentration of strong acids as HCl or HBr, monometallic Rh(III) species like  $\text{RhCl}_6^{3-}$  can be formed.<sup>12</sup> Finally, treatment of  $\text{Rh}_2(\text{tfa})_4$  with  $\text{Bi}_2(\text{tfa})_4$  provides the complex  $[\text{Rh}-\text{Bi}(\text{tfa})_4]$  which expands the range of application of dimetallic paddlewheel complexes.<sup>33</sup>

#### 2.4. Dirhodium tetracarboxylates: applications

Dirhodium paddlewheel complexes can be used as building blocks for construction of supramolecular arrays. Bifunctional ligands can be used for connecting dirhodium units together. Supramolecular assemblies can be formed through axial or equatorial ligands. Combination of axial and equatorial linkers can be useful for preparing 1D-, 2D- and 3D-supramolecular arrays using  $\text{Rh}_2^{4+}$  units. These arrays are able to accommodate ions or molecules (Figure 2.9).<sup>34,35</sup>

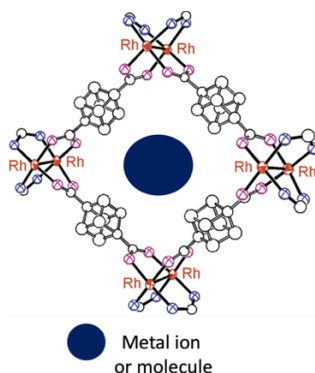


Figure 2.9. Structure of the dirhodium cubane dicarboxylate core. The blue sphere represents a generic metal ion or molecule entrapped in the 2D-array. Figure adapted from reference 35.

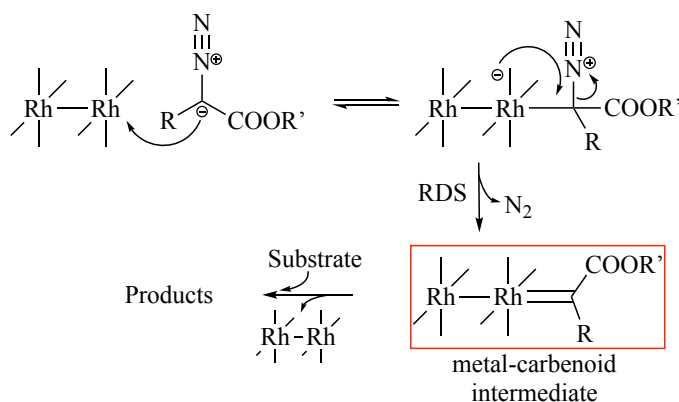
Dirhodium tetracarboxylates are also employed as CO, NH<sub>3</sub> and NO detectors, because the axial binding of these small molecules leads to changes in the physical properties of the complexes (e.g. conductivity and colour).<sup>36-38</sup>

Dirhodium compounds are also considered promising anticancer agents. They exhibit antitumour activity *in vivo* against several diseases as L1210 tumours, Ehrlich ascites, sarcoma 180 and P388 tumour lines (and other diseases).<sup>9</sup> Equatorial ligands can be exchanged to modulate the anticancer activity or to minimize the side effects of the paddlewheel complexes as metallodrugs.<sup>39</sup>

The molecular bases of the antitumour activity of these complexes has not yet been elucidated.<sup>40</sup> However, it is known that they interact with nucleobases forming axial and equatorial adducts.<sup>41,42</sup> SDS-PAGE experiments suggest that the dimetallic centres interact also with *double stranded*-DNA, with a preference of the dimetallic core in interacting with purine rather than pyrimidine sites (as observed from experiments performed on *single stranded*-DNA).<sup>43</sup> Upon binding of the macromolecule to the dirhodium core, covalent cross-link of the two DNA strands can occur in axial/axial, equatorial/equatorial or axial/equatorial fashion.<sup>44</sup>

The interaction of dirhodium paddlewheel complexes with DNA *in vivo* leads to the inhibition of protein synthesis, a phenomenon that could explain the anticancer activity of this class of complexes.<sup>40</sup>

Dirhodium tetracarboxylates are mainly used as homogeneous and heterogeneous catalysts of organic reactions. Due to the strong Lewis acidity of the dirhodium core, these complexes allow the transfer of electron deficient species (carbenes or nitrenes) on organic substrates.<sup>8</sup> In this class of reactions, the key step is the formation of a metal-carbenoid (or -nitrenoid) intermediate that can go through several transformations, such as cyclopropanation,<sup>45</sup> C—H insertion<sup>46</sup> Si—H insertion<sup>47</sup> or ylide generation.<sup>48</sup> Rh-carbenoids can be generated by several precursors, but the most common are diazo compounds.<sup>49</sup> For these reactions, the catalytic pathway has been extensively studied and is now clearly understood (Scheme 1).



Scheme 1. Catalytic pathway of carbene transfer reaction catalysed by dirhodium tetracarboxylates.

The dimetallic compound acts as a Lewis acid and undergoes to reversible electrophilic addition to the diazo compound at carbon atom, followed by a nitrogen lost to form the metal-carbenoid adduct. This is the rate-limiting step, that is followed by the transfer of the forming carbene from the metal to a substrate, providing the recovery of the dimetallic catalyst and different reaction products depending on the nature of the substrate.<sup>50</sup> This pathway is determined by the catalyst electrophilicity and the backbonding from the metal to the carbon atom involved in the Rh—C bond. Hence, the efficiency and the rate of the reaction can be tuned by changing the equatorial ligands of the dirhodium core or the substituents of the diazo compounds.<sup>51</sup> For asymmetric catalysis, the selectivity is achieved in the carbene transfer step of the catalytic path.<sup>52</sup> The choice of equatorial ligands not only affects the catalytic efficiency but also the regio- and stereo- selectivity. For example, carboxyamidate ligands display higher selectivity than carboxylates for stereoselective carbene transfer but dirhodium tetracarboxylates are more reactive toward this reaction.<sup>51</sup> Furthermore, for intramolecular reactions of compounds with a terminal double bond, a strong preference for macrocyclization is observed using dirhodium tetracarboxylates, while allylic cyclopropanation is promoted using dirhodium tetracarboxyamidates.<sup>53</sup>

Hence, dirhodium paddlewheel compounds are very efficient for several applications, especially in the field of catalysis, because they can promote a large

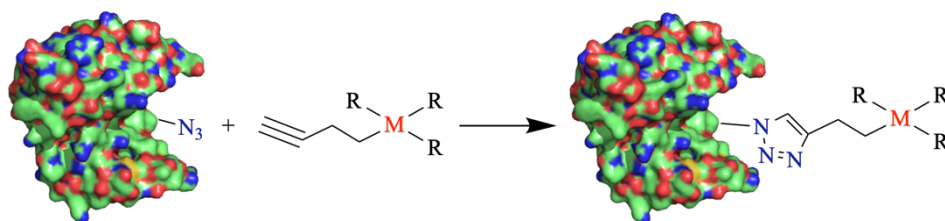
range of reactions. Furthermore, the selectivity can be tuned modifying the equatorial ligands that surround the dirhodium core.

## 2.5. Interaction of metal compounds with proteins

The interaction of metal or metal complexes with proteins is of significant interest in a number of fields.<sup>54</sup>

The process through which metal complexes form adducts with proteins is known as protein metalation. In the protein metalation process, coordinative bonds between the metal and ligands need to be broken and bonds between the metal and protein atoms need to be formed.<sup>55</sup> Metal/protein adducts can be used as metallodrug delivery systems and as artificial metalloenzymes.<sup>56-60</sup> The study of protein metalation can be helpful in unveiling the mechanism of action of metal-based drugs or their toxicity.<sup>61,62</sup>

Beyond the coordinative bonds that lead to the formation of metal/protein adducts, metal complexes can interact with proteins in a non-covalent fashion, via H-bonds or hydrophobic interactions with protein moieties.<sup>63,64</sup> Metal complexes can also be conjugated to engineered proteins via covalent bond between metal ligands and protein residues. An example of this process is reported in Scheme 2.<sup>65</sup> In this example, a protein engineered to contain an azide functional group reacts with a metal compound functionalized with an alkyne moiety through [3+2] azide-alkyne cycloaddition reaction, connecting the protein and the metal compound via formation of a 1,2,3-triazole ring.



Scheme 2. Bioconjugation upon reaction of metal ligands with protein residues. M indicates a generic metal compound. R refers to a generic organic molecule.

In the last decades, an increased number of experimental details allowed to summarize some general trends of protein metalation process.<sup>66</sup> After bonding with proteins, metal complexes can be completely broken or take part of redox processes which influence their coordination geometry.<sup>67,68</sup> Furthermore, a single protein can host more than one copy of the same metal complex (Figure 2.10).<sup>69</sup> When a metal compound is hosted in a protein environment, its first and second coordination spheres can change. As a result, a metal complex can lose, retain or improve its activity in the metal/protein adduct.<sup>70</sup>

Similarly, the physico-chemical properties of the protein can be affected upon interaction with a metal compound. For example, protein thermal stability is usually altered upon metal binding because the metal compound can affect the protein secondary and tertiary structure.<sup>67,71</sup> The experimental conditions explored for the formation of metal/protein adducts also play a non-innocent role in directing the protein metalation process.<sup>66</sup>

Despite the recent advances in this field,<sup>66</sup> many aspects of protein metalation process are still unclear and further studies are needed to fully understand the mechanism at the basis of the proteins/metal complexes recognition process.

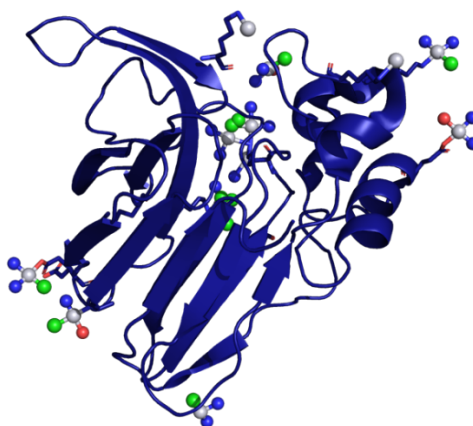


Figure 2.10. Structure of the adduct formed upon reaction of the Pt-based drug cisplatin with the model protein Thaumatin (PDB code: 5L4R).<sup>69</sup> Metal and metal ligands are shown as spheres.

## 2.6. Interaction of dirhodium tetracarboxylates with proteins

Recently, protein metalation by dimetallic complexes has raised increased attention.<sup>72-77</sup> Protein metalation by dirhodium tetracarboxylates has been investigated and some Rh<sub>2</sub>/protein adducts with interesting properties have been developed.<sup>78-80</sup>

The interaction of dirhodium tetraacetate with the  $\beta$ -domain of  $\beta$ -metallothionein rh1a has been investigated in solution by spectroscopic and mass spectrometry techniques.<sup>72</sup> The dimetallic compound forms an adduct where acetate moieties are replaced by S atoms of Cys side chain residues. In the adduct a metal to protein ratio of 3:1 was found. Time-dependent mass spectrometry analysis revealed that at neutral pH the metal binding occurs through a non-cooperative metalation mechanism,<sup>73,74</sup> with one, two or three dirhodium units that bind the protein subsequently, losing the acetate ligands, while at acid pH (< 2) up to six [Rh<sub>2</sub>(OAc)<sub>4</sub>] units can be found within a single protein unit, without loss of acetate ligands (Figure 1.11).<sup>74</sup> Hence, the binding depends on the environmental conditions. Due to potential application of [Rh<sub>2</sub>(OAc)<sub>4</sub>] in medicinal chemistry,  $\beta$ -metallothionein rh1a has been suggested as a scavenger for metal compounds within living organisms.<sup>74</sup>

The adducts formed upon reaction of [Rh<sub>2</sub>(OAc)<sub>4</sub>] and [Rh<sub>2</sub>(OAc)<sub>2</sub>(bpy)<sub>2</sub>] (bpy = bipyridine) with Human Serum Albumin (HSA), the most abundant plasma protein, have been studied in solution.<sup>75,76</sup> The metal complexes bind the protein with a molar ratio of 8:1 and 7:1 respectively. [Rh<sub>2</sub>(OAc)<sub>4</sub>] or [Rh<sub>2</sub>(OAc)<sub>2</sub>(bpy)<sub>2</sub>] binding to HSA induces protein conformational changes, reducing its  $\alpha$ -helix content. X-ray absorption spectroscopy analysis suggests that [Rh<sub>2</sub>(OAc)<sub>4</sub>] binding to the protein occurs via axial coordination to N atoms of His side chains or to S atom of the free Cys34.<sup>76</sup>

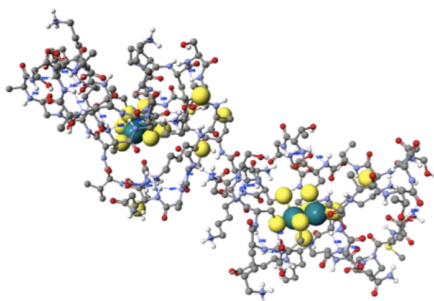


Figure 2.11. Model of the  $[\text{Rh}_2(\text{OAc})_4]$ /metallothionein adduct obtained by (molecular dynamics) MD simulation. Yellow spheres enlighten Cys residue exposed on the protein surface, teal spheres indicate dirhodium units. Adapted from reference 74.

The ability of dirhodium tetraacetate to cross-link different protein molecules has been explored using horse heart cytochrome C (Cyt C). The metal compound can link two cytochrome molecules through axial ligation of His side chains. The cross-linking is pH sensitive, in fact, it occurs at pH 7, but it is not observed at pH 2. However, once the adduct  $[\text{Rh}_2(\text{OAc})_4]$  (Cyt C)<sub>2</sub> is formed, it is stable at pH 5 even in presence of strong donor anions like  $\text{N}_3^-$  and  $\text{CN}^-$  (Figure 2.12).<sup>77</sup>

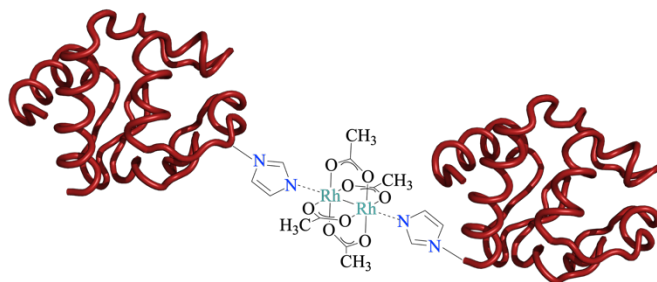


Figure 2.12. Schematic representation of the adduct formed by  $[\text{Rh}_2(\text{OAc})_4]$  with two Cyt C molecules. Dirhodium unit acts as a cross-linker.

Since the high versatility of dirhodium tetracarboxylates as catalysts, these compounds have been conjugated within protein scaffolds for artificial metalloenzymes preparation. An artificial metalloenzyme for *inter*-molecular selective cyclopropanation reaction has been obtained by interaction of a biotinylated dirhodium compound with streptavidin.<sup>78</sup> The artificial metalloenzyme retains its catalytic activity in the periplasm of *E. coli* cells (Figure 2.13A).<sup>78</sup> The same reaction has been catalysed by an engineered prolyl oligopeptidase (POP) conjugated with a dirhodium derivative via strain-promoted azide-alkyne cycloaddition. In both cases, the metal/protein adducts display a higher stereo- and chemo-selectivity than the metal complex alone.<sup>79</sup> Further mutations of POP scaffold led to the preparation of a dirhodium-based artificial metalloenzyme capable of promoting selective E-alkene coupling (Figure 2.13B).<sup>80</sup>

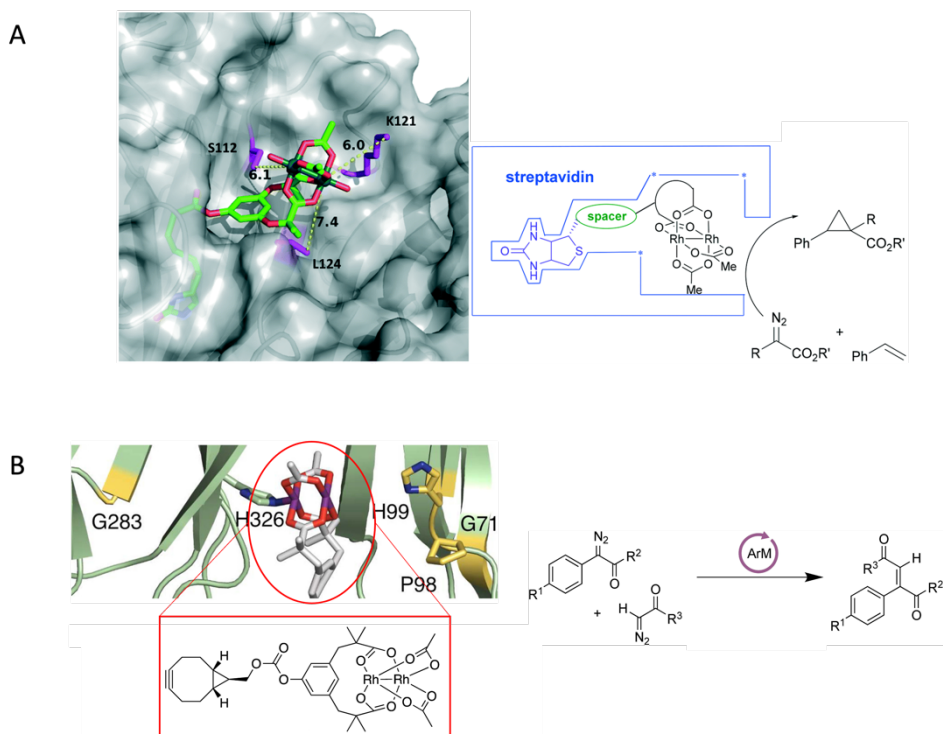


Figure 2.13. A. Dirhodium-based artificial metalloenzyme (ArM) for olefin cyclopropanation. The model on the left side was obtained by docking. B. Rh-

based ArM for selective self-coupling of diazo compounds and MD (molecular dynamic) simulation of the binding site of the metal/protein adduct (on the left). Panel A and B were adapted from references 79 and 80, respectively.

The first structural evidence of a dirhodium tetracarboxylate/protein adduct was obtained upon reaction of  $[\text{Rh}_2(\text{OAc})_4]$  with bovine pancreatic ribonuclease.<sup>81</sup> In the crystal structure of the  $[\text{Rh}_2(\text{OAc})_4]/\text{RNase A}$  adduct, two dirhodium binding sites were observed, in proximity of His105 and His 119 side chains (Figure 2.14).

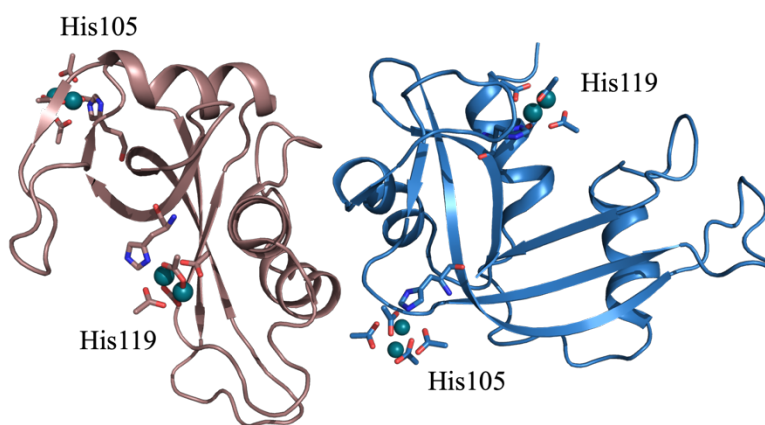


Figure 2.14. Overall structure of  $[\text{Rh}_2(\text{OAc})_4]/\text{RNase A}$  adduct. Crystals of the adduct belong to the C2 space group and contain two molecules in the asymmetric unit, coloured in salmon pink and marine blue. Rh atoms are displayed in teal. Figure adapted from reference 81.

In both cases, the dimetallic compound is axially bound to an N atom of the imidazole ring of the His side chain. The paddlewheel structure of the dimetallic compound with four bridging acetate ligands is retained, and the remaining axial position is occupied by a water molecule (Figure 2.15). Distances and angles of the dimetallic units found in the metal protein adducts agreed with those observed for dirhodium tetracarboxylates alone.<sup>81</sup>

The interaction between the metal complex and RNase A has been confirmed also in solution using electrospray ionisation mass spectrometry (ESI-MS) and spectroscopic techniques. Furthermore, the binding of imidazole to the metal compound has been verified by titration of  $[\text{Rh}_2(\text{OAc})_4]$  with increasing amount of imidazole.<sup>81</sup>

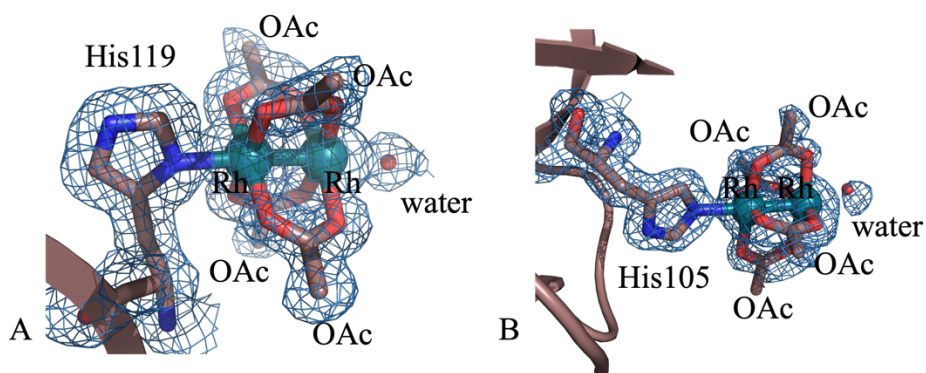


Figure 2.15.  $[\text{Rh}_2(\text{OAc})_4]$  binding site close to His119 side chain is in panel A,  $[\text{Rh}_2(\text{OAc})_4]$  binding site close to His105 side chain in panel B. The electron density map is contoured at  $1.0\sigma$ . Figure was adapted from reference 81.

The huge range of applicability of  $[\text{Rh}_2(\text{OAc})_4]$  and its derivatives in adduct with proteins requires more structural insights to provide a deeper knowledge of protein metalation by dirhodium tetracarboxylates.

## 2.7. Crystals of metal/protein adducts

Protein crystals are formed by highly ordered density-packed structures, held together by non-covalent interactions.<sup>82</sup> Due to the high volume of a protein, when these molecules are packed in a crystal lattice, large solvent channels are formed around the symmetry mates, (solvent channels range in size from 30% to 65% of the total lattice volume) (Figure 2.16).<sup>83</sup>

Hence, organic molecules, metal ions or complexes can diffuse through solvent channels and interact with proteins in the solid state.

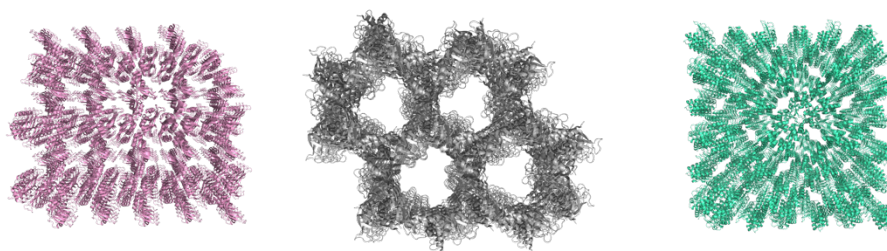


Figure 2.16. Porous lattice of protein crystals. From left to right: RNase A, C2 space group (PDB code: 1JVT); RNase A, P3<sub>2</sub>21 space group (PDB code: 5OGH); Hen egg white lysozyme, space group P4<sub>3</sub>2<sub>1</sub>2 (PDB code: 193L).

When a metal compound is mixed with a protein in solution, the metal-protein binding is not the only occurring phenomenon. In fact, multiple equilibrium processes, aquation of the metal compound, ligand detachment from the metal centre and redox pathway can simultaneously occur. This plethora of processes often hinder the investigation of metal-protein adduct formation by conventional techniques like spectroscopies or calorimetry.<sup>84</sup> Hence, crystallization and subsequent X-ray diffraction analysis often represent the only available strategy to correctly investigate and describe the interaction between proteins and metal complexes.

Crystals of metal/protein adducts can be obtained using two main strategies: co-crystallization and soaking. In the former technique, metal and protein are mixed in solution and then crystallized (Figure 2.17).<sup>85</sup>

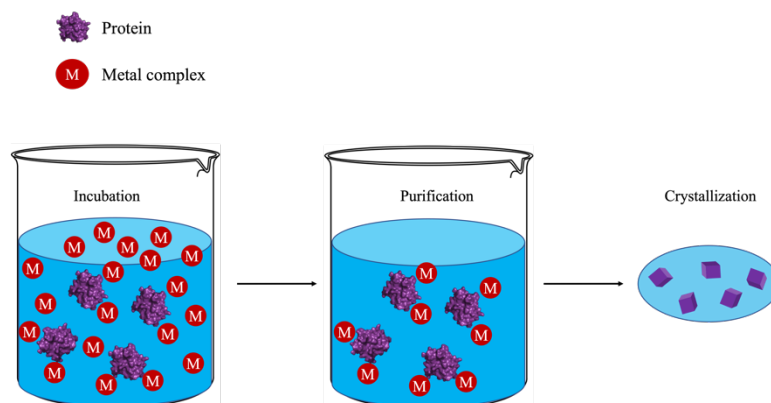


Figure 2.17. Schematic representation of co-crystallization technique.

The latter strategy takes advantage from solvent channels within protein crystal lattice. In fact, with soaking the metal complex is directly introduced in the drop containing protein crystals as a powder (Figure 2.18A), a solution (Figure 2.18B) or transferring the crystals from their mother liquor to a new solution containing the metal compound (Figure 2.18C).<sup>84</sup>

Both these techniques present several advantages and drawbacks. For example, during co-crystallization, after incubation of a metal complex with a protein, a purification step of the reaction mixture is required before performing crystallization, for removing the excess of metal, the possible oligomers formed upon protein-protein interaction or by-products derived from the interaction of metal complexes with buffer, additives etc. Without the purification step, the presence of these species could hamper the crystallization process.<sup>86</sup> Instead, with the soaking method, the metal compound is in direct contact with a protein crystal and purification of the metal-protein adduct is not required. With this method the interaction of metal compounds and proteins occurs only with limited portions of a protein, which are exposed to the solvent channels, while using co-crystallization all the protein surface is available for the metal-protein interaction to occur.<sup>87,88</sup> Hence, it is desirable to obtain crystals of metal/protein adducts using both soaking and co-crystallization methods, for providing a better description of metal/protein interaction in the solid state.

Structural data derived from X-ray diffraction of metal/protein adducts are of great interest because they provide a detailed description of the metal/protein interaction, like the number of metal atoms hosted by a single protein or a detailed depiction of the metal first, second and third coordination sphere at atomic resolution. Such a deep description of the metal/protein interaction is of interest for many application fields, as biocatalysis, medicine and material science.<sup>84,66</sup>

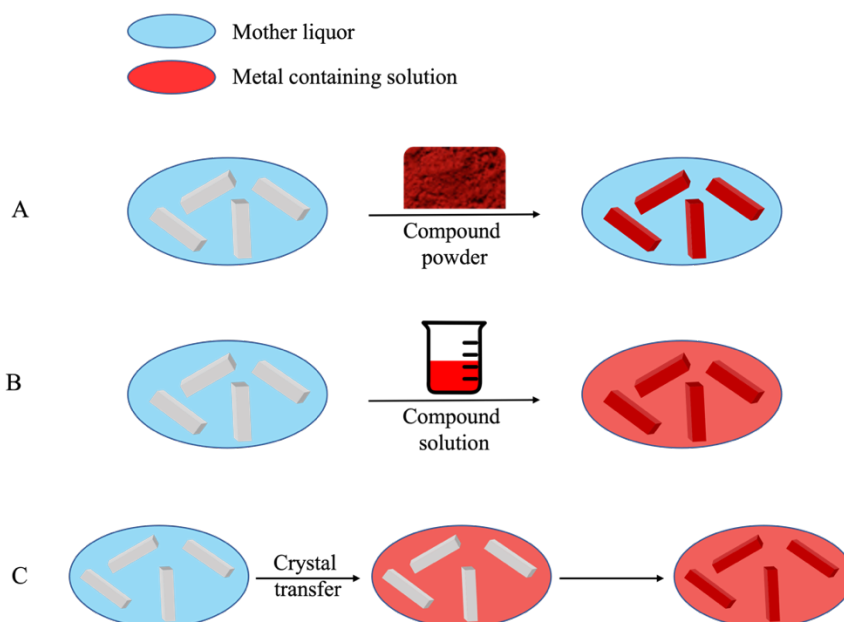


Figure 2.18. Schematic representation of soaking method. Soaking obtained using metal complex powder (panel A). Soaking using a metal complex solution (panel B). Transfer of crystals from their mother liquor to a solution containing the metal complex (panel C).

## 2.8. Cross-linked protein crystals (CLPCs)

Protein crystals can be seen as porous materials through which metal ions or complexes can diffuse, leading to metal/protein crystalline adducts with well-defined active site repeated in a regular 3D order.<sup>89</sup> Furthermore, the weak protein-protein interaction within a crystal allows some flexibility of the macromolecules which can retain their function in the solid state or tolerate small conformational

changes associated with chemical or physical processes. Thus, protein crystals are ideal candidates for providing protein assemblies.

However, the use of protein crystals as biomaterials is still rather limited. This is due to their high fragility. In fact, the high solvent content and the weak interaction that held together the symmetry mates within the crystal lattice make protein crystals difficult to handle, and unstable outside their mother liquor.<sup>90</sup>

An effective strategy to stabilize protein crystals is the covalent cross-linking with organic bifunctional molecules. Cross-linking treatment provides cross-linked protein crystals (CLPC) which are stable and insoluble both in organic solvents and aqueous solutions. CLPCs display a good thermal and mechanical stability,<sup>91,92</sup> thus expanding the applications of protein crystals as porous materials (Figure 2.19).

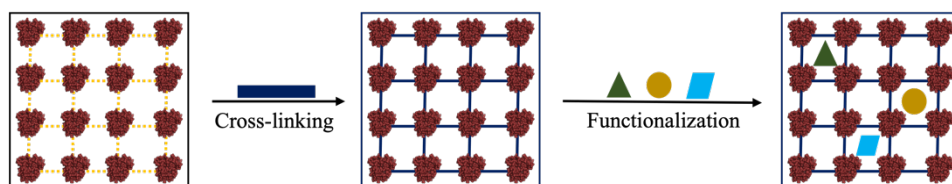


Figure 2.19. Schematic representation of CLPCs preparation and functionalization with chemicals.

## 2.9. Preparation of CLPCs

Preparation of CLPCs by covalent cross-linking is obtained by diffusion of a cross-linking agent through solvent channels using soaking technique.

Cross-linkers can be divided in three main categories (Figure 2.20):

- Homobifunctional cross-linkers, with two identical functional groups (Figure 2.20A).<sup>93</sup>
- Heterobifunctional cross-linkers, with two different functional groups (Figure 2.20B).<sup>94</sup>

- Photoactive cross-linkers. These are an extension of heterobifunctional cross-linkers, but with two functional groups that need to be activated by light irradiation (Figure 2.20C).<sup>90</sup>

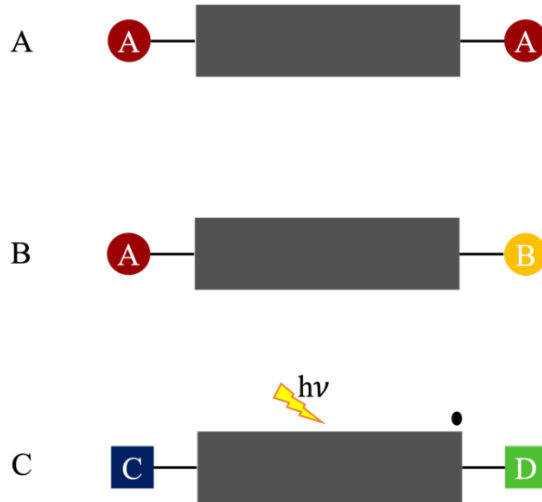


Figure 2.20. Schematic representation of homobifunctional (panel A), heterobifunctional (panel B) and photoactive cross-linking agents (panel C).

Cross-linking process proceeds in *intra*-molecular or *inter*-molecular fashion.<sup>95</sup> In the former case, two residues of a protein are covalently connected by a cross-linking agent (homobifunctional cross-linkers are usually used for this purpose). In the latter case, a cross-linking agent connects the residues of two different units in a crystal lattice with a covalent bond (Figure 2.21).

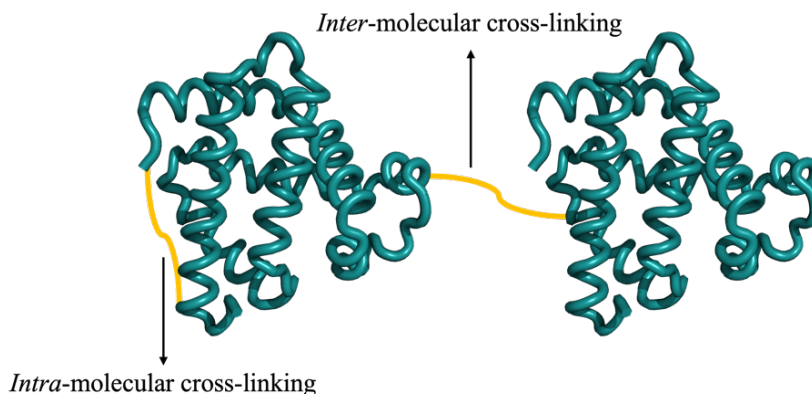


Figure 2.21. Depiction of *intra*- and *inter*-molecular cross-linking.

Heterobifunctional cross-linkers could help in linking proteins which expose many different residues on their surfaces. When a photoactive cross-linker is activated, it leads to formation of free radicals that interact rapidly with proteins, but with low specificity.

Lysine, cysteine, and amino acids containing carboxylate side chains are usually involved in cross-linking reaction.

### 2.10. Glutaraldehyde: a milestone for preparation of CLPCs

To stabilise a protein crystal, both *intra*- and *inter*- molecular cross-linking are needed. Common cross-linking agents are usually designed for a specific protein in a specific crystal lattice.

Glutaraldehyde (GA) occupies a unique position among the cross-linking agents because it can connect protein moieties within a crystal lattice both in *intra*- and *inter*- molecular mode. Hence, GA can be used for cross-linking of many protein crystals, regardless the protein folding or the crystal packing.<sup>90</sup>

The reason of the GA versatility as a cross-linker resides in the complexity of its aqueous solutions. When GA is dissolved in aqueous media, it has a strong tendency to the self-polymerization. The rate and the nature of polymeric forms

of GA in aqueous solution depend on experimental conditions, like pH, temperature and GA concentration (Figure 2.22).<sup>96</sup>

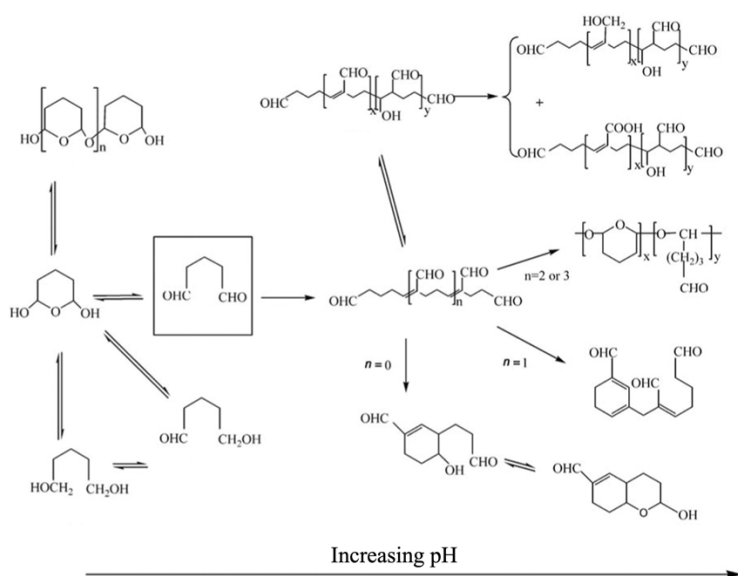


Figure 2.22. Possible GA oligomers and polymers in aqueous solution depending on pH. Figure adapted from reference 96.

Since protein crystallization generally occurs in aqueous media, when GA is used as a cross-linker, many potential cross-linkers of different length and shape are provided.<sup>96</sup> This leads to a non-specific cross-linking, that can be useful for preparing CLPCs.

GA has a strong preference to interact with Lys or Arg groups.<sup>97</sup> However, the general mechanism of cross-linking by GA is not completely understood. Due to the plethora of oligomeric and polymeric species of GA solutions, the cross-linking process is often inhomogeneous, and CLPCs may crack because of the non-uniform physico-chemical stress they undergo.<sup>90</sup> A good strategy to limit this drawback, is the gentle diffusion technique (“gentle cross-linking”) in which GA is introduced through vapor diffusion into a crystallization solution containing protein crystals (Figure 2.23).<sup>98</sup> In this way, only monomeric and short oligomeric

forms of GA can diffuse through protein crystal solvent channels, rendering the cross-linking process more uniform.

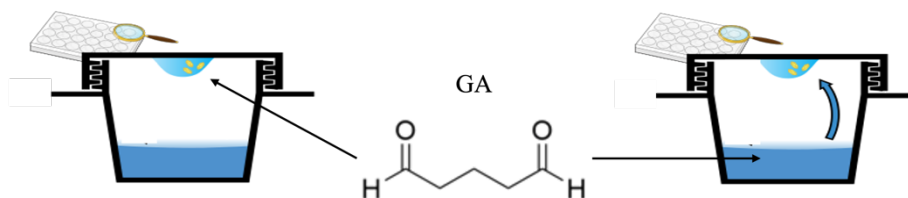


Figure 2.23. Schematic representation of the cross-linking with GA. On the left: addition of GA to the drop containing protein crystals. On the right: gentle diffusion technique: GA was added to the reservoir solution.

### 2.11. CLPCs properties and application

Catalytic activity of enzymes is reduced in the presence of organic solvents, because of the reduced dielectric constant and number of H-bond. Furthermore, with high percentage of organic solvents, enzymes can lose their activity due to denaturation. In cross-linked crystals, enzymes retain their activity both in low and high percentage of organic solvents. Thus, CLPCs could expand the function of an enzyme towards substrates which are not soluble in water.<sup>99</sup> Due to their thermal stability, CLPCs can exhibit high activity at relatively high temperature, extreme pH, and even in presence of radicals, expanding a protein scope beyond its natural one.<sup>100,101</sup> Moreover, the long-time resistance of CLPCs to several environmental conditions makes them ideal candidates for preparation of heterogeneous robust catalysts.<sup>102</sup>

The regular porosity in a long-range 3D order (solvent channel diameter ranges from 15 to 100 Å), and the functionalization with organic molecules, metal ions or complexes and macromolecules such as enzymes<sup>103</sup> make CLPCs ideal systems to be functionalised by exogenous compounds forming bio-hybrid materials with several potential applications. For example, biomineralization mechanism can be studied within crystal lattice,<sup>104</sup> or crystal pores can serve as templates for construction of organic, metallic, or inorganic nanoparticles with different shapes.<sup>105-107</sup> Moreover, enzymes can be conjugated within CLPCs pores for improving the enzyme biological activity under harsh conditions as drying or high

temperature.<sup>108</sup> The capability of these protein assemblies to interact with many kinds of compounds allows their use as biosensors or as detector of pollutants.<sup>109,110</sup>

Stability, porosity, and long-range regularity of CLPCs make them attractive for chromatographic stationary phases. In fact, the porosity of protein crystals can be useful for size exclusion chromatography and the intrinsic chirality of proteins is of interest for production of stationary phases for chiral chromatography. The affinity of proteins toward specific substrates can also be exploited for affinity chromatography.<sup>100</sup>

Finally, CLPCs are of huge interest in metalloenzymes research, because it is possible to combine the reactivity of a metal compound and the engineering of proteins to precisely design the first, second and third metal coordination spheres, to develop catalysts with unique and unprecedented performances.<sup>111</sup> Furthermore, because of the insolubility of CLPCs, the catalytic system can be easily separated from the reaction mixture and reused several times.

Despite all the advantages described above, the use of CLPCs is still far from large scale application. The preparation of CLPCs requires high amount of pure protein samples, and there is a great loss of proteins during purification, crystallization, and cross-linking steps.<sup>90</sup> Moreover, cross-linkers can interfere with protein activity in some cases and the non-homogeneous cross-linking can damage the crystal lattice compromising its mechanical properties. Hence, new techniques are needed for preparing CLPCs with high yield and new cross-linking agents need to be developed because the use of CLPCs as protein macro assemblies leads to tremendous advantages compared to proteins or protein crystals in many fields.



### 3. AIM OF THE THESIS

The combination of dirhodium tetracarboxylates versatility and intrinsic protein features has proven to be an effective approach for developing biohybrid compounds with interesting functional properties. However, the mechanism of protein metalation by dirhodium tetracarboxylates is still unclear and there are few reports on dirhodium/protein adducts in literature, especially in the solid state. Hence, a deeper knowledge of protein metalation is required to further understand the determinants that drive the dirhodium/protein adduct formation and the potential application of these systems.

This thesis is aimed to investigate the protein metalation by dirhodium tetracarboxylates both in solution and in the solid state and to explore the catalytic activity of dirhodium-conjugated CLPCs as functional materials.

Hence, the interaction between  $[\text{Rh}_2(\text{OAc})_4]$  and some of its fluorinated derivatives (*cis*- $[\text{Rh}_2(\text{OAc})_2(\text{tfa})_2]$  and  $[\text{Rh}_2(\text{OAc})(\text{tfa})_3]$ ) with the model proteins RNase A and hen egg white lysozyme (HEWL) were investigated both in solution and in the solid state. The reactivity of the  $[\text{Rh}_2(\text{OAc})_4]$ /RNase A adduct towards imidazole and glycine in the solid state was analysed by X-ray crystallography and, in the case of imidazole, also by quantum chemical simulations. Finally, CLPCs of  $[\text{Rh}_2(\text{OAc})_4]$ /protein adducts (CL\_**Rh**/RNase A) were prepared and their application as heterogeneous catalysts was tested for some reactions promoted by dirhodium tetracarboxylates.

## AIM OF THE THESIS

## 4. RESULTS AND DISCUSSION

### 4.1. Crystallization of the adducts formed upon reaction of $[\text{Rh}_2(\text{OAc})_4]$ with HEWL

HEWL is a protein that crystallizes under different experimental conditions with high reproducibility. For this reason, it is usually used as a model system to study the interaction between protein and metal complexes.<sup>66</sup> Hence, the protein was selected to study the interaction of  $[\text{Rh}_2(\text{OAc})_4]$  with proteins.

Six structures of adducts of HEWL with  $[\text{Rh}_2(\text{OAc})_4]$  were solved. Four datasets were obtained using crystals of HEWL produced after incubation of the protein in the presence of the metal compound, i.e. by cocrystallization (Crystals 1-4) (Table A, Appendix). Two structures were derived using datasets collected on crystals of  $[\text{Rh}_2(\text{OAc})_4]$ /HEWL adducts formed when metal-free HEWL crystals were exposed to solutions containing  $[\text{Rh}_2(\text{OAc})_4]$ , i.e. by soaking (Crystals 5-6). For cocrystallization experiments, crystals were grown in 20% ethylene glycol, 0,10 M sodium acetate buffer pH 4.5 and 0.60 M sodium nitrate. For soaking experiments, HEWL crystals were grown in the same condition used for cocrystallization (Crystal 5) or in 2.00 M sodium formate and 10 mM HEPES buffer pH 7.5 (Crystal 6).

### 4.2. X-ray structures of the $[\text{Rh}_2(\text{OAc})_4]$ /HEWL adducts prepared by cocrystallization

As expected, the four structures obtained by cocrystallization are quite similar to each other and to the structure of the metal-free HEWL. The overall features of HEWL are unaffected by the Rh binding. In fact, root mean square deviations of  $\text{C}\alpha$  atom positions ( $\text{C}\alpha$  rmsd) of the adduct and the native protein (PDB code: 193L)<sup>112</sup> range from 0.14 to 0.26 Å. The difference Fourier  $F_o - F_c$  electron density maps evidence a cleavage of the dirhodium compound upon the reaction with the protein. The partial occupancy ( $< 1.0$ ) of Rh atoms and conformational disorder prevented a detailed description of Rh ligands in almost all cases. Figure 4.1 reports the overall crystal structure of the  $[\text{Rh}_2(\text{OAc})_4]$ /HEWL adducts in the structure derived from Crystal 1 (Table A, Appendix), enlightening the Rh binding sites. Details of Rh binding sites are described in Table 1.

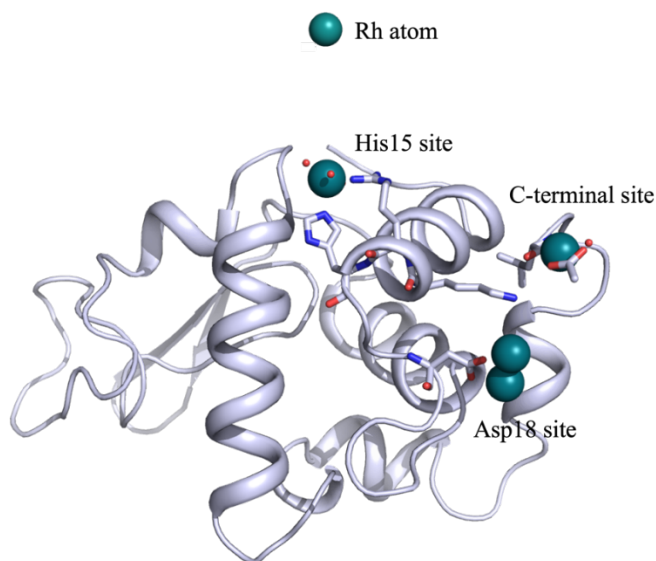


Figure 4.1. Identification of Rh binding sites in the overall  $[\text{Rh}_2(\text{OAc})_4]/\text{HEWL}$  adduct. Structure derived from Crystal 1 (Table A, Appendix).

In all the structures, a Rh monometallic fragment is found close to His15 and Arg14 side chains (Figure 4.2 A-D). His15 is involved in binding of several metal complexes.<sup>66</sup> The Rh centre, similarly to Pt, Ru, Au and Ag atoms,<sup>66,113</sup> is coordinated by the  $\text{N}\epsilon$  atom of the imidazole ring of the His side chain. Average measures on the HEWL structures revealed a Rh- $\text{N}\epsilon$  distance of 2.35 Å, comparable to the Rh-N distances observed in small molecules.<sup>9</sup> The Rh unit is coordinated also by Arg14 side chain in all the structures. In Crystal 1 (Figure 4.2 A) and 4 (Figure 4.2 D) two water molecules and an acetate ligand are coordinated to the Rh atom in a monodentate fashion. Rh atom in Crystal 2 is surrounded by an acetate ion and a water molecule (Figure 4.2 B). Around Rh fragment close to His15 in the Crystal 3 only an acetate ligand has been modelled (Figure 4.2 C). Since these ligands are located around the Rh atom in a distorted octahedral geometry, it has been deduced that one or more ligands are missing in the electron density maps.

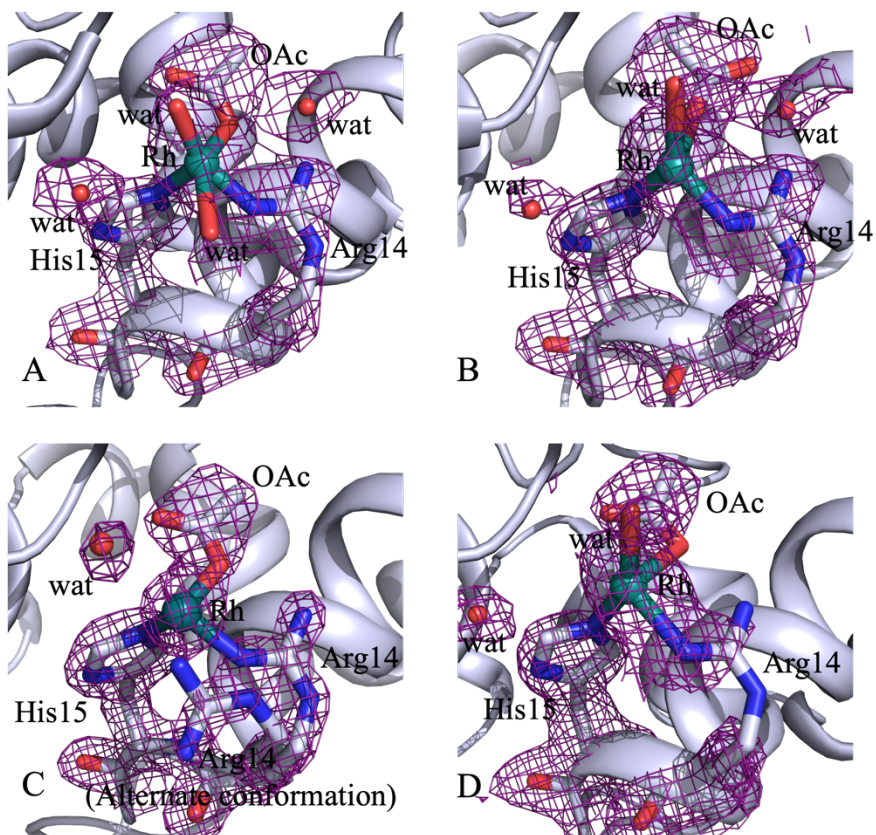


Figure 4.2. Details of Arg14/His15 binding sites in Crystals 1-4 (Panels A-D, respectively). 2Fo-Fc maps are contoured at  $1.0\sigma$  (purple). (wat = water).

Table 1. Rh binding sites for the structures of the  $[\text{Rh}_2(\text{OAc})_4]/\text{HEWL}$  adducts. The ligands at each Rh binding site are listed with their occupancy in parenthesis. \* indicates atoms present in symmetry related molecules.

$[\text{Rh}_2(\text{OAc})_4]/\text{HEWL}$ adduct ligands						
	Crystal 1	Crystal 2	Crystal 3	Crystal 4	Crystal 5	Crystal 6
	co-crystallization			soaking		
<b>His15 site</b>	Rh (0.35)	Rh (0.5)	Rh (0.3)	Rh (0.3)	Rh (0.25)	Rh (0.35)
	His15 (1)	His15 (1)	His15 (1)	His15 (1)	His15 (1)	His15 (1)
	Arg14 (1)	Arg14 (1)	Arg14	Arg14 (0.5)	Arg14	Arg14 (1)
	OAc (1)	OAc(1)	(0.5)	OAc (1)	(0.5)	H <sub>2</sub> O (0.35)
	H <sub>2</sub> O (0.35)	H <sub>2</sub> O (0.5)	OAc (1)	H <sub>2</sub> O (0.3)	OAc (1)	H <sub>2</sub> O (0.35)
	H <sub>2</sub> O (0.65)			H <sub>2</sub> O (0.3)	H <sub>2</sub> O (1)	
<b>C-ter site</b>	Rh (0.65)	Rh (0.65)	Rh (0.65)			
	Rh* (0.65)	Rh* (0.65)	Rh* (0.65)			
	Leu129 (1)	Leu129 (1)	Leu129 (1)	Rh (0.7)		Rh (0.45)
	Leu129* (1)	Leu129* (1)	Leu129* (1)	Rh* (0.7)		Rh* (0.45)
	Lys13 (1)	Lys13 (1)	Lys13 (1)	Leu129 (1)	Rh (0.4)	Leu129 (1)
	Lys13* (1)	Lys13* (1)	Lys13* (1)	Leu129* (1)	Rh* (0.4)	Leu129* (1)
	OAc (0.65)	OAc (0.65)	OAc (0.65)	Lys13 (1)	Leu129 (1)	Lys13 (1)
	OAc* (0.65)	OAc* (0.65)	OAc* (0.65)	Lys13* (1)	Leu129* (1)	Lys13* (1)
	H <sub>2</sub> O (0.65)	H <sub>2</sub> O (0.65)	H <sub>2</sub> O (0.65)	OAc (0.7)	Lys13 (1)	H <sub>2</sub> O (0.45)
	H <sub>2</sub> O* (0.65)	H <sub>2</sub> O* (0.65)	H <sub>2</sub> O* (0.65)	OAc* (0.7)	Lys13* (1)	H <sub>2</sub> O* (0.45)
				H <sub>2</sub> O (0.7)		
				H <sub>2</sub> O* (0.7)		
<b>Asp18 site</b>	Rh (0.40)	Rh (0.20)				Rh (0.40)
	Rh (0.40)	Rh (0.20)				Rh (0.40)
	Asp18 (1)	Asp18 (1)				Asp101 (1)
						H <sub>2</sub> O (0.40)
<b>Lys33 site</b>						Rh (0.20)
						Lys33 (1)
						OAc (0.33)
<b>Asn93 site</b>						Rh (0.30)
						Rh (0.30)
						Asn93 (1)
						Lys96 (1)
						H <sub>2</sub> O (1)

Rh-O bond length ranges from 1.91 to 2.67 Å. For small molecules this distance is in the range 2.0-2.2 Å,<sup>9</sup> thus, in the metal/protein adducts some distances are longer than usual. A good degree of protein metalation at this binding site is observed (occupancy between 0.30 and 0.50). Other Rh fragments are observed between two symmetry mates, close to the binary axis. In this binding site, two Rh atoms were observed at 3.22-3.42 Å. In all the structures, the metallic atoms are bound to the protein via C-terminal tail of two symmetry related molecules, the N $\zeta$  atoms of Lys13 water molecules and acetate ions (Figure 4.3).

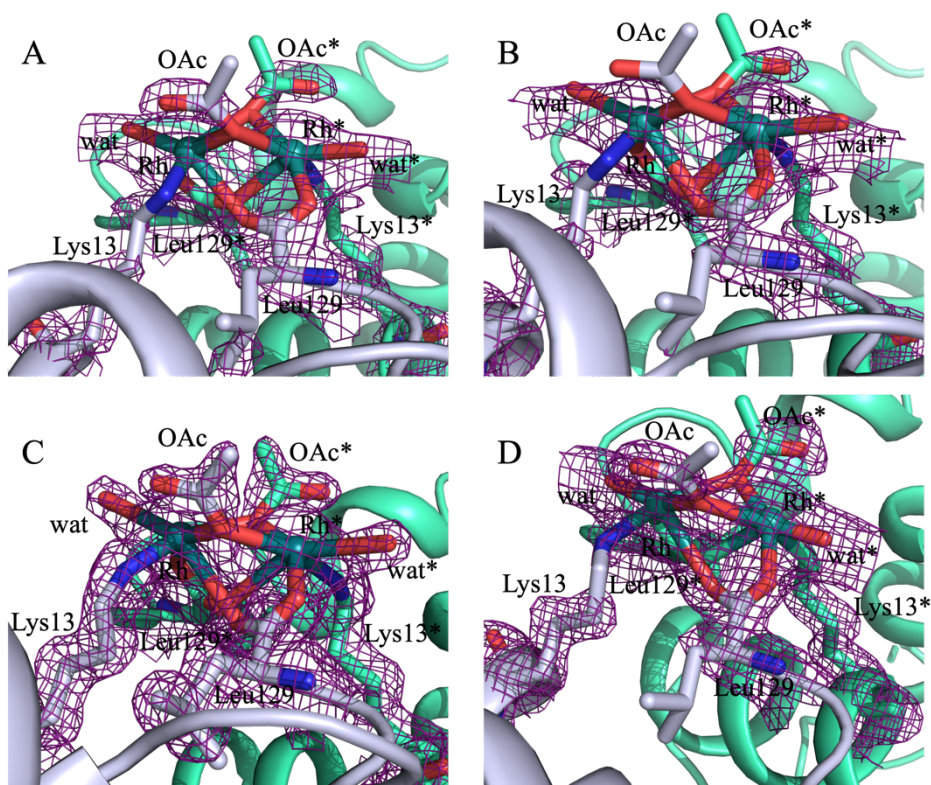


Figure 4.3. Details of Rh binding sites close to the C-terminal tails and Lys13 side chain in Crystals 1-4 (A-D, respectively). 2Fo-Fc electron density maps are contoured at 0.7 $\sigma$  (purple). \* refers to symmetry related molecules.

In Crystals 1, 2 and 4 the metal ligands are not well defined, however, the high occupancy (0.65-0.70) of Rh atoms indicates that the two Rh units are not alternative to each other. This high occupancy suggests that this is the main binding site of the metal compound, and it consists of a dimetallic unit. Since the distance of the two Rh atoms at this binding site is in the typical range of Rh(III)-Rh(III) dimeric species, a Rh(III)-O-Rh(III) structural motif, where carboxylate ligands of C-terminal tails and acetate ions act as bridging ligands between the two Rh atoms, was proposed. This hypothesis is supported by literature data: when  $[\text{Rh}_2(\text{OAc})_4]$  reacts with sodium thiolates in the presence of  $\text{O}_2$ , an oligomeric chain of Rh(III) ions that are bridged by three Rh-S-Rh bonds is formed, each with six Rh-S ( $2.36 \pm 0.02 \text{ \AA}$ ) bonds. In this oligomer, the distance between Rh ions is  $3.18 \pm 0.02 \text{ \AA}$  (Figure 4.4).<sup>114</sup>

This distance is in agreement with EXAFS data obtained for the aerobic reaction products formed in aqueous solution by  $[\text{Rh}_2(\text{OAc})_4]$  and glutathione.<sup>115</sup> However, HEWL does not contain free thiolate groups, hence, other agents should be responsible for the metal oxidation.

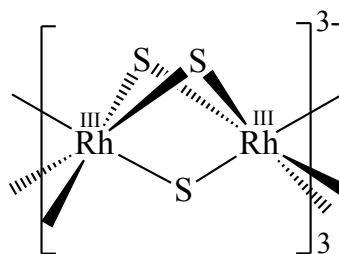


Figure 4.4. Schematic representation of the product obtained by the reaction of a dirhodium tetracarboxylate compound with a thiolate compound.

Since this binding site was observed at protein-protein interface, in principle it could act as a cross-linking agent between two symmetry mates (Figure 4.5). To verify this hypothesis, native HEWL crystals and crystals of  $[\text{Rh}_2(\text{OAc})_4]$ /HEWL adducts were dissolved and undertaken to SDS-PAGE analysis (Figure 4.6). Electrophoretic results revealed the existence of HEWL dimers only in the sample containing dissolved HEWL crystals treated with  $[\text{Rh}_2(\text{OAc})_4]$ . This indirectly validates the proposed structural motif. Furthermore, this result suggests that the dimetallic centre can induce the formation of protein dimers in the cellular milieu.

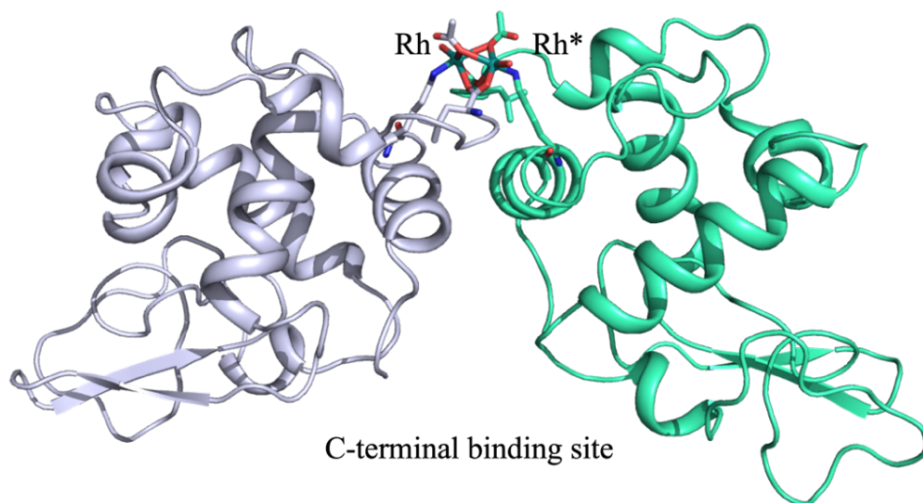


Figure 4.5. Dirhodium cross-linking of HEWL as revealed by crystal structure of the  $[\text{Rh}_2(\text{OAc})_4]/\text{HEWL}$  adduct in Crystal 1. \* Indicates symmetry related atoms.

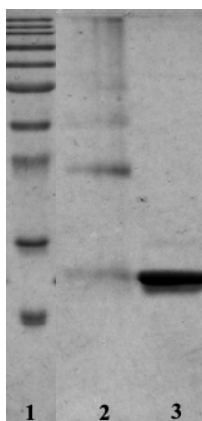


Figure 4.6. SDS-PAGE analysis of dissolved HEWL crystals. Line 1: markers. Line 2: dissolved crystals of  $\text{Rh}_2\text{OAc}_4/\text{HEWL}$  adduct. Line 3: dissolved native HEWL crystals.

CO releasing molecule CORM-2 ( $\text{Ru}_2\text{Cl}_4(\text{CO})_6$ ) and some Re complexes also bind HEWL C-terminal tail.<sup>116,117</sup> When the Ru complex reacts with HEWL, two Ru

atoms are found close to each other, like in the  $[\text{Rh}_2(\text{OAc})_4]/\text{HEWL}$  adduct, but, with an occupancy  $< 0.5$  (0.30 and 0.50, respectively).<sup>116</sup> In the structure of the HEWL adduct with Re, two metal atoms with 0.39 and 0.55 occupancy are bound to O atoms of the  $\text{COO}^-$  group with a Re-O distance of 2.1 and 2.7 Å.<sup>117</sup>

The four structures obtained by co-crystallization mainly differ close to Asp18 side chain, where two Rh atoms with low occupancy (0.20/0.20 and 0.40/0.40) are observed in two out of the four analysed structures (Crystal 1 and 2) (Figure 4.7).

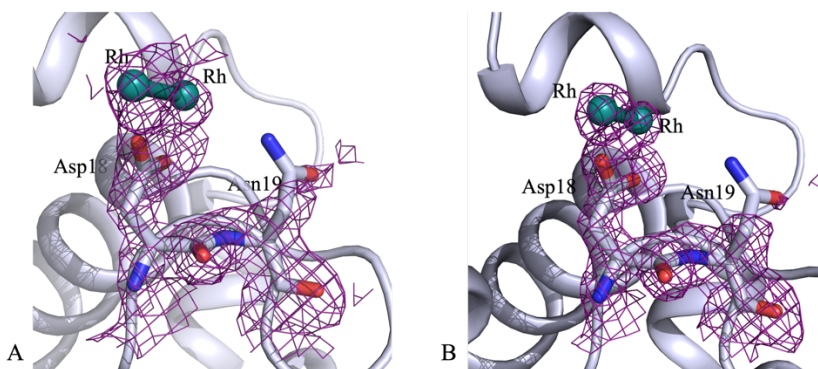


Figure 4.7. Details of Asp18 binding sites in Crystals 1 and 2 (panels A and B, respectively). 2Fo-Fc maps are contoured at  $1.0\sigma$  (purple).

The hypothesis that a single Rh fragment could occupy two alternate positions at this site cannot be excluded. However, the two Rh atoms have the same occupancy and similar B-factors ( $\Delta\text{B-factors} = 7.7\%$  and  $10.6\%$  in the two structures), moreover, they are at a distance comparable with the Rh-Rh bond distance of the dimetallic paddle-wheel complexes (2.31 and 2.48 Å),<sup>9</sup> hence, there is a strong possibility that a dimetallic unit is bound to the Asp18 side chain. Ligands at this binding site cannot be modelled, due to the low occupancy of Rh atoms. Other metal compounds form adducts with HEWL through the binding to Asp18 side chain.<sup>116,117</sup>

### 4.3. X-ray structures of the $[\text{Rh}_2(\text{OAc})_4]/\text{HEWL}$ adducts prepared by soaking

The two structures of  $[\text{Rh}_2(\text{OAc})_4]/\text{HEWL}$  adducts obtained by soaking were crystallised under different crystallization conditions. One structure is obtained from a crystal grown under the same crystallization conditions used for co-crystallization experiments at pH 4.5 (Crystal 5), while the other is obtained at pH 7.5 (Crystal 6).

The structure from Crystal 5 is very similar to those described in the previous paragraph ( $C\alpha$  rmsd = 0.19-0.24 Å). In fact, Rh atoms were bound to the protein via Arg14 and His15 side chains and close to the C-terminal carboxylate and Lys13 side chain (Figure 4.8). In particular, close to His15, a Rh monometallic fragment is coordinated also by Arg14 and an acetate ligand. The dimeric unit at interface between two symmetry related molecules is surrounded by two acetate ions and two water molecules. This result further demonstrates that soaking and co-crystallization procedures often provide similar results.<sup>84</sup>

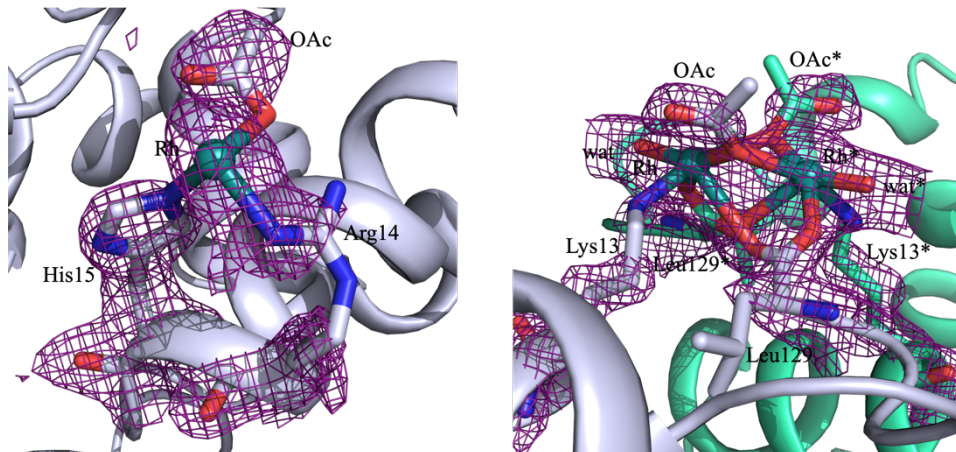


Figure 4.8. Details of Rh binding sites close to Asp18 (on the left) and C-terminal tails/Lys13 (on the right) in Crystal 5. From left to right, 2Fo-Fc maps are contoured at 1.0 and 0.7 $\sigma$  (purple). \* refers to symmetry related molecules.

Instead, the structure of the adduct from crystal 6, grown using 10 mM HEPES pH 7.5 and 2.00 M sodium formate, revealed unexpected results. In fact, beyond the previous described binding sites (Arg14/His15, Lys13/C-terminal tail), three

additional metal recognition sites were observed. In particular, Rh-containing fragments were found close to Asn93 and Lys96, Asp101 and Lys33 side chains (Figure 4.9).

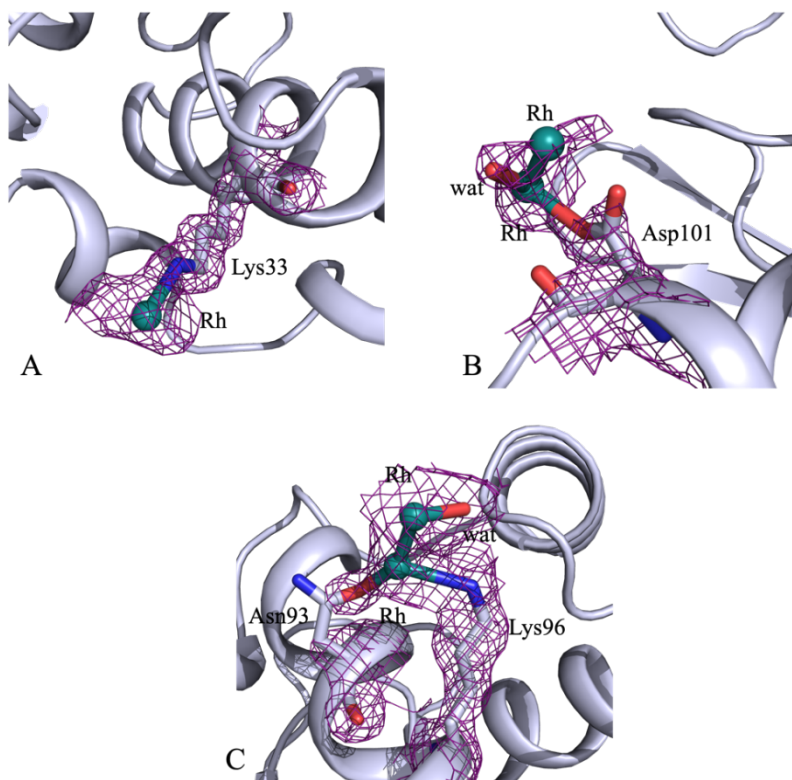


Figure 4.9. A. Details of binding sites near Lys33 (panel A), Asp101 (panel B) and Asn93 (panel C). 2Fo-Fc maps are contoured at  $1.0\sigma$  (purple).

This structure is quite similar to the previous described ones ( $C\alpha$  rmsd = 0.19-0.27 Å). Hence, the differences associated with Rh binding sites are not related to large variations of the overall protein structure.

A Rh atom is coordinated to N $\zeta$  atom of Lys33 (Figure 4.9 A). Two dimetallic units were found close to Asp101 and Asn93/Lys96 side chains (Figure 4.9 B and C, respectively). In the former binding site Rh atoms are at a distance of 2.29 Å each other, and 2.32-2.56 Å from O atoms of Asp side chain (Figure 4.9 B). A water molecule is found close to the Rh atom that is not bound to the protein. As

in the case of Asp18 binding site, the low occupancy of the metals prevents an unambiguous description of the binding site. In fact, the Rh-Rh distance suggests the possibility of a dirhodium centre bound to the protein. However, the possibility of a single Rh with two alternate positions cannot be excluded. The latter binding site also consists of a dimetallic centre with low occupancy (0.30/0.30). In this site, the Rh-Rh distance is 2.48 Å. One of the two Rh atoms is at distances of 2.42 and 2.80 Å from the side chains of Asn93 and Lys96, respectively (Figure 4.9 C). The other Rh is not bound to protein atoms, suggesting the possibility that a dirhodium core can be bound to the protein. Here, a water molecule is coordinated to the Rh fragment that is far from the protein.

These results indicate that the experimental condition used during the soaking plays a non-innocent role in directing the interaction between  $[\text{Rh}_2(\text{OAc})_4]$  and the proteins.

#### 4.4. Comparison of the $[\text{Rh}_2(\text{OAc})_4]$ /HEWL adducts with literature data

The six structures of the  $[\text{Rh}_2(\text{OAc})_4]$ /HEWL adduct here solved were compared with those obtained upon reaction of diruthenium tetraacetate  $[\text{Ru}_2(\text{OAc})_4]$  and  $\text{RhCl}_3$  with the same protein.<sup>118,104</sup> The overall protein conformation is conserved in these metal/protein adducts ( $C\alpha$  rmsd = 0.17-0.23 Å.)

In the structure of  $[\text{Ru}_2(\text{OAc})_4]$ /HEWL adduct the diruthenium centre is conserved upon the interaction with the protein: the Ru-Ru centre binds the Asp101 and Asp119 side chains, retaining the bridging carboxylate ligands and preserving the paddlewheel motif, in contrast to what was observed in the structures of the  $[\text{Rh}_2(\text{OAc})_4]$ /HEWL adducts above described (Figure 4.10). Hence, despite  $[\text{Ru}_2(\text{OAc})_4]$  and  $[\text{Rh}_2(\text{OAc})_4]$  compounds have similar structure they interact with HEWL in a very different way, under the same experimental conditions.<sup>118</sup>

Eight structures were obtained upon reaction of  $\text{RhCl}_3$  with HEWL (Figure 4.11).<sup>104</sup> These structures are different from those obtained when  $[\text{Rh}_2(\text{OAc})_4]$  reacts with the protein. The two metal/protein adduct structures share some common binding sites, close to Arg14/His15 and Asp18. However, in one of the structures of  $\text{RhCl}_3$ /HEWL adduct, the Rh atom bound to Asp18 side chain interacts also with Asn19 side chain. The main differences were found for the Rh atoms close to Asn46/Asp52, Asn65, Asp87 and Asp119 side chains.<sup>104</sup> These

binding sites were not found in the structures described in previous paragraphs. These results imply that the final metal binding sites are strongly influenced by Rh oxidation state and ligands. Hence, different Rh ligands can be used to direct the dirhodium-based compounds towards different protein binding sites or molecular targets.

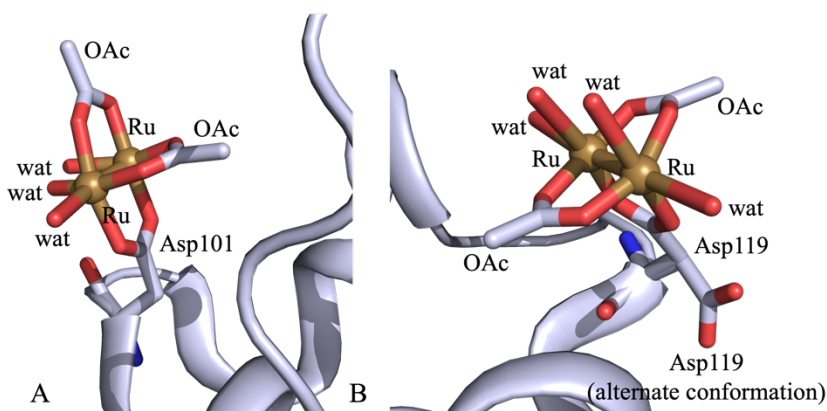


Figure 4.10.  $[\text{Ru}_2(\text{OAc})_4]$  binding site in its adduct with HEWL, close to Asp101 (panel A) and Asp119 (panel B).

The structures of the adduct formed by  $[\text{Rh}_2(\text{OAc})_4]$  with HEWL were also compared with the structure of the adduct that the compound forms with RNase A.<sup>81</sup> In the structure of  $[\text{Rh}_2(\text{OAc})_4]/\text{RNase A}$  adduct the whole  $[\text{Rh}_2(\text{OAc})_4]$  is coordinated at axial position to the side chain of His residues (Figure 2.15).<sup>81</sup> Thus, the interaction with proteins of this metal compound depends on the protein nature: dirhodium tetracarboxylates can interact with proteins retaining or losing their structures, thus forming both dimetallic and monometallic binding sites. Data also indicate that His side chains can coordinate both the whole  $[\text{Rh}_2(\text{OAc})_4]$  complex or Rh-containing monometallic fragments derived from the degradation of the initial compound.

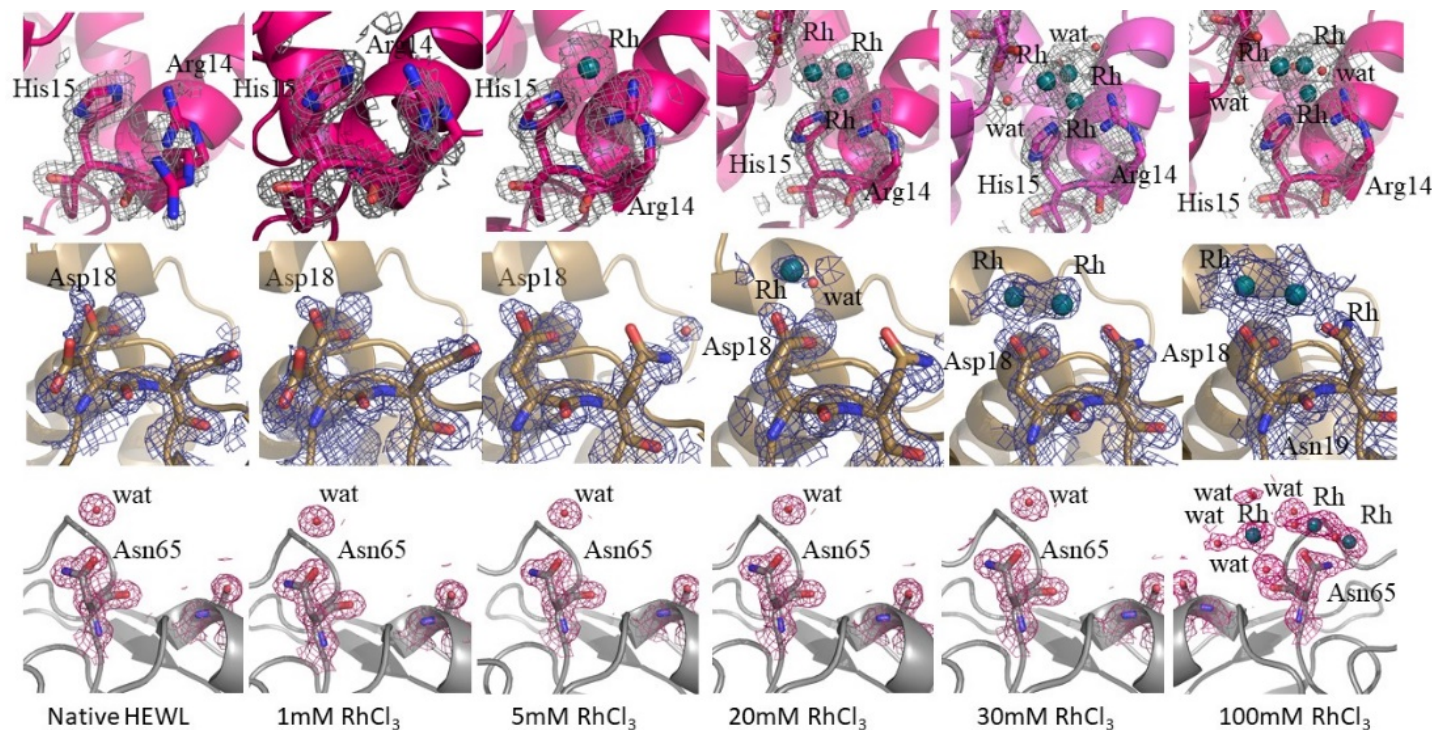


Figure 4.11. Rh binding sites close to His15 and Arg14, Asp18 and Asn19, Asn65 in the structures of HEWL in the presence of increasing amount of RhCl<sub>3</sub>.<sup>104</sup>

#### 4.5. Spectroscopic analysis of the interaction of $[\text{Rh}_2(\text{OAc})_4]$ with HEWL

The interaction between  $[\text{Rh}_2(\text{OAc})_4]$  and HEWL was also investigated in solution by UV-visible (UV-vis) absorption spectroscopy and circular dichroism (CD). UV-vis data revealed that the metal complex is stable over time in the crystallisation buffer used for growing HEWL crystals (Figure 4.12).

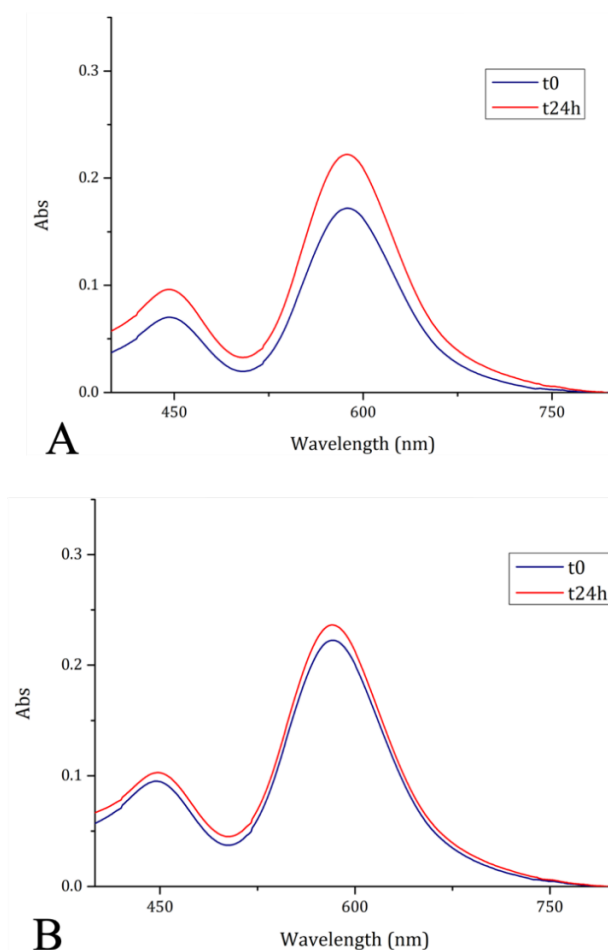


Figure 4.12. UV-vis absorption spectra of  $[\text{Rh}_2(\text{OAc})_4]$  in sodium acetate buffer pH 4.5 (panel A) and in 10 mM HEPES buffer pH 7.5 (panel B).

CD analysis revealed that HEWL is stable when incubated for 24 h with  $[\text{Rh}_2(\text{OAc})_4]$  at different metal to protein ratios (Figure 4.13).

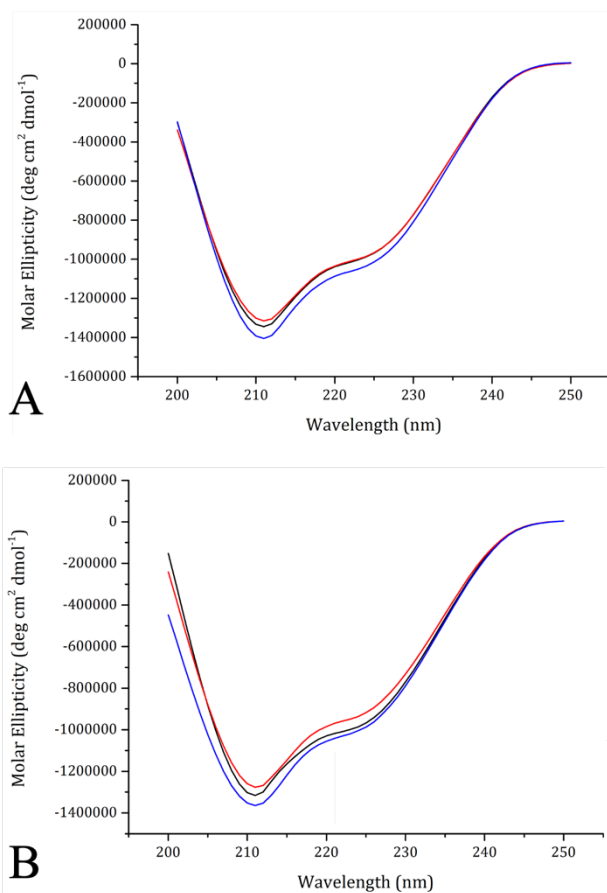


Figure 4.13. CD spectra of HEWL incubated for 24 h in the presence of  $[\text{Rh}_2(\text{OAc})_4]$  in 5 mM sodium acetate buffer pH 4.4 (panel A) and in 5 mM HEPES buffer pH 7.5 (panel B). Black lines refer to native protein. Red lines are derived from a 1:1 ratio of the metal/protein mixture. Blu lines indicate 3:1 ratio of the metal/protein mixture.

#### 4.6. Summary of the $[\text{Rh}_2(\text{OAc})_4]/\text{HEWL}$ adduct features

Six single crystal structures of the  $[\text{Rh}_2(\text{OAc})_4]/\text{HEWL}$  adduct obtained under three different experimental conditions were refined. Rare examples of structures of Rh/protein adducts were obtained from this investigation. The results indicate that the metal complex is partially degraded upon interaction with HEWL. The overall structure of HEWL is unaffected by the Rh-containing fragments binding to its scaffold. Multiple Rh binding sites were observed on the protein structure, with different occupancy, which can be related to different affinities of the Rh atoms for diverse protein portions. Monometallic fragments are found close to Arg14 and His15 side chains, Lys33 side chain (occupancy 0.25-0.50 and 0.20, respectively). Rh(II)-Rh(II) units are observed close to Asp18, Asp101, Asn93 and Lys96 side chains with low occupancy (0.30 on average). Close to C-terminal tails, a singular binding site is observed where a dimetallic centre with a Rh-Rh distance of 3.2-3.4 Å is bound to the carboxylate and Lys13 side chain at the interface between two symmetry-related molecules. The unusual long Rh-Rh distance was attributed to an oxidation of the metal atoms, with the two Rh atoms connected by O atoms of C-terminal carboxylate and acetate ions in a bridged fashion. The high occupancy of Rh atoms suggests that this is the main binding site of the metal compound in HEWL.

These data demonstrate that the Rh centres in the HEWL scaffold experience different environments, which could display a distinct reactivity if the metal/protein adduct is used as a homogeneous or heterogeneous catalyst (at crystalline state). These data suggest that the dirhodium compound could degrade upon reaction with proteins present in cellular milieu, inducing the formation of protein dimers and other aggregates. This could be related to the anticancer activity of the metal compound<sup>9</sup> since the binding of  $[\text{Rh}_2(\text{OAc})_4]$  to proteins could alter enzyme activity. Furthermore, different Rh binding sites could have different functional or biological role.

The Rh binding sites observed when  $[\text{Rh}_2(\text{OAc})_4]$  reacts with HEWL are different from those observed when  $\text{RhCl}_3$  interacts with the protein.<sup>104</sup> Hence, the fine tuning of ligands around a Rh core can be used to drive the interaction of Rh compounds towards different protein regions or different molecular targets, improving the performances of Rh-based complexes as potential drugs.

Comparison with literature data enlightens the different behaviour of  $[\text{Rh}_2(\text{OAc})_4]$  in interaction with HEWL and RNase A and reveals that  $[\text{Rh}_2(\text{OAc})_4]$  behaves differently from  $[\text{Ru}_2\text{Cl}(\text{OAc})_4]$ . The dirhodium compound degrades upon interaction with HEWL, while it retains its whole structure when it binds RNase A.<sup>81</sup> Furthermore, it is cleaved upon interaction with HEWL, while its Ru-based analogue retains its dimetallic structure in the adduct with the same protein. These findings revealed that Cys residues are not the only responsible for dirhodium tetracarboxylate decomposition.<sup>114,115</sup> Finally, from these results it emerges that when synthesizing  $[\text{Rh}_2(\text{OAc})_4]$ -based artificial metalloenzymes, the reaction products resulting from the enzyme functionalization should be carefully analysed from a structural point of view, since unexpected features could be obtained.

#### 4.7. Interaction of *cis*- $[\text{Rh}_2(\text{OAc})_2(\text{tfa})_2]$ with model proteins

Dirhodium tetracarboxylates bearing fluorinated bridging ligands have been reported as useful systems in several application fields.<sup>119,120,121</sup> The tfa ion is a better leaving group than OAc and its electron withdrawing ability enhances the Lewis acidity of dirhodium tetracarboxylates. Here, the effect of OAc substitution by tfa on the ability of the dirhodium compounds to bind proteins was investigated. In particular, the reactivity of *cis*- $[\text{Rh}_2(\text{OAc})_2(\text{tfa})_2]$  (Figure 4.14) with HEWL and RNase A was compared with that of dirhodium tetraacetate.

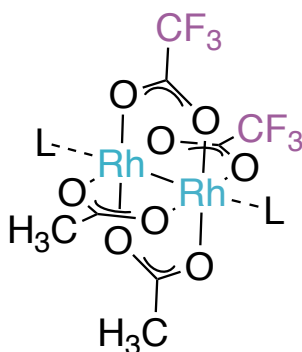


Figure 4.14. Depiction of the *cis*- $[\text{Rh}_2(\text{OAc})_2(\text{tfa})_2]$  structure. L refers to generic axial ligands.

*Cis*-[Rh<sub>2</sub>(OAc)<sub>2</sub>(tfa)<sub>2</sub>] was synthesised and its interaction with the two proteins was investigated in solution using a combination of physico-chemical techniques, which include UV-vis absorption spectroscopy, CD, and <sup>19</sup>F nuclear magnetic resonance spectroscopy (NMR). The metal/protein interaction was then also described in detail by X-ray crystallography. Four structures of *cis*-[Rh<sub>2</sub>(OAc)<sub>2</sub>(tfa)<sub>2</sub>]/RNase A adduct and one structure of *cis*-[Rh<sub>2</sub>(OAc)<sub>2</sub>(tfa)<sub>2</sub>]/HEWL adduct were solved. All the crystals were prepared by soaking. RNase A crystals were grown in 22% polyethylene glycol 4000 (PEG 4K) and 10 mM sodium citrate buffer pH 5.1, HEWL crystals were prepared using 2.00 M sodium formate and 10 mM HEPES buffer pH 7.5.

#### 4.8. Synthesis and NMR characterization of *cis*-[Rh<sub>2</sub>(OAc)<sub>2</sub>(tfa)<sub>2</sub>]

*Cis*-[Rh<sub>2</sub>(OAc)<sub>2</sub>(tfa)<sub>2</sub>] was synthesised through ligand exchange reaction starting from [Rh<sub>2</sub>(OAc)<sub>4</sub>], accordingly to a previous described procedure.<sup>121</sup> Briefly, [Rh<sub>2</sub>(OAc)<sub>4</sub>] is dissolved in trifluoroacetic acid (TFA) at room temperature for 2 h. This procedure provided the *cis*-[Rh<sub>2</sub>(OAc)<sub>2</sub>(tfa)<sub>2</sub>] compound in 64% yield. <sup>1</sup>H and <sup>19</sup>F NMR spectra of *cis*-[Rh<sub>2</sub>(OAc)<sub>2</sub>(tfa)<sub>2</sub>] closely match those previously reported elsewhere.<sup>121</sup>

#### 4.9. Stability of *cis*-[Rh<sub>2</sub>(OAc)<sub>2</sub>(tfa)<sub>2</sub>] in aqueous medium and in solution reactivity with RNase A and HEWL

UV-vis spectra of *cis*-[Rh<sub>2</sub>(OAc)<sub>2</sub>(tfa)<sub>2</sub>] were recorded over time in the absence and in the presence (Figure 4.15 and Figure 4.16) of RNase A and HEWL in the buffers used to grow crystals of the two proteins (10.0 mM sodium citrate buffer pH 5.1 and 5.0 mM HEPES pH 7.5, respectively). The spectral profile of *cis*-[Rh<sub>2</sub>(OAc)<sub>2</sub>(tfa)<sub>2</sub>] in sodium citrate pH 5.1 consists of two bands in the visible region, with maxima at 451 and 584 nm, respectively (Figure 4.15 A). The band at 451 nm can be assigned to Rh<sub>2</sub>(π\*) → Rh-O(σ\*) transitions, while that at 584 nm comes from the Rh<sub>2</sub>(π\*) → Rh<sub>2</sub>(σ\*) transition of the metal-metal single bond.<sup>81</sup> The band at λ<sub>max</sub> = 584 nm remains unaltered for 3 h, then, it is slightly red shifted up to 588 nm after 24 h. This slight shift suggests that the dimetallic centre is preserved under these conditions, in agreement with what was found for [Rh<sub>2</sub>(OAc)<sub>4</sub>].<sup>81</sup> Similarly, the band at λ<sub>max</sub> = 451 nm remains unchanged for 3 h,

but a blue shift from 451 to 444 nm is detected upon 24 h. This shift might arise from the ligand exchange process of tfa with solvent or buffer molecules. When *cis*-[Rh<sub>2</sub>(OAc)<sub>2</sub>(tfa)<sub>2</sub>] is in the presence of RNase A (Figure 4.15 B) under the same experimental conditions, a different behaviour is observed. Again, the spectral profile presents two bands in the visible region, at 449 and 576 nm. However, the over-time behaviour of the spectra reveals changes already after 30 min. In particular, a blue shift of the band at 449 nm, that disappears after 24 h, is observed. Concomitantly, the band with a minimum at 576 nm is red shifted up to 582 nm. Hence, the ligand exchange occurs faster in the presence of the protein, suggesting a possible interaction of protein residue side chains with the dimetallic complex. Furthermore, the data suggest that the Rh-Rh core is preserved upon interaction with the protein.

The spectral profiles of *cis*-[Rh<sub>2</sub>(OAc)<sub>2</sub>(tfa)<sub>2</sub>] in 5.0 mM HEPES pH 7.5 are very different from those described above (Figure 4.16 A). Under this condition, two bands are observed with  $\lambda_{\text{max}} = 452$  and 580 nm. Significant variations of these absorption maxima were recorded just after 30 min. A blue shift of the peak at 452 nm up to 408 nm was observed over time, with a concomitant increase in the absorbance. Simultaneously, the peak at 580 nm is blue shifted to 576 nm, with a decrease of the absorbance over time. An isosbestic point at 481 nm was observed from the spectra superimposition, which suggests an equilibrium phenomenon between two species in solution. These extensive variations of the spectral profiles over time could be explained considering significant structural variations of *cis*-[Rh<sub>2</sub>(OAc)<sub>2</sub>(tfa)<sub>2</sub>] under these conditions. The compound could retain the dimetallic core up to 3 h, going through degradation upon 24 h. It is worth to note that [Rh<sub>2</sub>(OAc)<sub>4</sub>] is stable under the same experimental conditions.<sup>81</sup>

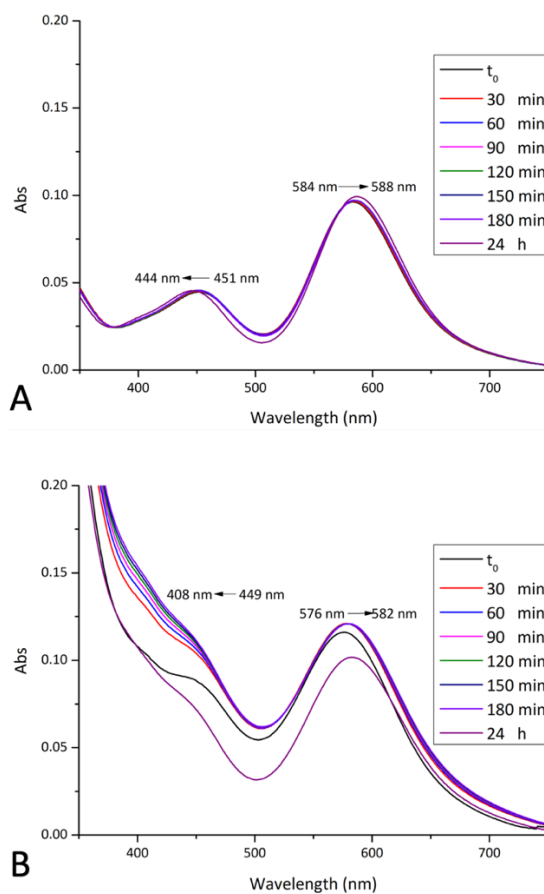


Figure 4.15. Time course UV-vis absorption spectra of *cis*-[Rh<sub>2</sub>(OAc)<sub>2</sub>(tfa)<sub>2</sub>] in 10.0 mM sodium citrate buffer pH 5.1 monitored over 24 h in the absence (panel A) and in the presence of RNase A (panel B). Metal/protein molar ratio = 3:1.

In the presence of HEWL (Figure 4.16 B), spectra change differently from those recorded in the absence of the protein under the same experimental conditions. Two peaks were observed at 446 and 577 nm, that undergo to large variations over time. The absorption maximum at  $\lambda_{\text{max}} = 577$  nm goes through a red shift from 577 to 495 nm with a decrease of intensity, while the absorbance of the band at 446 nm increases in intensity and disappears over time. Again, an isosbestic point at 621 nm arises from the superimposition of the spectra. Such large changes in the spectral profiles suggest that the dimetallic compound can degrade and that

the Rh-Rh bond can be cleaved upon interaction with HEWL, as observed in the crystal structures of the  $[\text{Rh}_2(\text{OAc})_4]/\text{HEWL}$  adducts described above. Moreover, the spectral differences found for the metal complex in the absence and in the presence of the protein under these experimental conditions suggest a possible irreversible interaction between the metal compound and HEWL.

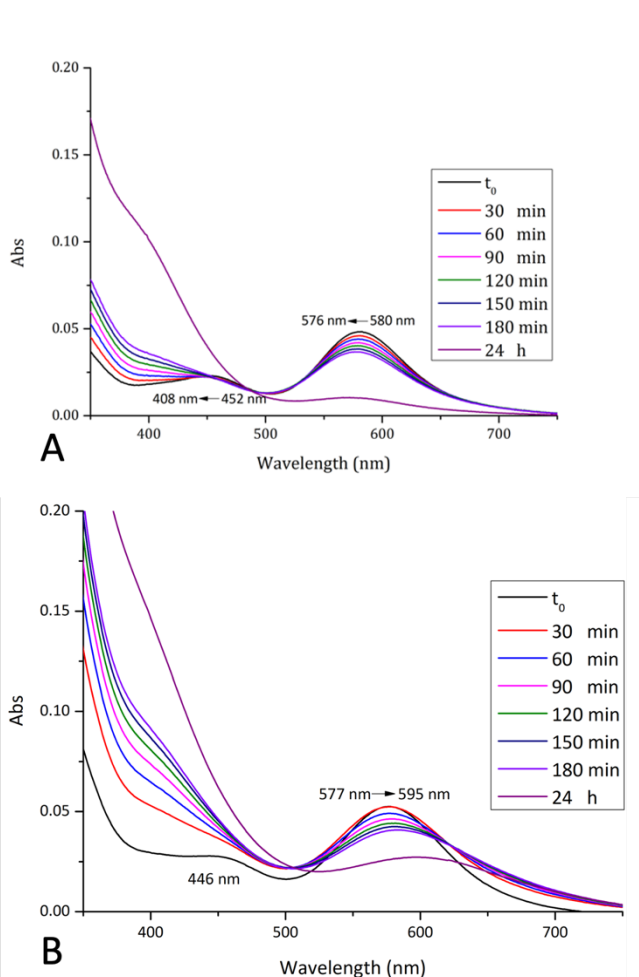


Figure 4.16. Time course UV-vis absorption spectra of *cis*- $[\text{Rh}_2(\text{OAc})_2(\text{tfa})_2]$  in 5.0 mM HEPES buffer pH 7.5 monitored over 24 h in the absence (panel A) and in the presence of HEWL (panel B). Metal/protein molar ratio = 3:1.

Since  $^{19}\text{F}$  nucleus is an excellent probe for the identification and quantification of chemical environments, a deeper understanding of ligand exchange process of *cis*- $[\text{Rh}_2(\text{OAc})_2(\text{tfa})_2]$  in aqueous media was obtained by collecting  $^{19}\text{F}$  NMR spectra over time. Spectra of *cis*- $[\text{Rh}_2(\text{OAc})_2(\text{tfa})_2]$  alone and in the presence of RNase A (Figure 4.17) and HEWL (Figure 4.18) were collected under the same experimental conditions described for the UV-vis analysis and compared with the spectrum of the pure TFA recorded in the same buffer solutions. The results revealed ligand exchange of tfa by solvent or buffer molecules over time: in both the explored experimental conditions, the metal compound completely releases all the tfa ligands after 24 h in the absence of the proteins. In the presence of the proteins the ligand exchange process occurs faster than in their absence. When RNase A is added to the solution, ligand exchange occurs just after 5 min, whereas 2 h are needed for the complete release of tfa in the presence of HEWL. These data further support the idea of a possible interaction between *cis*- $[\text{Rh}_2(\text{OAc})_2(\text{tfa})_2]$  and the two model proteins, as suggested by UV-vis spectroscopic measurements.

CD spectra of RNase A and HEWL incubated for 24 h with *cis*- $[\text{Rh}_2(\text{OAc})_2(\text{tfa})_2]$  in 1:3 protein/metal compound molar ratio revealed slight changes of molar ellipticities when compared to the spectra of the metal-free proteins, without extensive changes in the spectral profiles (Figure 4.19). Hence, it could be deduced that the presence of the metal compound can slightly affect the secondary structure of the two proteins leaving their overall folding unaltered.

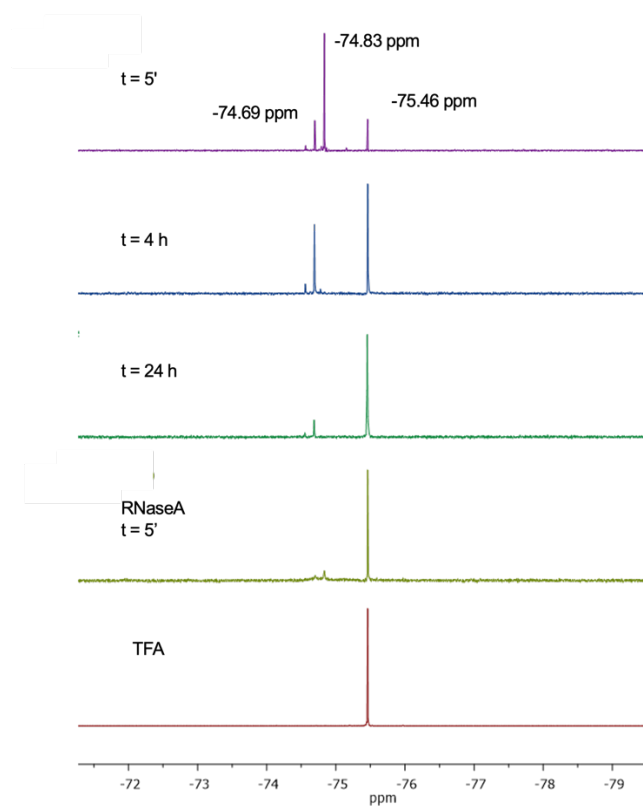


Figure 4.17. Time course  $^{19}\text{F}$  NMR spectra of *cis*- $[\text{Rh}_2(\text{OAc})_2(\text{tfa})_2]$  monitored over time (up to 24 h) in sodium citrate buffer pH 5.1 (10%  $\text{D}_2\text{O}$ ) in the absence and in the presence of RNase A (metal/protein ratio 1:1).

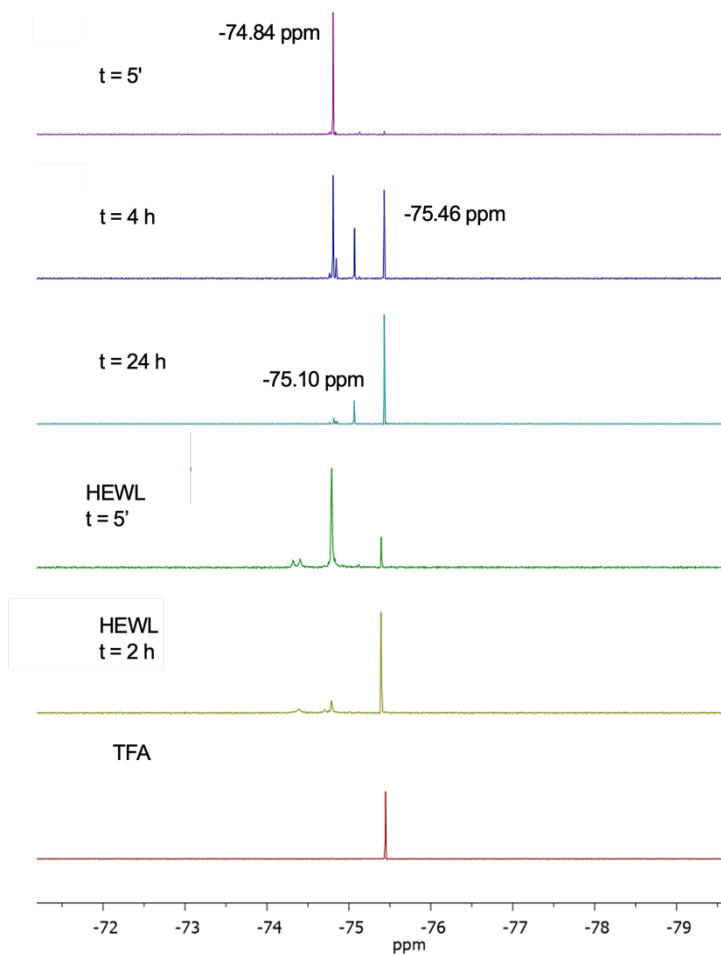


Figure 4.18 Time course  $^{19}\text{F}$  NMR spectra of *cis*- $[\text{Rh}_2(\text{OAc})_2(\text{tfa})_2]$  monitored over time (up to 24 h) in HEPES buffer pH 7.5 (10%  $\text{D}_2\text{O}$ ) in the absence and in the presence of HEWL (metal/protein ratio 1:1).

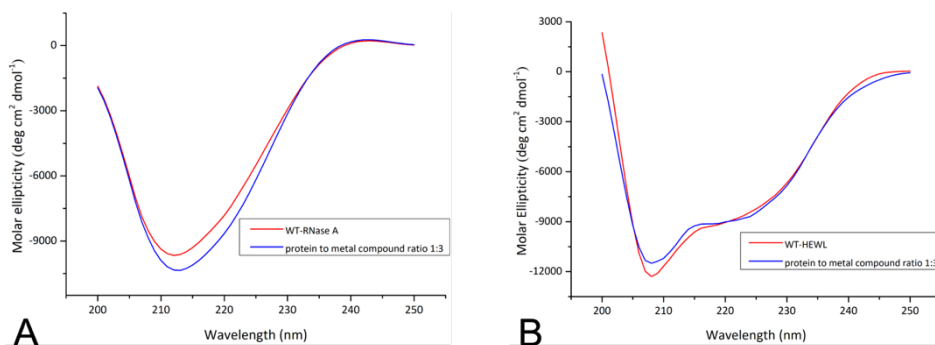


Figure 4.19. CD spectra of RNase A incubated for 24 h with *cis*-[Rh<sub>2</sub>(OAc)<sub>2</sub>(tfa)<sub>2</sub>] in 10 mM sodium citrate buffer pH 5.1 (panel A) and CD spectra of HEWL incubated for 24 h with *cis*-[Rh<sub>2</sub>(OAc)<sub>2</sub>(tfa)<sub>2</sub>] in 5 mM HEPES buffer pH 7.5 (panel B).

#### 4.10. X-ray structures of the *cis*-[Rh<sub>2</sub>(OAc)<sub>2</sub>(tfa)<sub>2</sub>]/RNase A adducts

Four different structures of the *cis*-[Rh<sub>2</sub>(OAc)<sub>2</sub>(tfa)<sub>2</sub>]/RNase A adducts were obtained by X-ray crystallography. Crystals of metal/protein adducts were prepared by exposing RNase A crystals to a solution of the metal compound for different soaking times and using slightly different soaking procedures (Appendix, Table B). X-ray diffraction data were collected at high resolution (1.15-1.45 Å) at XRD2 beamline of Elettra synchrotron in Trieste, Italy. Data collection and refinement statistics can be found in Table B (Appendix). As expected, the crystals contain two independent protein molecules in the asymmetric unit (molecule A and B) (Figure 4.20). Overall, the structures of *cis*-[Rh<sub>2</sub>(OAc)<sub>2</sub>(tfa)<sub>2</sub>]/RNase A adduct are very similar to each other, to the structure of the metal-free RNase A (PDB code: 1JVT)<sup>122</sup> and to the structure of the [Rh<sub>2</sub>(OAc)<sub>4</sub>]/RNase A adduct (C $\alpha$  rmsd = 0.07-0.45 Å, Table 2). Hence, the metal binding does not induce relevant changes to the protein structure.

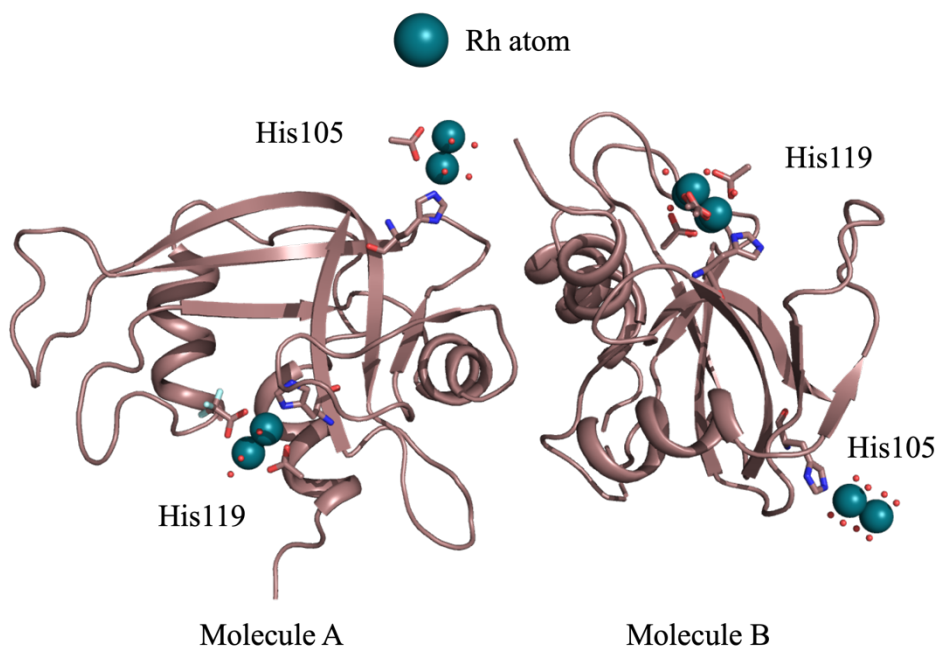


Figure 4.20. Overall structure of the two independent protein chains (molecule A and B) in the asymmetric unit of the crystals of *cis*-[Rh<sub>2</sub>(OAc)<sub>2</sub>(tfa)<sub>2</sub>]/RNase A adduct (from Structure 3, Table B).

As observed by <sup>19</sup>F NMR spectroscopy, there is a strong tendency of the metal compound to lose tfa ions upon interaction with the protein. In Structures 1, 2, and 4, (refer to Table B in the Appendix for the numbering scheme), dirhodium binding sites were found close to His119 side chains of molecules A and B and to His105 side chain of molecule A. In the Structure 3, (Table B, Appendix), the dimetallic compound is found close to the side chain of His119 and 105 of both the molecules A and B.

## RESULTS AND DISCUSSION

Table 2. Rmsd obtained by superimposition of C $\alpha$  of the structures of *cis*-[Rh<sub>2</sub>(OAc)<sub>2</sub>(tfa)<sub>2</sub>]/RNase A adduct each other, the native RNase A and the [Rh<sub>2</sub>(OAc)<sub>4</sub>]/RNase A adduct.

	Structure 1		Structure 2		Structure 3		Structure 4		6XVX		1JVT	
	Molecule A	Molecule B	Molecule A	Molecule B	Molecule A	Molecule B						
Structure 1												
Molecule A	0	0.341	0.108	0.358	0.082	0.398	0.058	0.353	0.384	0.084	0.208	0.380
Molecule B		0	0.423	0.069	0.382	0.106	0.310	0.061	0.105	0.378	0.352	0.212
Structure 2												
Molecule A			0	0.425	0.105	0.423	0.144	0.387	0.437	0.119	0.264	0.423
Molecule B				0	0.389	0.091	0.326	0.071	0.098	0.391	0.383	0.203
Structure 3												
Molecule A					0	0.406	0.082	0.385	0.412	0.077	0.233	0.390
Molecule B						0	0.306	0.077	0.077	0.397	0.390	0.187
Structure 4												
Molecule A							0	0.358	0.377	0.070	0.220	0.382
Molecule B								0	0.090	0.377	0.367	0.209
6XVX												

## RESULTS AND DISCUSSION

Molecule A	0	0.405	0.365	0.194
Molecule B		0	0.214	0.361
1JVT Molecule A			0	0.345
Molecule B				0

In the structures 1 and 2, His119 side chain adopts two distinct conformations in the molecule A, one of which is bound to a dirhodium centre at axial position (Figure 4.21 A, D). In the Structure 1 the other metal ligands are two acetate ions, one tfa ion and two water molecules at equatorial positions and a water molecule at the other axial position (occupancy = 0.55) (Figure 4.21 A). In the Structures 3 and 4, His119 side chain adopts a single conformation, with the imidazole ring that is coordinated to the same dimetallic fragment observed in the Structure 1, but with higher occupancy (0,80 and 0,75 respectively) (Figure 4.21 B and 3.21 C, respectively). In the Structure 2, this binding site is occupied by a dirhodium centre containing one acetate ion and six water molecules as equatorial ligands (Figure 4.21 D).

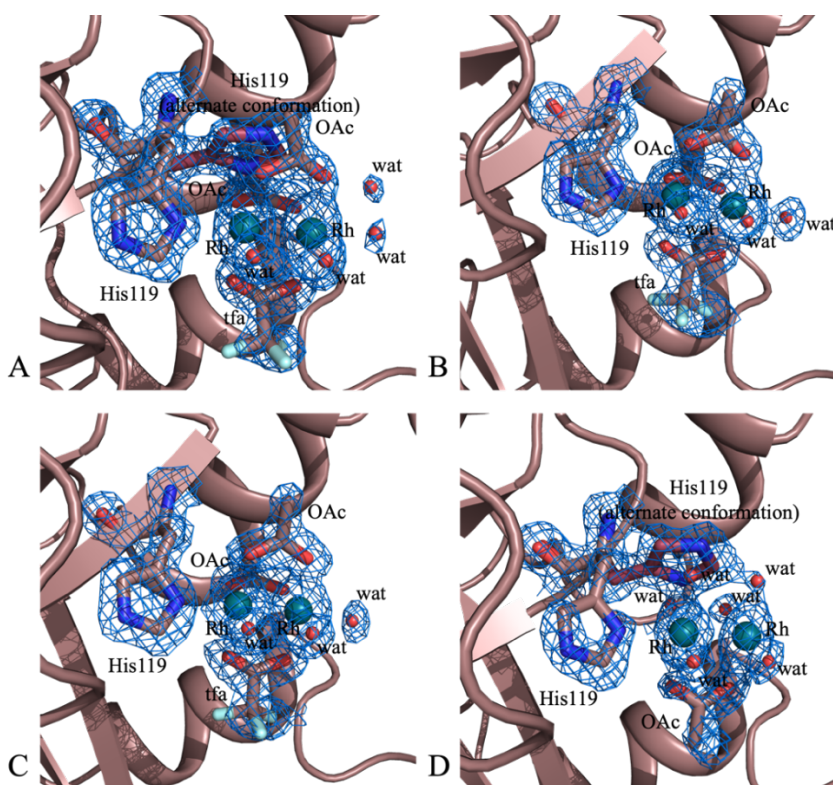


Figure 4.21. Details of the Rh binding sites close to His119 of molecule A in Structure 1 (panel A), Structure 3 (panel B), Structure 4 (panel C), Structure 2 (panel D). 2Fo-Fc electron density maps are contoured at  $0.7\sigma$  in panels A and D, and at  $1.0\sigma$  in panels B and C.

In molecule B, a single conformation of His119 is observed in all the structures. At this binding site, in the structures 1, 3 and 4, the dirhodium core adopts two alternate conformations and is surrounded by two acetate ions and four water molecules at equatorial position (Figure 4.22 A, B and C, respectively). In the Structure 2, this binding site is occupied by a dirhodium fragment with six water molecules and an OAc as equatorial ligands (Figure 4.22 D).

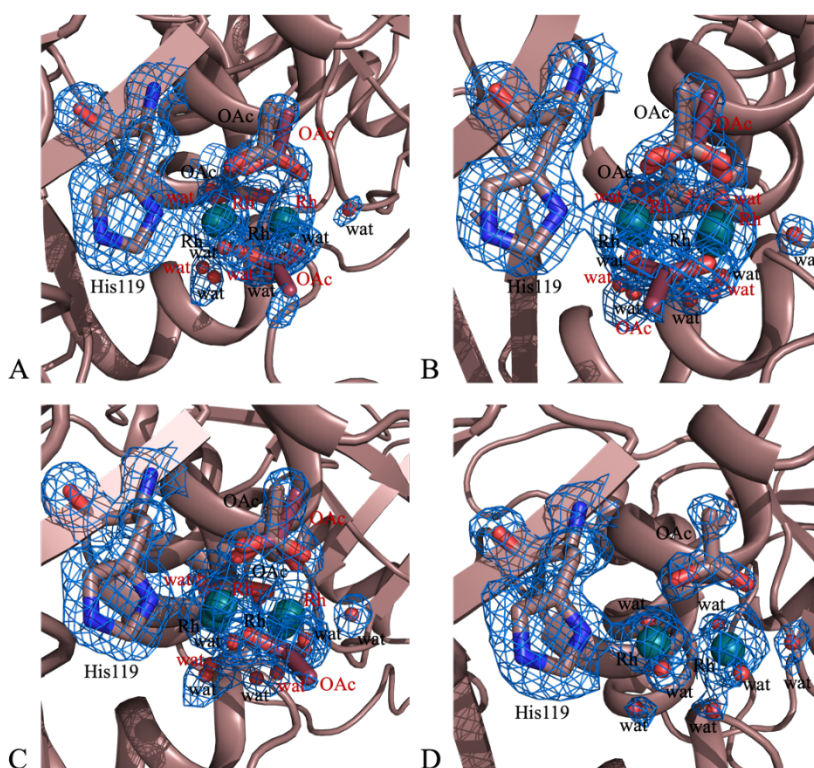


Figure 4.22. Details of the Rh binding site close to His119 of molecule B in Structure 1 (panel A), Structure 3 (panel B), Structure 4 (panel C) Structure 2 (panel D). Alternate conformations of the metal compound are labelled in red. 2Fo-Fc electron density maps are contoured at  $0.7\sigma$  in panels A and D, and at  $1.0\sigma$  in panels B and C.

Different dirhodium units were found near His105 side chain of molecule A. In structures 1 and 3, the dimetallic core is coordinated by one acetate and six water molecules (Figure 4.23 A and B, respectively), while in the structure 2 the Rh atoms are surrounded only by water molecules (Figure 4.23 C). In the structure 4, the dirhodium compound bears two acetate ions and four water molecules as equatorial ligands (Figure 4.23 D).

A detailed description of the metal binding sites and bond distances and geometries of the dirhodium fragments bound to the protein are summarised in Table 3 and Table 4. Bond distances and angles are in good agreement with those observed in small Rh-based dimetallic compounds.<sup>9</sup> It is worth to note that these binding sites have been found also in the structure of the adduct formed upon reaction of  $[\text{Rh}_2(\text{OAc})_4]$  with the protein.<sup>81</sup> However, in this latter case the acetate ions are fully retained by the metal compound upon interaction with the protein.

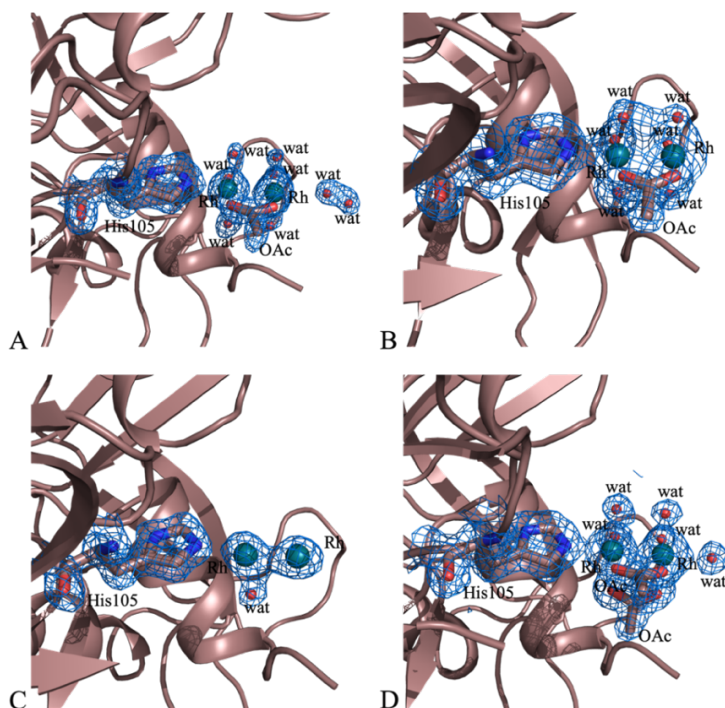


Figure 4.23. Details of the Rh binding site close to His105 of molecule A in Structure 1 (panel A), Structure 3 (panel B), Structure 2 (panel C) Structure 4 (panel D).

Figure 4.24 shows the binding site found close to His105 side chain in the molecule B. This binding site was metalated only in the structure 3 with a dirhodium unit coordinated by water molecules. 2Fo-Fc electron density maps are contoured at  $0.7\sigma$ .

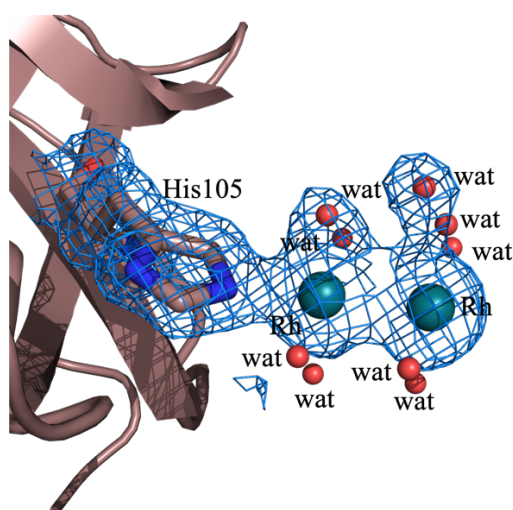


Figure 4.24. Details of the Rh binding sites close to His105 of molecule A in the Structure 3. 2Fo-Fc electron density maps are contoured at  $0.7\sigma$ .

Table 3. Summary of the Rh-containing fragments found in the five structures of Rh/protein adducts obtained upon reaction of *cis*-[Rh<sub>2</sub>(OAc)<sub>2</sub>(tfa)<sub>2</sub>] with RNase A or HEWL. The Rh ligands identified in each binding site are described with occupancy values in parentheses.

Rh/RNase A adduct binding site	Metal and Ligands in Structure 1	Metal and Ligands in Structure 2	Metal and Ligands in Structure 3	Metal and Ligands in Structure 4
His119 of molecule A (His in double conformation in structures 1 and 2)	Rh (0.55)	Rh (0.40)	Rh (0.80)	Rh (0.75)
	Rh (0.55)	Rh (0.40)	Rh (0.80)	Rh (0.75)
	OAc (0.55)	OAc (0.40)	OAc (0.80)	OAc (0.75)
	tfa (0.55)	H <sub>2</sub> O (0.40)	tfa (0.80)	tfa (0.75)

## RESULTS AND DISCUSSION

	H <sub>2</sub> O (0.55)	H <sub>2</sub> O (0.40)	H <sub>2</sub> O (0.80)	H <sub>2</sub> O (0.75)
	H <sub>2</sub> O (0.55)	H <sub>2</sub> O (0.40)	H <sub>2</sub> O (0.80)	H <sub>2</sub> O (0.75)
	H <sub>2</sub> O <sub>ax</sub> (0.55)	H <sub>2</sub> O (0.40)	H <sub>2</sub> O <sub>ax</sub> (0.80)	H <sub>2</sub> O <sub>ax</sub> (0.75)
		H <sub>2</sub> O (0.40)		
		H <sub>2</sub> O (0.40)		
<b>His119 of molecule B (His in double conformation in structure 2)</b>	Rh (0.20) (d.c.)	Rh (0.40)	Rh (0.30/0.30) (d.c.)	Rh (0.30/0.30) (d.c.)
	Rh (0.20) (d.c.)	Rh (0.40)		
	OAc (0.20) (d.c.)	OAc (0.40)	Rh (0.30/0.30) (d.c.)	Rh (0.30/0.30) (d.c.)
	OAc (0.20) (d.c.)	H <sub>2</sub> O (0.40)		
	H <sub>2</sub> O (0.20) (d.c.)	H <sub>2</sub> O (0.40)	OAc (0.30/0.30) (d.c.)	OAc (0.30/0.30) (d.c.)
	H <sub>2</sub> O (0.20) (d.c.)	H <sub>2</sub> O (0.40)	OAc (0.30/0.30) (d.c.)	OAc (0.30/0.30) (d.c.)
	H <sub>2</sub> O (0.20) (d.c.)	H <sub>2</sub> O (0.40)	OAc (0.30/0.30) (d.c.)	OAc (0.30/0.30) (d.c.)
	H <sub>2</sub> O (0.20) (d.c.)	H <sub>2</sub> O (0.40)	H <sub>2</sub> O (0.30/0.30) (d.c.)	H <sub>2</sub> O (0.30/0.30) (d.c.)
	H <sub>2</sub> O <sub>ax</sub> (0.40)	H <sub>2</sub> O (0.40)	H <sub>2</sub> O (0.30/0.30) (d.c.)	H <sub>2</sub> O (0.30/0.30) (d.c.)
		H <sub>2</sub> O <sub>ax</sub> (0.40)	H <sub>2</sub> O (0.30/0.30) (d.c.)	H <sub>2</sub> O (0.30/0.30) (d.c.)
			H <sub>2</sub> O (0.30/0.30) (d.c.)	H <sub>2</sub> O (0.30/0.30) (d.c.)
			H <sub>2</sub> O (0.30/0.30) (d.c.)	H <sub>2</sub> O (0.30/0.30) (d.c.)
			H <sub>2</sub> O <sub>ax</sub> (0.60)	H <sub>2</sub> O <sub>ax</sub> (0.60)
<b>His105 of molecule A</b>	Rh (0.40)	Rh (0.40)	Rh (0.70)	Rh (0.55)
	Rh (0.40)	Rh (0.40)	Rh (0.70)	Rh (0.55)
	OAc (0.40)	H <sub>2</sub> O (0.40)	OAc (0.70)	OAc (0.55)
	H <sub>2</sub> O (0.40)		H <sub>2</sub> O (0.70)	OAc (0.55)
	H <sub>2</sub> O (0.40)		H <sub>2</sub> O (0.70)	H <sub>2</sub> O (0.55)
	H <sub>2</sub> O (0.40)		H <sub>2</sub> O (0.70)	H <sub>2</sub> O (0.55)
	H <sub>2</sub> O (0.40)		H <sub>2</sub> O (0.70)	H <sub>2</sub> O (0.55)
	H <sub>2</sub> O (0.40)		H <sub>2</sub> O (0.70)	H <sub>2</sub> O (0.55)
	H <sub>2</sub> O <sub>ax</sub> (0.20) (d.c.)		H <sub>2</sub> O <sub>ax</sub> (0.70)	
<b>His105 of molecule B</b>	/	/	Rh (0.40)	/
			Rh (0.40)	
			H <sub>2</sub> O (0.40)	
			H <sub>2</sub> O (0.40)	
			H <sub>2</sub> O (0.40)	
			H <sub>2</sub> O (0.40)	
			H <sub>2</sub> O (0.40)	
			H <sub>2</sub> O (0.40)	
			H <sub>2</sub> O (0.40)	
<b>Rh/HEWL adduct binding site</b>	<b>Metal and Ligands in the structure</b>			
<b>His15</b>	Rh (0.50)			
	Rh (0.50)			
	H <sub>2</sub> O (0.50)			
<b>Asp101</b>	Rh (0.30)			
	H <sub>2</sub> O (0.30)			

d.c. and ax refer to double conformations and axial ligands, respectively. Values in parenthesis refer to a single conformation.

Table 4. Bond distances and angles of Rh-containing fragments in the *cis*-[Rh<sub>2</sub>(OAc)<sub>2</sub>(tfa)<sub>2</sub>]/RNase A adducts.

Structure	Rh/RNase A adducts				
	His119A	His119B	His105A	His105B	
<b>1</b>	Rh—N (Å)	2.25	2.11	2.16	
	Rh—Rh (Å)	2.38	2.41	2.50	
	Rh—O <sub>OAc</sub> <sup>a</sup> (Å)	2.09	2.10	2.12	
	Rh—O <sub>tfa</sub> <sup>a</sup> (Å)	2.09	/	/	
	Rh—O <sub>wat</sub> <sup>a</sup> (Å)	2.08	2.10	2.10	/
	O <sub>OAc</sub> —Rh—N <sup>a</sup> (°)	90.1	90.1	89.4	
	O <sub>tfa</sub> —Rh—N <sup>a</sup> (°)	87.3	/	/	
	N—Rh—Rh (°)	178.9	161.0	169.7	
	O <sub>wat</sub> —Rh—Rh <sup>a</sup> (°)	86.3	90.2	91.6	
	<b>2</b>	Rh—N (Å)	2.36	2.17	2.21
Rh—Rh (Å)		2.41	2.38	2.30	
Rh—O <sub>OAc</sub> <sup>a</sup> (Å)		2.12	2.11	/	
Rh—O <sub>tfa</sub> <sup>a</sup> (Å)		/	/	/	
Rh—O <sub>wat</sub> <sup>a</sup> (Å)		2.11	2.08	2.03	/
O <sub>OAc</sub> —Rh—N <sup>a</sup> (°)		81.9	97.4	/	
O <sub>tfa</sub> —Rh—N <sup>a</sup> (°)		/	/	/	
N—Rh—Rh (°)		176.1	173.63	165.4	
O <sub>wat</sub> —Rh—Rh <sup>a</sup> (°)		91.8	89.1	95.0	
<b>3</b>		Rh—N (Å)	2.25	2.16	2.11
	Rh—Rh (Å)	2.35	2.47	2.43	2.48
	Rh—O <sub>OAc</sub> <sup>a</sup> (Å)	2.10	2.10	2.13	/
	Rh—O <sub>tfa</sub> <sup>a</sup> (Å)	2.10	/	/	/
	Rh—O <sub>wat</sub> <sup>a</sup> (Å)	2.10	2.10	2.09	2.10
	O <sub>OAc</sub> —Rh—N <sup>a</sup> (°)	90.4	89.5	90.9	/
	O <sub>tfa</sub> —Rh—N <sup>a</sup> (°)	90.2	/	/	/
	N—Rh—Rh (°)	179.0	159.5	170.0	176.6
	O <sub>wat</sub> —Rh—Rh <sup>a</sup> (°)	87.8	89.9	91.1	89.7
	<b>4</b>	Rh—N (Å)	2.27	2.30	2.20
Rh—Rh (Å)		2.36	2.39	2.42	
Rh—O <sub>OAc</sub> <sup>a</sup> (Å)		2.10	2.10	2.10	
Rh—O <sub>tfa</sub> <sup>a</sup> (Å)		2.12	/	/	
Rh—O <sub>wat</sub> <sup>a</sup> (Å)		2.11	2.11	2.10	/
O <sub>OAc</sub> —Rh—N <sup>a</sup> (°)		90.8	89.9	91.7	
O <sub>tfa</sub> —Rh—N <sup>a</sup> (°)		87.5	/	/	
N—Rh—Rh (°)		179.4	159.0	175.6	
O <sub>wat</sub> —Rh—Rh <sup>a</sup> (°)		89.5	92.6	90.4	
<b>Structure of the [Rh<sub>2</sub>(OAc)<sub>4</sub>]/RNase A adduct</b>		Rh—N (Å)	2.16	2.27	2.20
	Rh—Rh (Å)	2.34	2.37	2.42	2.42
	Rh—O <sub>OAc</sub> <sup>a</sup> (Å)	2.09	2.11	2.06	2.13
	Rh—O <sub>tfa</sub> <sup>a</sup> (Å)	/	/	/	/
	Rh—O <sub>wat</sub> <sup>a</sup> (Å)	2.24	2.28	2.29	2.28
	O <sub>OAc</sub> —Rh—N <sup>a</sup> (°)	93.7	93.9	94.4	92.5
	O <sub>tfa</sub> —Rh—N <sup>a</sup> (°)	90.9	91.9	91.1	93.3
	N—Rh—Rh (°)	177.1	175.4	176.3	176.6
	O <sub>wat</sub> —Rh—Rh <sup>a</sup> (°)	90.1	88.0	88.9	87.3

<sup>a</sup> Average values. Standard deviations for the distances are in the range of 0.00-0.04 Å. Standard deviations for the angles are in the range of 1.4-7.8 °.

#### 4.11. X-ray structure of the *cis*-[Rh<sub>2</sub>(OAc)<sub>2</sub>(tfa)<sub>2</sub>]/HEWL adduct

The structure of the [Rh<sub>2</sub>(OAc)<sub>4</sub>]/HEWL adduct obtained by soaking in 10 mM HEPES pH 7.5 and 2.00 M sodium formate revealed a cleavage of the dimetallic centre, with formation of monometallic and bimetallic Rh fragments near the side chains of Arg14/His15, Lys13/C-terminal tail, Lys33, Asp101 and Asn94/Lys96. *cis*-[Rh<sub>2</sub>(OAc)<sub>2</sub>(tfa)<sub>2</sub>]/HEWL adduct crystals were obtained under the same conditions. The structure of this adduct was refined at 1.48 Å resolution. Superimposition of this structure with those of metal-free HEWL (PDB code: 193L)<sup>112</sup> and of the [Rh<sub>2</sub>(OAc)<sub>4</sub>]/HEWL adduct obtained under the same experimental conditions revealed that the overall protein 3D conformation in the crystals is not affected by the interaction with *cis*-[Rh<sub>2</sub>(OAc)<sub>2</sub>(tfa)<sub>2</sub>] (Cα rmsd = 0.15 and 0.13 Å) (Figure 4.25).

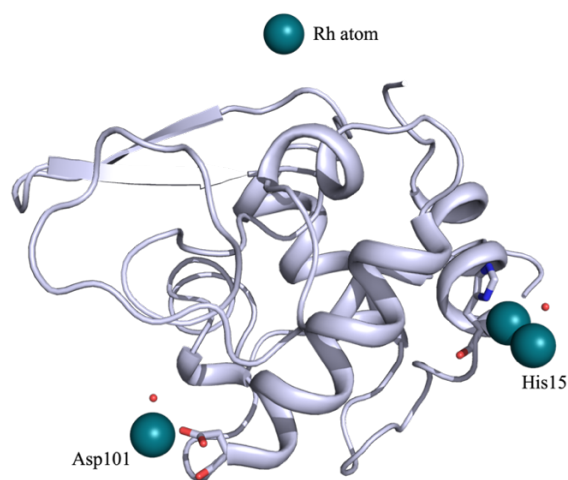


Figure 4.25. Overall structure of the *cis*-[Rh<sub>2</sub>(OAc)<sub>2</sub>(tfa)<sub>2</sub>]/HEWL adduct.

Nevertheless, Rh fragments arisen from the interaction of *cis*-[Rh<sub>2</sub>(OAc)<sub>2</sub>(tfa)<sub>2</sub>] with HEWL are different from those observed when [Rh<sub>2</sub>(OAc)<sub>4</sub>] reacts with the protein. In the structure of the *cis*-[Rh<sub>2</sub>(OAc)<sub>2</sub>(tfa)<sub>2</sub>]/HEWL adduct a dirhodium fragment is coordinated to the N $\delta$  atom of His15 (occupancy 0.50, Figure 4.26), while a monometallic fragment was found at this binding site for the [Rh<sub>2</sub>(OAc)<sub>4</sub>]/HEWL adduct. However, the possibility of a Rh-Rh bond cleavage over time at this binding site cannot be excluded. In fact, the coordination sphere of the dirhodium core at this binding site is not well defined in the electron density map, and only a water molecule has been added to the model.

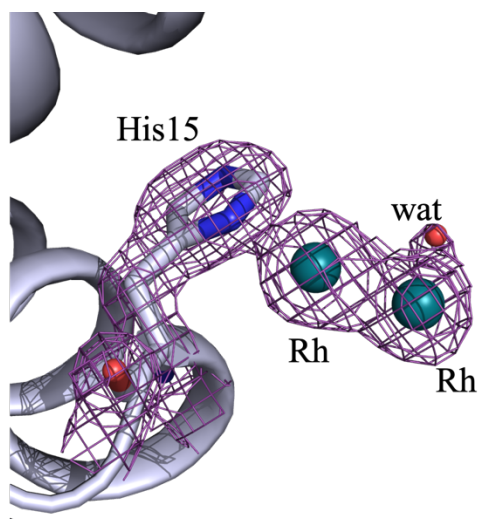


Figure 4.26. Details of Rh binding site close to His15 side chain. 2Fo-Fc electron density maps are contoured at  $0.7\sigma$ .

The idea of a dirhodium core degradation at this site is strongly supported by the presence, in this structure, of a monometallic unit near the of Asp101 side chain (Figure 4.27).

The occupancy of Rh atom at this site is 0.30. Refinements of models with higher occupancy values at this site show a decrease in the *R*factor but provide unrealistic

B-factor values ( $> 90 \text{ \AA}^2$ ) when compared to the B-factor of the O $\delta$ 2 atom of Asp101 ( $34 \text{ \AA}^2$ ) that coordinates the metal fragment.

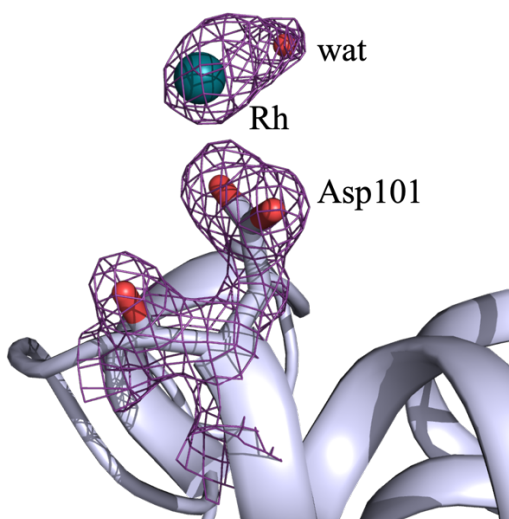


Figure 4.27. Details of Rh binding site close to Asp101 side chain. 2Fo-Fc electron density maps are contoured at  $0.7\sigma$ .

#### 4.12. Summary of the interaction of *cis*-[Rh<sub>2</sub>(OAc)<sub>2</sub>(tfa)<sub>2</sub>] with model proteins

The replacement of equatorial ligands around a dirhodium tetracarboxylate compound strongly affects its properties. The reactivity of these complexes towards biological macromolecules can be tuned by changing the ligands surrounding the dirhodium core, leading to the potential development of selective biological targeting agents.

Although the cytotoxicity of these compounds and their reactivity toward DNA is well-documented,<sup>123,124</sup> little is known in this field about dirhodium compounds bearing tfa ligands in their paddlewheel scaffold.

Hence, the interaction of *cis*-[Rh<sub>2</sub>(OAc)<sub>2</sub>(tfa)<sub>2</sub>] with RNase A and HEWL were investigated both in solution and in the solid state. <sup>19</sup>F NMR and UV-vis absorption spectroscopies indicate that ligand exchange of tfa ions with solvent molecules occurs faster in solution when the metal complex is in the presence of the two proteins, suggesting a possible interaction of the metal complex with the macromolecules. <sup>19</sup>F NMR data evidenced that *cis*-[Rh<sub>2</sub>(OAc)<sub>2</sub>(tfa)<sub>2</sub>] loses all the fluorinated ligands just after few minutes in the presence of RNase A, and after 2 h in the presence of HEWL.

Five crystal structures of the adduct formed upon reaction of *cis*-[Rh<sub>2</sub>(OAc)<sub>2</sub>(tfa)<sub>2</sub>] with RNase A and HEWL provided relevant insights in the reactivity of this metal complex with proteins. The binding of the metal compound to the two proteins does not alter their overall conformation, as observed in all the known Rh-based/protein adducts observed in solution and in the solid state. The reactivity of *cis*-[Rh<sub>2</sub>(OAc)<sub>2</sub>(tfa)<sub>2</sub>] and [Rh<sub>2</sub>(OAc)<sub>4</sub>] with proteins is similar. In fact, these complexes have a strong preference to bind His side chains at their axial position, but Asp side chains can also be metalated. However, some differences also emerge. In the interaction with RNase A, [Rh<sub>2</sub>(OAc)<sub>4</sub>] retains its equatorial ligands, while *cis*-[Rh<sub>2</sub>(OAc)<sub>2</sub>(tfa)<sub>2</sub>] loses its tfa ions. Furthermore, the stability in aqueous media of the latter compound strongly depends on the experimental conditions. The interaction of proteins with dirhodium complexes via axial ligation alters their reactivity and catalytic activity. In fact, when a rhodium carbene intermediate (Scheme 1) is formed, axial ligation opposite to the Rh-C unit significantly affects the reactivity of the metal-carbene intermediate.<sup>125</sup> This is due to the changes in the electronic and structural features of the dirhodium core arisen by the axial ligation.<sup>126</sup> In fact, dirhodium complexes with improved catalytic features have been prepared using hindered ligands that preclude the axial coordination of the dirhodium core.<sup>127</sup>

The data here reported can be helpful in designing experiments devoted to the preparation of dirhodium-based artificial metalloenzymes. Moreover, X-ray structures of the *cis*-[Rh<sub>2</sub>(OAc)<sub>2</sub>(tfa)<sub>2</sub>]/protein adducts here described increase the number of Rh/protein adducts reported in literature, that is scarce.<sup>128</sup> Finally, this analysis suggests that protein crystals are interesting candidates as immobilization platforms of dirhodium centres for heterogeneous catalysis.

#### 4.13. Interaction of $[\text{Rh}_2(\text{OAc})(\text{tfa})_3]$ with model proteins

Since the tfa ions facilitate the hydrolysis of dirhodium paddlewheel compounds, the effect of additional tfa in directing the interaction between these complexes and proteins was also evaluated. In particular, RNase A and HEWL were selected as model systems to study the interaction of  $[\text{Rh}_2(\text{OAc})(\text{tfa})_3]$  with proteins. The results were compared with those obtained upon reaction of *cis*- $[\text{Rh}_2(\text{OAc})_2(\text{tfa})_2]$  and  $[\text{Rh}_2(\text{OAc})_4]$  with the same proteins. As in the case of *cis*- $[\text{Rh}_2(\text{OAc})_2(\text{tfa})_2]$ , the interaction of  $[\text{Rh}_2(\text{OAc})(\text{tfa})_3]$  with RNase A and HEWL was investigated both in solution and in the solid state through UV-vis absorption spectroscopy, CD,  $^{19}\text{F}$  MNR and X-ray crystallography. In this frame, two crystal structures of the  $[\text{Rh}_2(\text{OAc})(\text{tfa})_3]$ /RNase A adduct and one crystal structure of the  $[\text{Rh}_2(\text{OAc})(\text{tfa})_3]$ /HEWL adduct were solved (Table C, Appendix).

#### 4.14. Synthesis and characterization of $[\text{Rh}_2(\text{OAc})(\text{tfa})_3]$

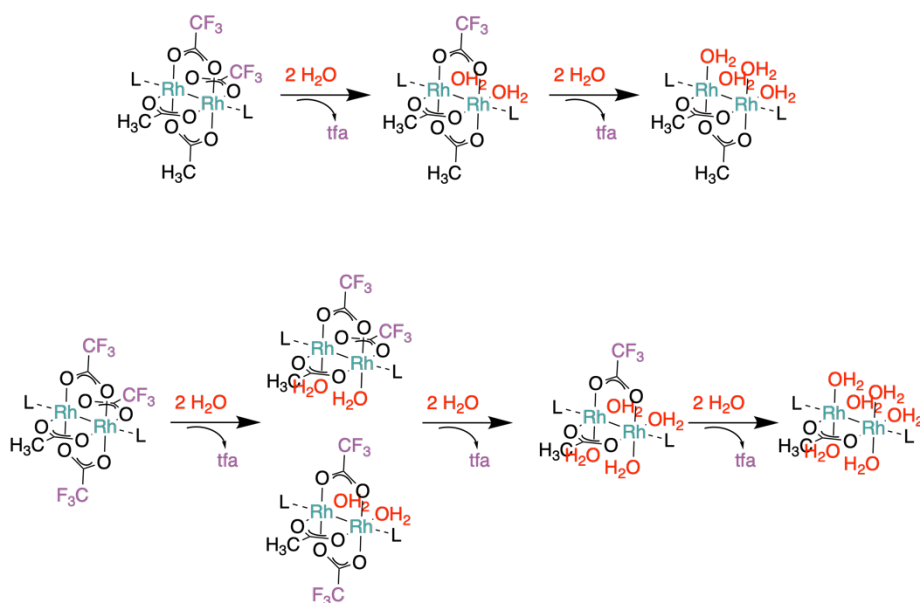
The same synthetic strategy used to prepare *cis*- $[\text{Rh}_2(\text{OAc})_2(\text{tfa})_2]$  was employed for preparing  $[\text{Rh}_2(\text{OAc})(\text{tfa})_3]$ .  $[\text{Rh}_2(\text{OAc})_4]$  was treated with an excess of TFA at room temperature for 6 h. The  $[\text{Rh}_2(\text{OAc})(\text{tfa})_3]$  was obtained in a good yield (55%) as a blue powder. The metal compound was characterised by  $^1\text{H}$  and  $^{19}\text{F}$  NMR, according to previous reported data.<sup>121</sup>

#### 4.15. Stability of $[\text{Rh}_2(\text{OAc})(\text{tfa})_3]$ in aqueous media and in solution reactivity with RNase A and HEWL

Stability of  $[\text{Rh}_2(\text{OAc})(\text{tfa})_3]$  in aqueous solution was investigated under the crystallization buffers used to grow crystals of RNase A and HEWL (10.0 mM sodium citrate buffer pH 5.1 and 5.0 mM HEPES buffer pH 7.5). The behaviour of  $[\text{Rh}_2(\text{OAc})(\text{tfa})_3]$  in these aqueous media was studied in the absence and in the presence of RNase A and HEWL as done above for *cis*- $[\text{Rh}_2(\text{OAc})_2(\text{tfa})_2]$ .

The electron absorption spectrum of  $[\text{Rh}_2(\text{OAc})(\text{tfa})_3]$  in sodium citrate at pH 5.1 reveals two bands in the visible region at 458 and 583 nm. Following the

assignment described for *cis*-[Rh<sub>2</sub>(OAc)<sub>2</sub>(tfa)<sub>2</sub>], the two bands were attributed to Rh<sub>2</sub>(π\*) → Rh-O(σ\*) and Rh<sub>2</sub>(π\*) → Rh<sub>2</sub>(σ\*) transitions, respectively (Figure 4.28 A). The spectral profile of [Rh<sub>2</sub>(OAc)(tfa)<sub>3</sub>] recorded over time under these conditions was similar to that observed for *cis*-[Rh<sub>2</sub>(OAc)<sub>2</sub>(tfa)<sub>2</sub>]. In fact, spectral changes are observed after 3 h and continue until 24 h. Specifically, the band at 458 nm is blue-shifted up to 407 nm whereas the band at 583 nm is red-shifted up to 588 nm. These changes could be related to the equatorial ligand exchange of tfa ligands by solvent molecules. Comparing Figure 4.28 A and Figure 4.15 A it can be concluded that [Rh<sub>2</sub>(OAc)(tfa)<sub>3</sub>] and *cis*-[Rh<sub>2</sub>(OAc)<sub>2</sub>(tfa)<sub>2</sub>] have a different behaviour under the same experimental conditions. In fact, while the spectrum of *cis*-[Rh<sub>2</sub>(OAc)<sub>2</sub>(tfa)<sub>2</sub>] shows a distinct band at 444 nm after 24 h, in the spectrum of [Rh<sub>2</sub>(OAc)(tfa)<sub>3</sub>] a broad signal is observed at 407 nm after 24 h. This difference could be explained considering that [Rh<sub>2</sub>(OAc)(tfa)<sub>3</sub>] provides several hydrolysis products over time (Scheme 3).



Scheme 3. Products of hydrolysis of *cis*-[Rh<sub>2</sub>(OAc)<sub>2</sub>(tfa)<sub>2</sub>] (up) and [Rh<sub>2</sub>(OAc)(tfa)<sub>3</sub>] (down)

When  $[\text{Rh}_2(\text{OAc})(\text{tfa})_3]$  is in the presence of RNase A (Figure 4.28 B) the spectrum changes more rapidly than in the absence of the protein. In fact, when the metal complex is in the presence of RNase A, the band at 444 nm is not observed, and a red-shift of the band at 566 up to 580 nm is observed upon 24 h. Hence, an instantaneous exchange of tfa ligands in the presence of protein could occur, leaving the dimetallic core unperturbed.

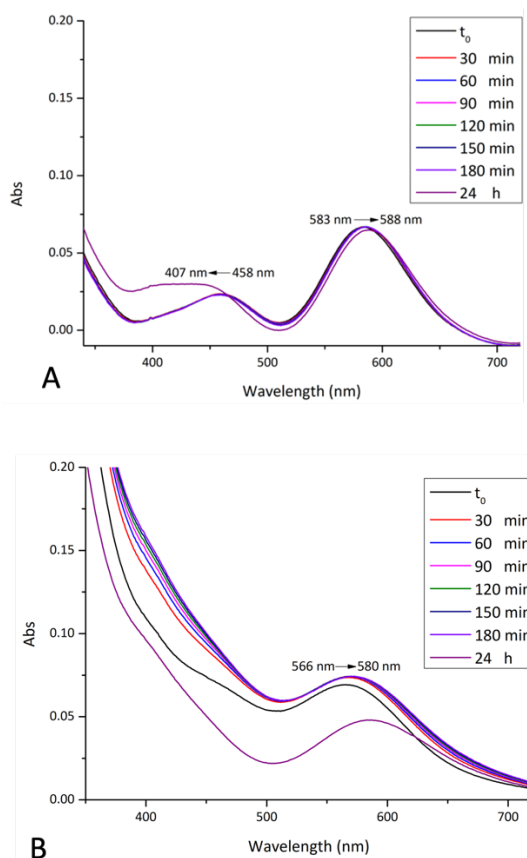


Figure 4.28. Time course UV-vis absorption spectra of  $[\text{Rh}_2(\text{OAc})(\text{tfa})_3]$  in 10.0 mM sodium citrate buffer pH 5.1 in the absence (panel A) and in the presence of RNase A (panel B). Metal/protein ratio 3:1.

When the metal compound is dissolved in 5.0 mM HEPES pH 7.5 the two bands of the dimetallic complex are observed at  $\lambda_{\text{max}} = 458 \text{ nm}$  and  $\lambda_{\text{max}} = 581 \text{ nm}$  (Figure 4.29 A). The first band disappears just after 30 min, suggesting a rapid release of tfa ligands also in HEPES buffer. This change is accompanied by a blue-shift of the second band from 581 nm up to 771 nm.

The band at  $\lambda_{\text{max}} = 548 \text{ nm}$  disappears just after the addition of HEWL. This finding suggests a complete release of tfa ions from the dimetallic centre. The band at 568 nm is red-shifted up to 575 nm, as observed in the spectra of *cis*-[Rh<sub>2</sub>(OAc)<sub>2</sub>(tfa)<sub>2</sub>] under the same experimental conditions (Figure 4.29 B).

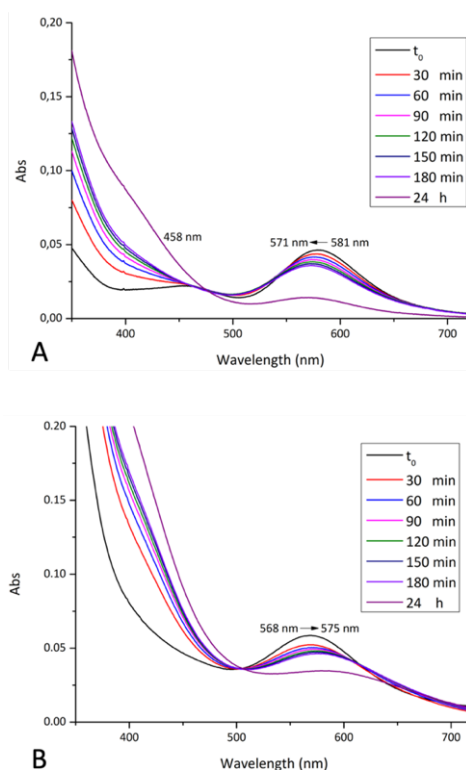


Figure 4.29. Time course UV-vis absorption spectra of [Rh<sub>2</sub>(OAc)(tfa)<sub>3</sub>] in 5.0 mM HEPES buffer pH 7.5 in the absence (panel A) and in the presence of HEWL (panel B). Metal/protein ratio 3:1.

$^{19}\text{F}$  NMR spectroscopy was used to further clarify the behaviour of the  $[\text{Rh}_2(\text{OAc})(\text{tfa})_3]$  in solution.  $^{19}\text{F}$  NMR spectra were recorded over time in the absence and in the presence of RNase A (Figure 4.30) and HEWL (Figure 4.31) in 10.0 mM sodium citrate pH 5.1 and 5.0 mM HEPES pH 7.5, respectively. Comparison between Figure 4.17 and Figure 4.30 reveals that  $[\text{Rh}_2(\text{OAc})(\text{tfa})_3]$  releases a higher percentage of tfa after 5 min when compared to *cis*- $[\text{Rh}_2(\text{OAc})_2(\text{tfa})_2]$  in sodium citrate at pH 5.1. Furthermore, in the spectrum of  $[\text{Rh}_2(\text{OAc})(\text{tfa})_3]$  several peaks were observed. They can be related to different hydrolysis products of the dimetallic compound when compared to those that can be formed starting from of *cis*- $[\text{Rh}_2(\text{OAc})_2(\text{tfa})_2]$ . tfa release from  $[\text{Rh}_2(\text{OAc})(\text{tfa})_3]$  is almost complete after 24 h, as observed for *cis*- $[\text{Rh}_2(\text{OAc})_2(\text{tfa})_2]$ . In the presence of RNase A, the tfa release is instantaneous, in fact it occurs just after the addition of the protein.

Several peaks are observed upon 24 h in the spectra recorded on the sample in HEPES buffer. This finding suggests that a mixture of species exists in solution under this condition. On the contrary, when the metal compound is in the presence of HEWL, tfa ligands are released after 2 h. Hence, in solution experiments revealed that  $[\text{Rh}_2(\text{OAc})(\text{tfa})_3]$  reacts with RNase A and HEWL, just like *cis*- $[\text{Rh}_2(\text{OAc})_2(\text{tfa})_2]$  and  $[\text{Rh}_2(\text{OAc})_4]$ .

The interaction occurs between hydrolysed species of the dimetallic centre and the proteins.

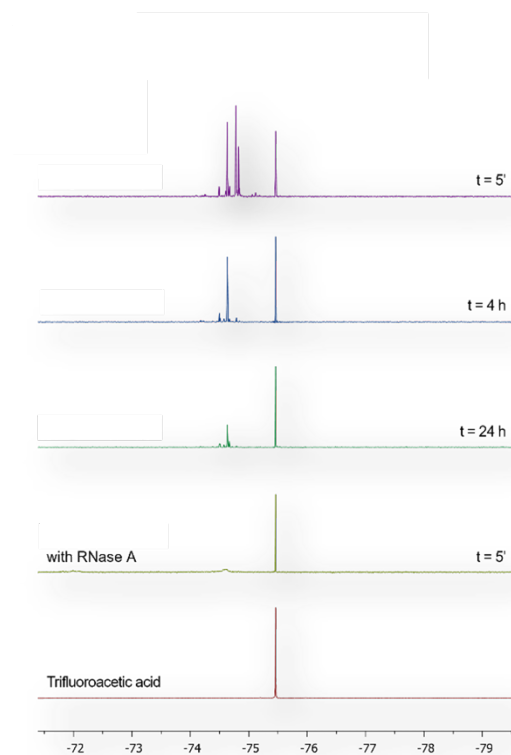


Figure 4.30.  $^{19}\text{F}$  NMR spectra of  $[\text{Rh}_2(\text{OAc})(\text{tfa})_3]$  in 10.0 mM sodium citrate pH 5.1 (10%  $\text{D}_2\text{O}$ ) recorded over time in the absence and presence of RNase A (metal/protein ratio 1:1).

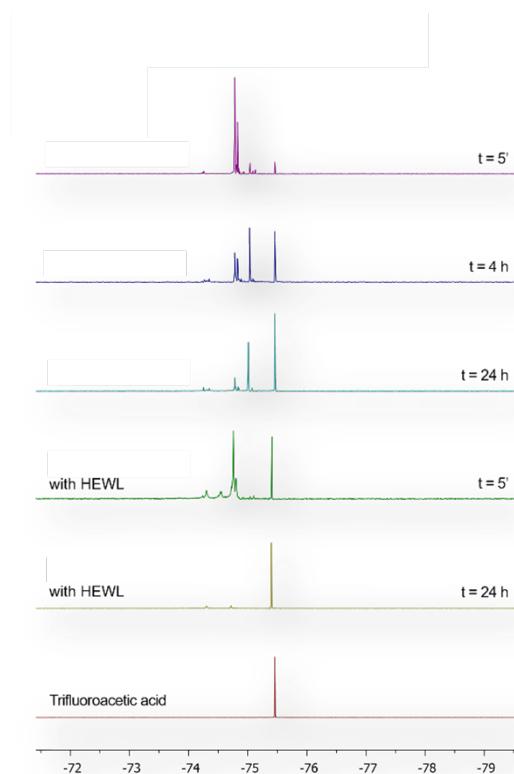


Figure 4.31.  $^{19}\text{F}$  NMR spectra of  $[\text{Rh}_2(\text{OAc})(\text{tfa})_3]$  in 5.0 mM HEPES pH 7.5 (10%  $\text{D}_2\text{O}$ ) recorded over time in the absence and presence of HEWL (metal/protein ratio 1:1).

To confirm that the proteins remain folded upon interaction with the dimetallic compound, the two macromolecules were incubated for 24 h with  $[\text{Rh}_2(\text{OAc})(\text{tfa})_3]$  in a 1:3 protein/metal ratio and CD data were recorded (Figure 4.32). The spectra of the two proteins in the absence and in the presence of the metal compound share a very similar shape, indicating that the binding of the metal compound does not affect the secondary structure, as observed when *cis*- $[\text{Rh}_2(\text{OAc})_2(\text{tfa})_2]$  and  $[\text{Rh}_2(\text{OAc})_4]$  interact with the same proteins.

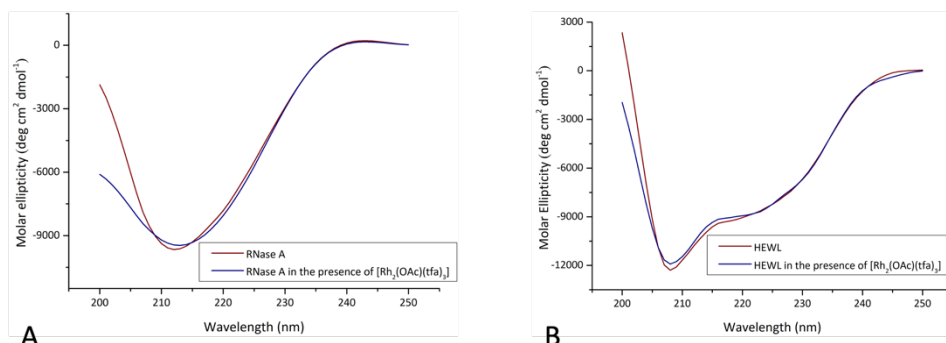


Figure 4.32. CD spectra of RNase A (panel A) and HEWL (panel B) in the absence and in the presence of  $[\text{Rh}_2(\text{OAc})(\text{tfa})_3]$ .

#### 4.16. X-ray structure of the $[\text{Rh}_2(\text{OAc})(\text{tfa})_3]/\text{RNase A}$ adduct

A deeper detail of the metal binding sites of the  $[\text{Rh}_2(\text{OAc})(\text{tfa})_3]/\text{RNase A}$  adduct was obtained using X-ray crystallography. Two structures of the metal/protein adduct were solved. The structures were refined at 1.45 and 1.71 Å resolution (Table C, Appendix) using crystals obtained via soaking strategy. This allows to directly compare the structural data on the  $[\text{Rh}_2(\text{OAc})(\text{tfa})_3]/\text{RNase A}$  adduct with those observed for the adducts formed upon reaction of RNase A with *cis*- $[\text{Rh}_2(\text{OAc})_2(\text{tfa})_2]$  and  $[\text{Rh}_2(\text{OAc})_4]$ . Also, the crystals used for these structural determinations belong to the C2 space group with two molecules in the asymmetric unit (molecule A and B). The two structures of the  $[\text{Rh}_2(\text{OAc})(\text{tfa})_3]/\text{RNase A}$  adduct are quite similar to each other. Metal binding sites were found close to the side chains of His105 of molecule A and to the side chain of His119 of molecule A and B (Figure 4.33).

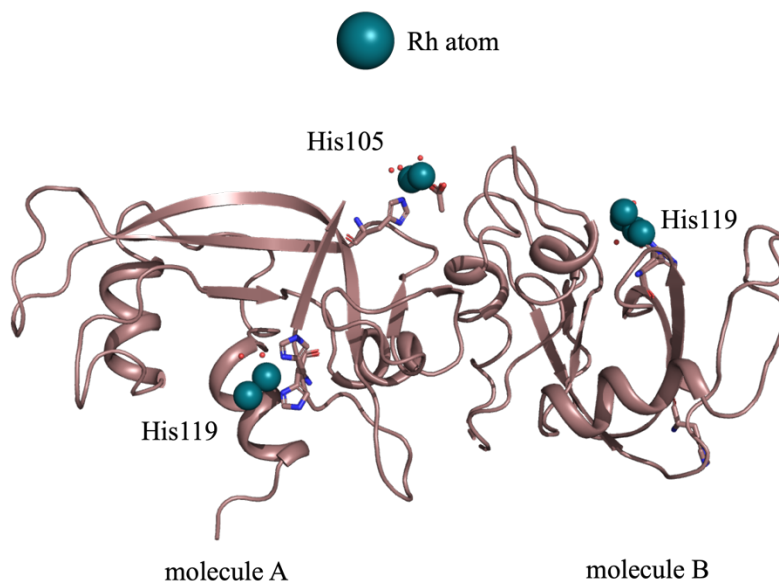


Figure 4.33. Overall structure of the  $[\text{Rh}_2(\text{OAc})(\text{tfa})_3]/\text{RNase A}$  adduct (from adduct 1, Table C, Appendix)

The crystal structure of the metal/protein adduct well overlaps with those of the adduct of RNase A with *cis*- $[\text{Rh}_2(\text{OAc})_2(\text{tfa})_2]$  and  $[\text{Rh}_2(\text{OAc})_4]$  as observed from  $\text{C}\alpha$  rmsd (0.099 to 0.448 Å). Despite the dirhodium core is well defined in all the binding sites, its ligands are not clearly defined in the electron density map. This finding is in agreement with  $^{19}\text{F}$  NMR data, indicating that the metal compound loses its tfa ions upon interaction with the protein.

His119 side chain of the molecule A adopts two alternate conformations, both coherent with the binding of imidazole ring to the dimetallic centre, at axial and equatorial positions (Figure 4.34). Rh-N distances at this binding site are 2.28 Å (axial binding) and 2.19 Å (equatorial binding). In the molecule B, His119 side chain is bound to a dirhodium fragment at axial position. Both His119 side chain and the dirhodium core occupy two different conformations (Figure 4.35). Since the two dirhodium units are close to each other, the interpretation of electron density map is not straightforward. However, the reproducibility of the experiments (two almost identical structures) allows to model this binding site

accurately. The Rh-Rh distances of the two alternate dirhodium fragments are 2.29 and 2.17 Å.

The possibility of equatorial binding of imidazole ring of His residues to the dirhodium core is further supported by the dimetallic fragment close to His105. Here, the dimetallic compound is equatorially coordinated to the imidazole ring of His105 residue (Figure 4.36). Furthermore, an acetate ligand coordinated only to one Rh atom is found at this binding site. The first coordination sphere of the dimetallic fragment is completed by water molecules. In the molecule B His105 is not metalated.

Dirhodium ligands are reported in Table 5 and bond distances and geometry are reported in Table 6.

In conclusion, the data here reported revealed that  $[\text{Rh}_2(\text{OAc})(\text{tfa})_3]$  binds proteins both at axial and equatorial positions, differently from *cis*- $[\text{Rh}_2(\text{OAc})_2(\text{tfa})_2]$  and  $[\text{Rh}_2(\text{OAc})_4]$ .

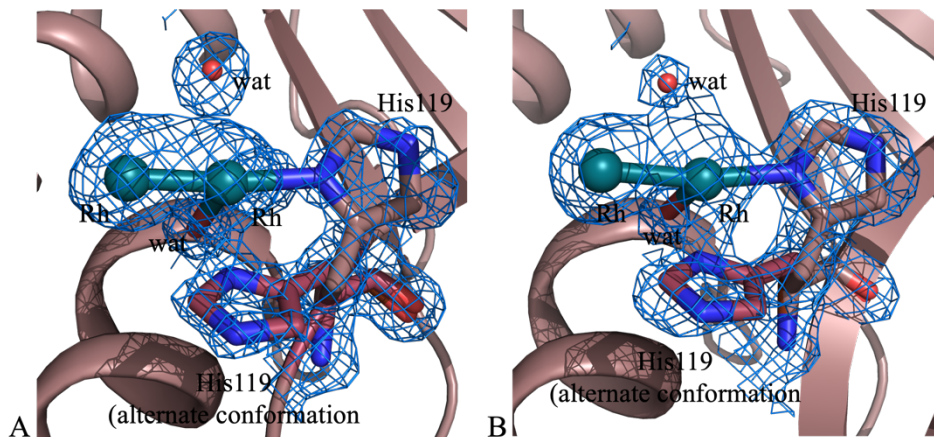


Figure 4.34. Details of Rh binding sites close to His119 side chain of the molecule A in the adducts 1 and 2 (panel A and B, respectively). 2Fo-Fc electron density maps are contoured at  $1.0\sigma$ .

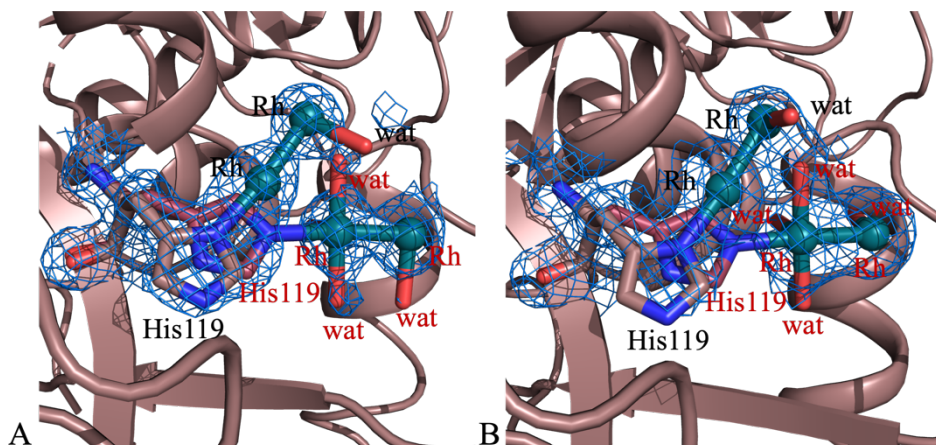


Figure 4.35. Details of Rh binding site close to His119 side chain of the molecule B in the adducts 1 and 2 (panel A and B, respectively). Alternate conformations of the metal compound are labelled in red. 2Fo-Fc electron density maps are contoured at  $1.0\sigma$ .

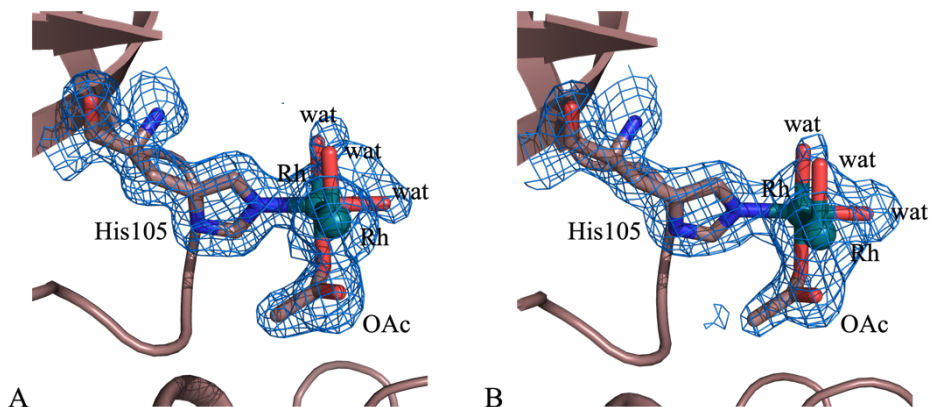


Figure 4.36. Details of Rh binding sites close to His105 side chain of the molecule A in the adducts 1 and 2 (panel A and B, respectively). 2Fo-Fc electron density maps are contoured at  $0.8\sigma$ .

Table 5. Rh-containing fragments and ligands bound in the three structures of Rh/protein adducts obtained upon reaction of  $[\text{Rh}_2(\text{OAc})(\text{tfa})_3]$  with RNase A and HEWL. Values in parenthesis indicate the occupancy of the metals and ligands.

Rh/RNase A adduct binding site	Metal and Ligands in adduct 1	Metal and Ligands in adduct 2
<b>His119 of molecule A</b> (His in double conformation in adducts 1 and 2)	Rh (0.40)	Rh (0.55)
	Rh (0.40)	Rh (0.55)
<b>His119 of molecule B</b> (His in double conformation in adducts 1 and 2)	Rh (0.20) (d.c.)	Rh (0.55) (d.c.)
	Rh (0.20) (d.c.)	Rh (0.55) (d.c.)
	Rh (0.40) (d.c.)	Rh (0.30) (d.c.)
	Rh (0.40) (d.c.)	Rh (0.30) (d.c.)
	H <sub>2</sub> O (0.20) (d.c.)	H <sub>2</sub> O (0.55) (d.c.)
	H <sub>2</sub> O (0.40) (d.c.)	H <sub>2</sub> O (0.55) (d.c.)
	H <sub>2</sub> O (0.40) (d.c.)	H <sub>2</sub> O (0.55) (d.c.)
<b>His105 of molecule A</b>	H <sub>2</sub> O (0.40) (d.c.)	H <sub>2</sub> O (0.55) (d.c.)
	H <sub>2</sub> O (0.40) (d.c.)	H <sub>2</sub> O (0.30) (d.c.)
	Rh (0.50)	Rh (0.70)
	Rh (0.50)	Rh (0.70)
	OAc (0.50)	OAc (0.70)
	H <sub>2</sub> O (0.50)	H <sub>2</sub> O (0.70)
<b>His105 of molecule B</b>	H <sub>2</sub> O (0.50)	H <sub>2</sub> O (0.70)
	H <sub>2</sub> O (0.50)	H <sub>2</sub> O (0.70)
	H <sub>2</sub> O (0.50)	H <sub>2</sub> O (0.70)
	H <sub>2</sub> O (0.50)	H <sub>2</sub> O (0.70)
<b>His105 of molecule B</b>	/	/
Rh/HEWL adduct binding site	Metal and Ligands in the structure	
<b>His15</b>	Rh (0.25)	
	Rh (0.25)	
<b>Lys33</b>	Rh (0.30)	
	H <sub>2</sub> O (0.30)	

<b>Asp101</b>	Rh (0.25)
	H <sub>2</sub> O (0.25)
<b>Leu129</b>	Rh (0.30)
	Rh*(0.30)

d.c. = double conformation

Table 6. Geometric parameters of the Rh-containing fragments in the [Rh<sub>2</sub>(OAc)(tfa)<sub>3</sub>]/RNase A adducts.

[Rh <sub>2</sub> (OAc)(tfa) <sub>3</sub> ]/RNase A adducts					
Adduct	His119A	His119B	His105A	His105B	
<b>1</b>	Rh—N <sub>ax</sub> <sup>a</sup> (Å)	2.28	2.23	/	
	Rh—N <sub>eq</sub> (Å)	2.19	/	2.03	
	Rh—Rh <sup>a</sup> (Å)	2.28	2.45	2.37	
	Rh—O <sub>OAc</sub> (Å)	/	/	2.10	
	Rh—O <sub>wat</sub> <sup>a</sup> (Å)	/	2.10	2.11	/
	O <sub>OAc</sub> —Rh—N (°)	/	/	94.3	
	N <sub>ax</sub> —Rh—Rh <sup>a</sup> (°)	174.3	172.5	/	
	N <sub>eq</sub> —Rh—Rh (°)	94.7	/	99.8	
	O <sub>wat</sub> —Rh—Rh <sup>a</sup> (°)	/	88.8	86.8	
	<b>2</b>	Rh—N <sub>ax</sub> <sup>a</sup> (Å)	2.31	2.16	/
Rh—N <sub>eq</sub> (Å)		2.01	/	2.15	
Rh—Rh <sup>a</sup> (Å)		2.53	2.47	2.29	
Rh—O <sub>OAc</sub> (Å)		/	/	2.13	/
Rh—O <sub>wat</sub> <sup>a</sup> (Å)		/	2.10	2.12	
O <sub>OAc</sub> —Rh—N (°)		/	/	89.6	

	$N_{\text{ax}}\text{—Rh—Rh}^a(^{\circ})$	170.7	171.4	/	
	$N_{\text{eq}}\text{—Rh—Rh} (^{\circ})$	92.5	/	100.4	
	$O_{\text{wat}}\text{—Rh—Rh}^a(^{\circ})$	/	90.6	83.9	
<b>Structure of the [Rh<sub>2</sub>(OAc)<sub>4</sub>]/RNase A adduct</b>	Rh—N (Å)	2.16	2.27	2.20	2.18
	Rh—Rh (Å)	2.34	2.37	2.42	2.42
	Rh—O <sub>OAc</sub> <sup>a</sup> (Å)	2.09	2.11	2.06	2.13
	Rh—O <sub>tfa</sub> <sup>a</sup> (Å)	/	/	/	/
	Rh—O <sub>wat</sub> <sup>a</sup> (Å)	2.24	2.28	2.29	2.28
	O <sub>OAc</sub> —Rh—N <sup>a</sup> ( <sup>°</sup> )	93.7	93.9	94.4	92.5
	O <sub>tfa</sub> —Rh—N <sup>a</sup> ( <sup>°</sup> )	90.9	91.9	91.1	93.3
	N—Rh—Rh ( <sup>°</sup> )	177.1	175.4	176.3	176.6
	O <sub>wat</sub> —Rh—Rh <sup>a</sup> ( <sup>°</sup> )	90.1	88.0	88.9	87.3

<sup>a</sup>Average values. Standard deviations for the distances are in the range of 0.01-0.08 Å. Standard deviations for the angles are in the range of 1.2-8.8 °. ‘wat’ refers only to water coordinating Rh atoms at equatorial positions.

#### 4.17. X-ray structure of the [Rh<sub>2</sub>(OAc)(tfa)<sub>3</sub>]/HEWL adduct

Both *cis*-[Rh<sub>2</sub>(OAc)<sub>2</sub>(tfa)<sub>2</sub>] and [Rh<sub>2</sub>(OAc)<sub>4</sub>] degrade upon interaction with HEWL in HEPES buffer, forming protein adducts containing both Rh and Rh<sub>2</sub> units. Similar results were observed for [Rh<sub>2</sub>(OAc)(tfa)<sub>3</sub>]. The crystal structure of [Rh<sub>2</sub>(OAc)(tfa)<sub>3</sub>] was refined at 1.53 Å resolution, (Figure 4.37). Rh binding sites were found close to the side chains of His15, Lys33, Asp101 and to the C-terminal tail (Figure 4.38).

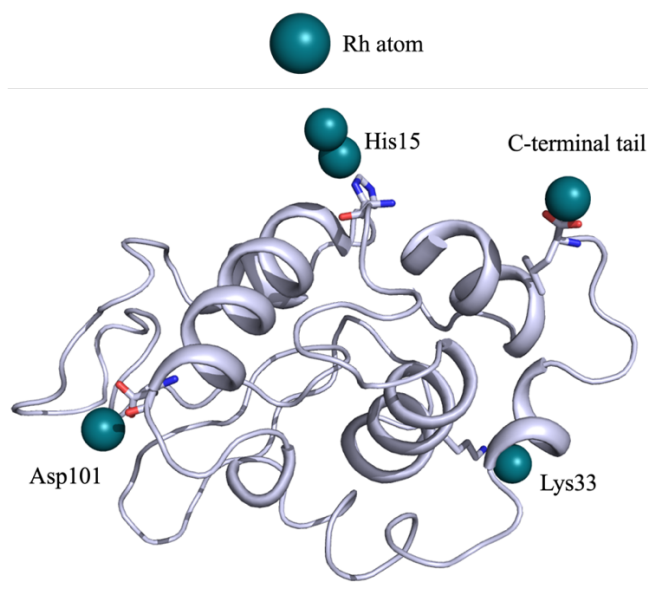


Figure 4.37. Overall structure of the  $[\text{Rh}_2(\text{OAc})(\text{tfa})_3]/\text{HEWL}$  adduct.

A dimetallic fragment with low occupancy (0.25, B-factor of Rh = 60.1-62.8 Å Figure 4.38 A) was found close to His15 side chain. Here, metal ligands were not observed in the difference Fourier electron density map and the anomalous difference electron density map peaks in correspondence to the Rh atoms are very low. Rh occupancy is low (0.25, Figure 4.38 B) also close to Lys33 side chain. A monometallic fragment was modelled at this site, coordinated to the  $\text{N}\zeta$  atom of Lys in an equatorial fashion.

A single Rh atom (occupancy = 0.30) was observed coordinated to  $\text{O}\delta 1$  atom of Asp101 side chain with a Rh-O distance of 2.22 Å (Figure 4.38 C).

Close to C-terminal tail, a singular binding site is observed where a dimetallic centre with a Rh-Rh distance of 3.2-3.4 Å is bound to the carboxylate and to Lys13 side chain at the interface between two symmetry-related molecules. These Rh atoms are surrounded by the O atom of the protein backbone and the  $\text{N}\zeta$  atom of Lys13. However, the long Rh-Rh, Rh-O and Rh-N distances (Rh-O = 2.38 and

(2.42 Å, Rh-N = 2.64 Å, Rh-Rh = 2.79 Å) suggest a significant degradation of the dirhodium complex.

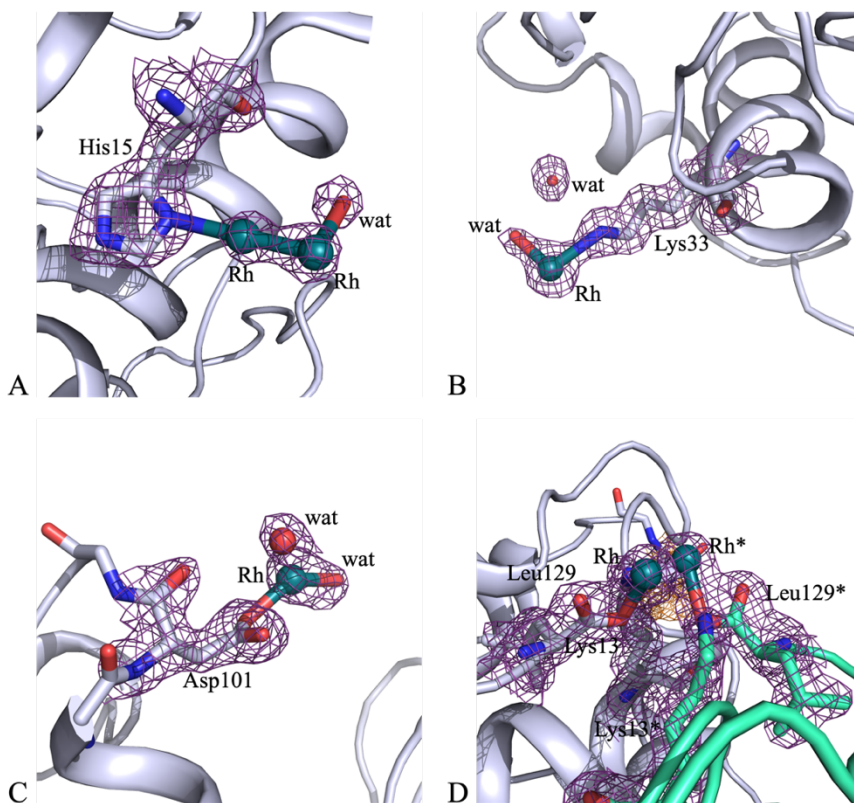


Figure 4.38. Details of Rh binding sites close to His15 (panel A), Lys33 (panel B), Asp101 (panel C) and C-terminal tail (panel D). 2Fo-Fc electron density maps are contoured at  $1.0\sigma$ . \* refers to symmetry related molecules.

#### 4.18. Summary of the interaction of $[\text{Rh}_2(\text{OAc})(\text{tfa})_3]$ with model proteins

Substitution of equatorial carboxylate ligands with tfa ions in the dirhodium paddlewheel compounds facilitates the reaction between these complexes and proteins. *cis*- $[\text{Rh}_2(\text{OAc})_2(\text{tfa})_2]$  reacts with proteins upon release of tfa ions. The metal is coordinated by His residues at axial position. The interaction of

$[\text{Rh}_2(\text{OAc})(\text{tfa})_3]$  with RNase A and HEWL was investigated, comparing the results with those obtained in the case of *cis*- $[\text{Rh}_2(\text{OAc})_2(\text{tfa})_2]$  and  $[\text{Rh}_2(\text{OAc})_4]$ .

In solution data reveal that  $[\text{Rh}_2(\text{OAc})(\text{tfa})_3]$  loses its fluorinated ligands instantaneously when it is in the presence of RNase A and after 2 h in the presence of HEWL. In contrast to what was found in the case of *cis*- $[\text{Rh}_2(\text{OAc})_2(\text{tfa})_2]$  and  $[\text{Rh}_2(\text{OAc})_4]$ , crystallographic data enlighten the capability of the proteins to bind the  $[\text{Rh}_2(\text{OAc})(\text{tfa})_3]$  compound both at axial and equatorial positions. The overall conformation of the two proteins is not altered upon binding of the metal complex.

N-containing ligands (e.g., isocyanide or pyridine) can bind  $\text{Rh}_2(\text{tfa})_4$  and a dimolybdenum compound bearing three tfa ions to both axial and equatorial positions, as observed in the structure of the  $[\text{Rh}_2(\text{OAc})(\text{tfa})_3]/\text{RNase A}$  adduct here reported.<sup>129,130</sup> It has been surmised that the equatorial binding to these complexes occurs only after initial coordination of the N donor ligand at axial position. 09/03/2023 16:42:00Hence,  $[\text{Rh}_2(\text{OAc})(\text{tfa})_3]$ , *cis*- $[\text{Rh}_2(\text{OAc})_2(\text{tfa})_2]$  and  $[\text{Rh}_2(\text{OAc})_4]$  form different reaction products upon reaction with proteins. This finding could explain the different results obtained studying the interaction of analogous dirhodium compounds and T7-RNA polymerase.<sup>38</sup>

These data also support the hypothesis that changing equatorial ligands in the dirhodium paddlewheel motif can be helpful in directing their effects on specific cellular targets. Furthermore, metalloenzymes with distinct properties can be prepared by using different dirhodium tetracarboxylates.

#### 4.19. *In crystallo* reactivity of [Rh<sub>2</sub>(OAc)<sub>4</sub>]/RNase A

When [Rh<sub>2</sub>(OAc)<sub>4</sub>] reacts with RNase A in the solid state, a metal/protein adduct is formed in which the overall paddlewheel structure of the dimetallic moiety is preserved.<sup>81</sup> Hence, to verify the dirhodium tetraacetate reactivity upon formation of the metal/protein adduct, the X-ray structure of the reaction product of the [Rh<sub>2</sub>(OAc)<sub>4</sub>]/RNase A adduct with imidazole (Im) was investigated in the solid state.

#### 4.20. X-ray structure of the [Rh<sub>2</sub>(OAc)<sub>4</sub>]/RNase A adduct upon reaction with imidazole in the solid state

Metal/protein adduct was prepared by soaking, as described above. Then, [Rh<sub>2</sub>(OAc)<sub>4</sub>]/RNase A adduct crystals were soaked with a solution of Im dissolved in the reservoir. The crystal structure of the reaction product was refined at 1.40 Å resolution. As in the previous described metal/protein adducts, the macromolecule crystallized in the C2 space group with two molecules in the asymmetric unit (Figure 4.39, Table D, Appendix). In both the molecules A and B the dirhodium core was observed close to His105 and His119 side chains (Figure 4.40). The structure is similar to the one of [Rh<sub>2</sub>(OAc)<sub>4</sub>]/RNase A adduct (C $\alpha$  rmsd = 0.22 and 0.15 for the molecules A and B, respectively).

Close to His119 side chains of the molecules A and B a dirhodium core surrounded by three acetate ligands and two water molecules was found. The Rh atom that is not bound to the protein is axially coordinated by a water molecule (Figure 4.40 A and B). Close to His105 side chains an Im molecule is found in both the molecules A and B. The presence of multiple conformations of the dimetallic compound close to His105 side chain in the molecule A prevented a clear interpretation of the electron density map at this binding site (Figure 4.40 C). Instead, in the molecule B this binding site is well defined in the electron density (Figure 4.40 D). Notably, at this dirhodium binding site, Im is not found coordinated to the axial position of the dirhodium core, as expected,<sup>76</sup> but it coordinates the dimetallic centre to a Rh atom that is already coordinated to the protein, i.e. at equatorial position. The Im binding at this position is stabilised by a H-bond network and contacts that are formed by the aromatic compound with the surrounding protein residues and water molecules (Figure 4.41). The

dirhodium coordination sphere is completed by an acetate ligand and five water molecules.

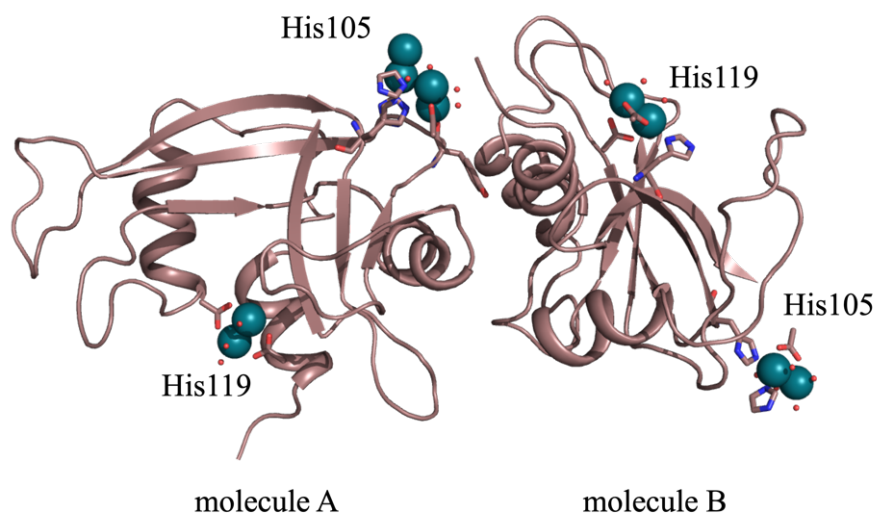


Figure 4.39. Overall structure of the  $[\text{Rh}_2(\text{OAc})_4]/\text{RNase A}$  adduct upon reaction with Im.

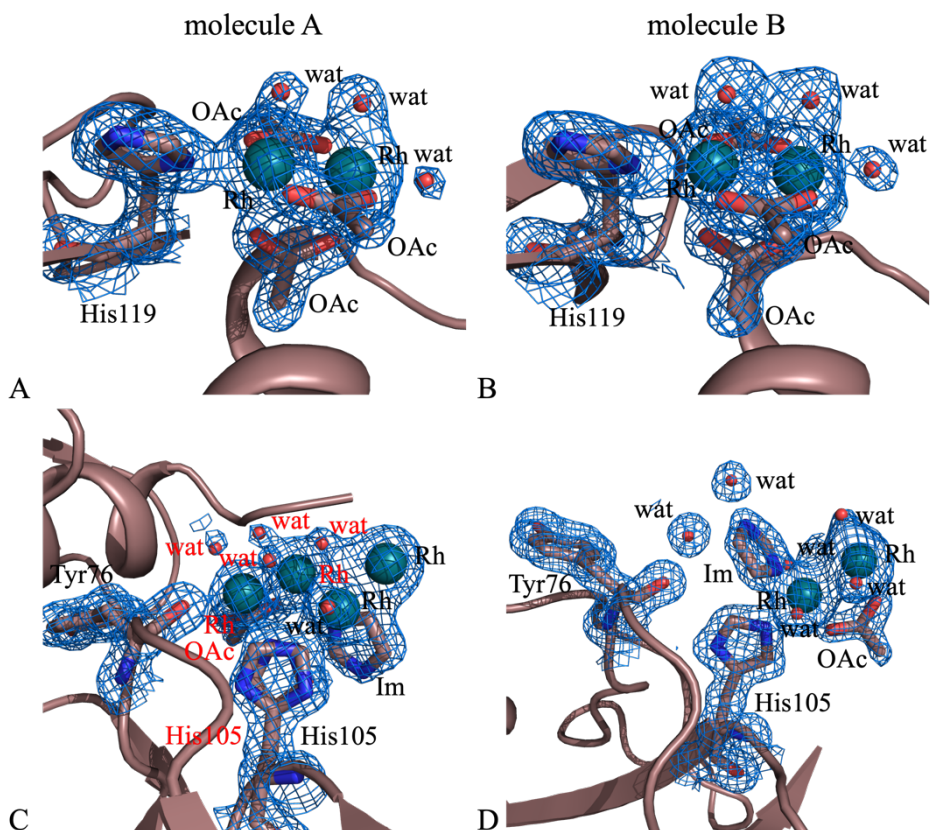


Figure 4.40. Details of Rh binding sites close to His119 of the molecule A (panel A), His119 of the molecule B (panel B), His105 of the molecule A (panel C) and His105 of the molecule B (panel D). 2Fo-Fc electron density maps are contoured at  $1.0\sigma$ .

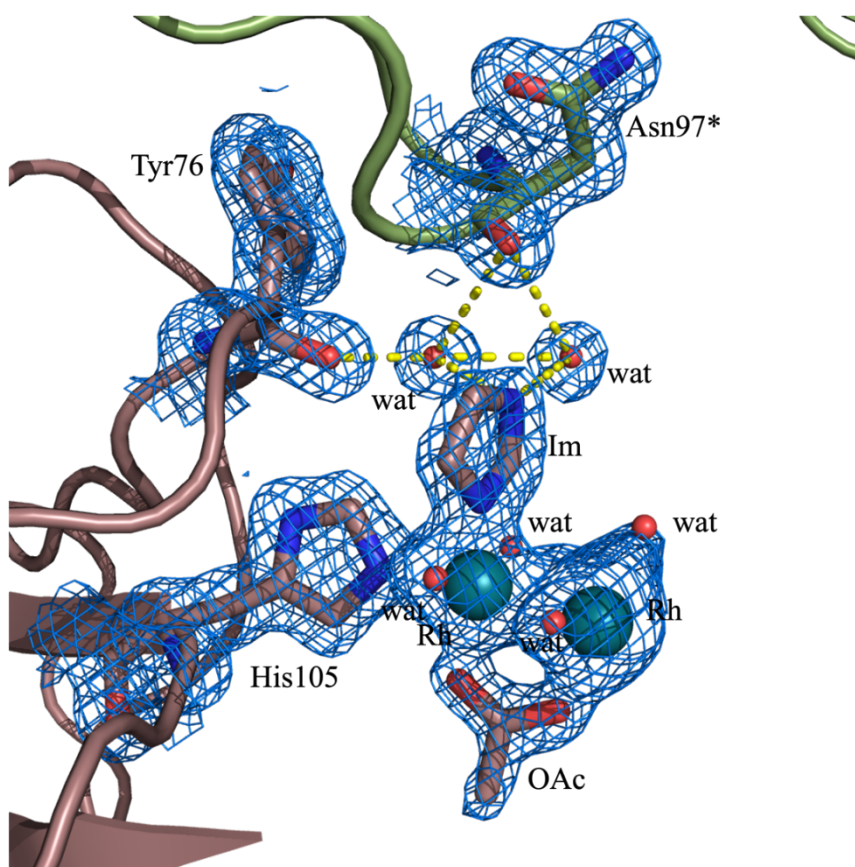


Figure 4.41. Deeper detail of the Rh binding site close to His105 in the molecule A. Polar contacts are shown in yellow. 2Fo-Fc electron density maps are contoured at  $1.0\sigma$ . \* refers to symmetry related molecules.

#### 4.21. Quantum chemical analysis of the reaction between $[\text{Rh}_2(\text{OAc})_4]/\text{RNase A}$ and imidazole

The rationale of the unexpected reactivity that arises from the interaction of  $[\text{Rh}_2(\text{OAc})_4]/\text{RNase A}$  adduct with Im in the solid state was investigated by quantum chemistry, within the frame of density functional theory (DFT). A small portion of the metal/protein adduct around His105 was carved from the crystal structure, following the cluster approach reviewed by Himo and co-workers

(Figure 4.42 A).<sup>131,132</sup> This model was built considering the distance of the surrounding residues from the dirhodium core. Furthermore, this model was compared with a minimal model in which the protein environment is neglected, and the dimetallic fragment was coordinated to one Im at one of the two available axial positions (Figure 4.42 B). In both cases, the polarizable continuum model was used to account for the dielectric properties of the chemical environment. Water was selected as solvent, since the metal compound is exposed to aqueous solution, and it was extensively hydrolysed in the metal/protein adduct.

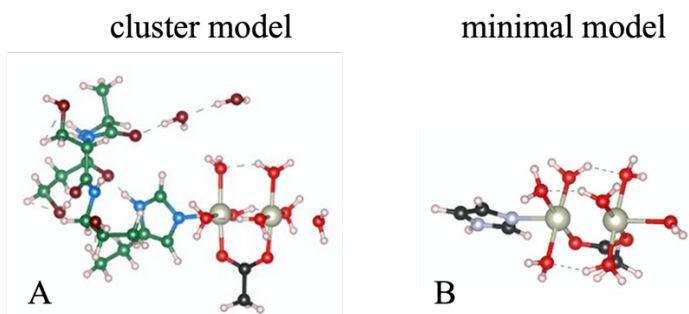


Figure 4.42. Depiction of the cluster (panel A) and minimal (panel B) models used for computational analysis.

The coordination of a second Im to the  $[\text{Rh}_2(\text{His}/\text{Im})(\text{OAc})(\text{H}_2\text{O})_7]^{3+}$  fragment was characterised for three available positions (Figure 4.43):

- Axial position to the Rh atom not bound to the protein (ax).
- Equatorial to the Rh atom not bound to the protein (r2).
- Equatorial to the Rh atom already bound to the protein (r1).

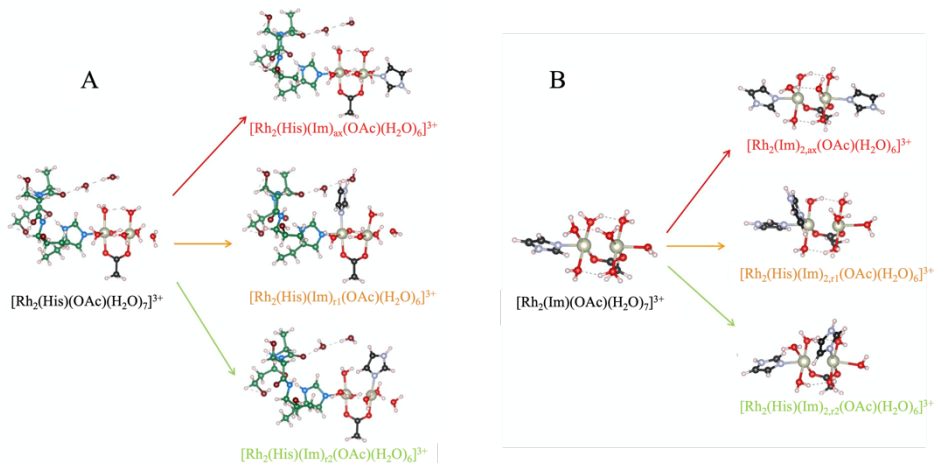


Figure 4.43. Three possible binding modes of imidazole to the dirhodium core for the cluster (panel A) and minimal (panel B) model. ax binding is represented in red, r1 binding is represented in yellow and r2 binding is represented in green.

The free energies for the above-mentioned substitutions were computed according to the following reaction scheme:



The free energy values reported in Table 7 highlighted a specific preference for equatorial coordination of Im to the Rh atom already bound to the protein (r1 binding). This binding preference is confirmed both in the cluster model and in the minimal model (Table 7). However, in the former model the r1 binding is further promoted by the presence of the surrounding protein residues.

Since the minimal model behaved like the cluster model, it was used to further investigate the Im binding to the dimetallic fragment.

In the metal/protein adduct three acetate ligands were replaced by six water molecules, thus, this hydrolysis of the dirhodium compound was investigated by quantum chemistry. It was found that the coordination of six water molecules to the dirhodium compound does not balance the cost of removing three acetate

ligands from the dimetallic centre. In fact, the free energy variation upon going from  $[\text{Rh}_2(\text{Im})(\text{OAc})_4(\text{H}_2\text{O})]$  to  $[\text{Rh}_2(\text{Im})(\text{OAc})(\text{H}_2\text{O})_7]^{3+}$  is unfavourable ( $\sim 5$  eV, Figure 4.44). The model considered that acetate groups entered into the solvent as isolated moieties. Hence, the protein environment balanced the thermodynamics for this process, stabilizing the leaving acetate groups, and concurrently providing extra stabilization through the second-shell H-bond network. Once the  $[\text{Rh}_2(\text{Im})(\text{OAc})(\text{H}_2\text{O})_7]^{3+}$  species is formed, the second Im molecule binds the dimetallic fragment at r1 position spontaneously.

Table 7. Free energy variations ( $\Delta G$ ) values associated to the substitution of a water molecule upon binding of Im at different coordination sites.  $\Delta G_{\text{rel}}$  refers to free energy variations relative to the r binding.

		ax	r2	r
$\Delta G$ (eV)	cluster model	-0.398	-1.004	-1.173
	minimal model	-0.482	-0.940	-1.003
$\Delta G_{\text{rel}}$ (eV)	cluster model	0.776	0.169	0.0
	minimal model	0.544	0.081	0.0

The electronic features of the  $[\text{Rh}_2(\text{Im})(\text{OAc})(\text{H}_2\text{O})_7]^{3+}$  species account for such unexpected Im binding. In fact, once that a Rh atom is bound to an Im (or His) molecule, the two Rh atoms in the dimetallic compound become not equivalent (Figure 4.45). Bader's Atom-in-Molecule charge analysis of  $[\text{Rh}_2(\text{Im})(\text{OAc})(\text{H}_2\text{O})_7]^{3+}$  compound revealed that the Rh atom coordinated to the protein is slightly more positive than the other Rh atom, thus, its Lewis acidity is enhanced for hosting a second Im molecule (Figure 4.45).

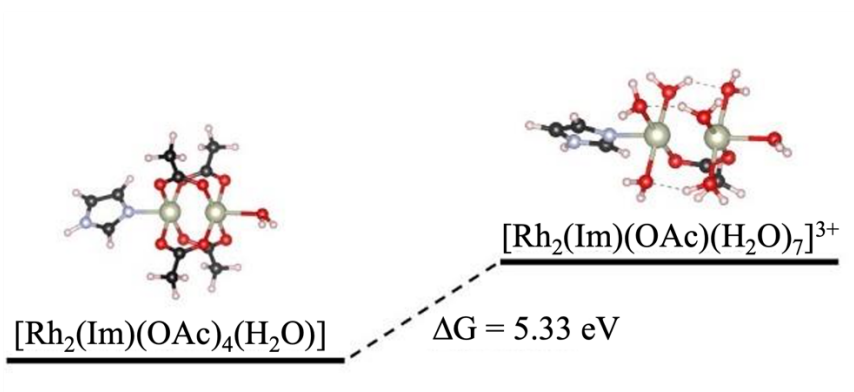


Figure 4.44. Free energy variations of the  $[\text{Rh}_2(\text{Im})(\text{OAc})(\text{H}_2\text{O})_7]^{3+}$  upon hydrolysis of acetate ligands.

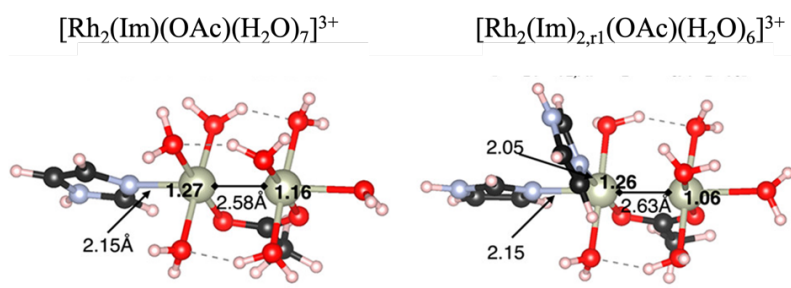


Figure 4.45. Computed Bader charges on Rh atoms for  $[\text{Rh}_2(\text{Im})(\text{OAc})(\text{H}_2\text{O})_7]^{3+}$  and  $[\text{Rh}_2(\text{Im})_{2,r1}(\text{H}_2\text{O})_6]^{3+}$ .

The degree of hydrolysis also plays a significant role in the observed and computed selectivity. In fact, the substitution free energy for a water molecule by Im on r1, r2 and ax binding for the  $[\text{Rh}_2(\text{Im})(\text{OAc})_4(\text{H}_2\text{O})]$ ,  $[\text{Rh}_2(\text{Im})(\text{OAc})_3(\text{H}_2\text{O})_3]^+$ , and  $[\text{Rh}_2(\text{Im})(\text{OAc})_2(\text{H}_2\text{O})_5]^{2+}$  series (i.e., for the adducts with four three and two acetate ligands) revealed that these species host the second Im molecule at r2 position (Figure 4.46). Hence, despite the ax binding is by far the least favourable process for all hydrolysis degrees, the r2 binding is favoured for the dimetallic adducts bearing three or two acetate ligands, and the

r1 binding becomes the most favoured process only for the adduct with one acetate group, as found in the experimental data. The presence of a second-shell H-bond network provided by protein residues could alter these relative energies. However, when dirhodium compounds react with proteins, they can be hydrolysed,<sup>81</sup> hence, when Im is added to a dirhodium/protein adduct, the r2 binding could be observed.

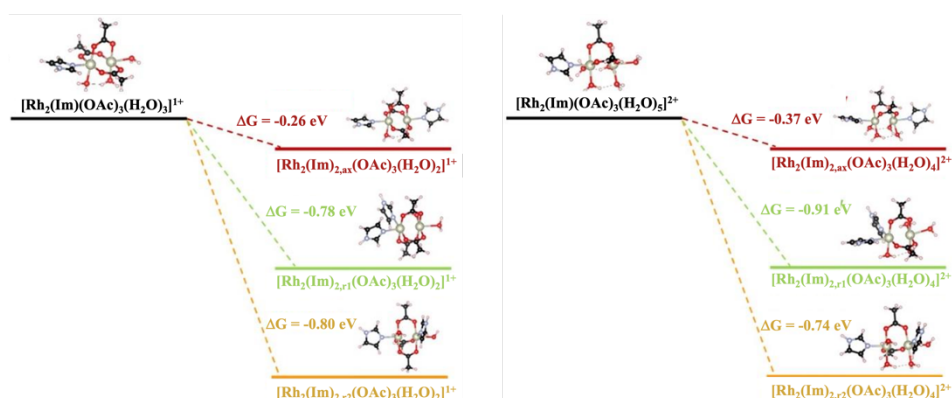


Figure 4.46. All the possible Im binding modes to the  $[\text{Rh}_2(\text{Im})(\text{OAc})_3(\text{H}_2\text{O})_3]^+$  (on the left) and  $[\text{Rh}_2(\text{Im})(\text{OAc})_2(\text{H}_2\text{O})_5]^{2+}$  (on the right) compounds. Free energy variation associated to the Im binding modes is also reported.

The peculiar electronic features of the dirhodium/protein adduct here described can result in modified (photo)catalytic activity, as observed by the qualitative differences between the computed frontier orbitals of  $[\text{Rh}_2(\text{Im})_{2,r1}(\text{OAc})(\text{H}_2\text{O})_6]^{3+}$  and  $[\text{Rh}_2(\text{Im})(\text{OAc})(\text{H}_2\text{O})_7]^{3+}$  species (Figure 4.47). For instance, the  $[\text{Rh}_2(\text{Im})(\text{OAc})(\text{H}_2\text{O})_7]^{3+}$  compound loses the involvement of the Im  $\pi$  system in its highest occupied molecular orbital (HOMO) when the  $[\text{Rh}_2(\text{Im})_{2,r1}(\text{OAc})(\text{H}_2\text{O})_6]^{3+}$  is formed, and the lowest unoccupied molecular orbital (LUMO) presents a more significant contribution from the Rh that is not bound to the two Im ligands (Figure 4.47).

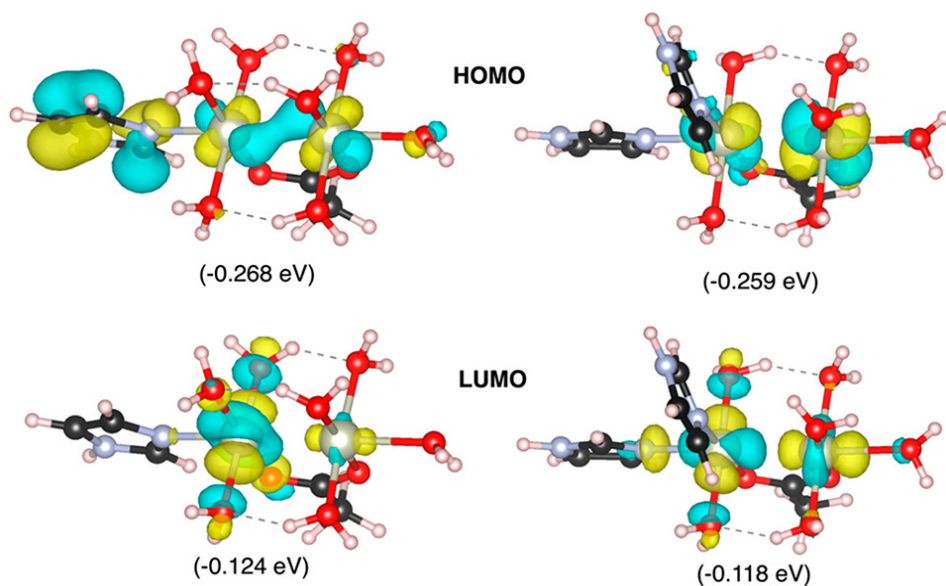


Figure 4.47. HOMO and LUMO of  $[\text{Rh}_2(\text{Im})(\text{OAc})(\text{H}_2\text{O})_7]^{3+}$  (on the left) and  $[\text{Rh}_2(\text{Im})_{2,\text{r1}}(\text{OAc})(\text{H}_2\text{O})_6]^{3+}$  (on the right) with their corresponding energies. Isodensity surfaces are depicted in cyan (positive values) and yellow (negative values).

#### 4.22. Summary of the *in crystallo* reactivity of $[\text{Rh}_2(\text{OAc})_4]/\text{RNase A}$

The product of the reaction between the  $[\text{Rh}_2(\text{OAc})_4]/\text{RNase A}$  adduct and Im was investigated in the solid state by X-ray crystallography. The metal/protein adduct reacts with Im and reaction product consists of Im bound to the dirhodium core at equatorial rather than axial position. DFT analysis indicates that the experimentally observed reaction product is the most stable reaction product once the original dirhodium compound is hydrolysed upon formation of the adduct with the protein. The unexpected equatorial binding of Im to the dirhodium core was explained by electronic structure analysis, which enlightened also interesting features of frontier molecular orbitals.

It is worth to note that when  $[\text{Rh}_2(\text{OAc})(\text{tfa})_3]$  interacts with RNase A, the three tfa ligands are lost in the metal/protein adduct, forming an adduct quite similar to that observed in the  $[\text{Rh}_2(\text{OAc})_4]/\text{RNase A}$  adduct upon reaction with imidazole.

Hence, DFT analysis could also be helpful in explaining the equatorial binding of His side chains observed upon reaction of  $[\text{Rh}_2(\text{OAc})(\text{tfa})_3]$  with RNase A.

These results open new directions in the exploitation of the reactivity of metal/protein crystal adducts as heterogeneous catalysts.

#### 4.23. Interaction of $[\text{Rh}_2(\text{OAc})_4]$ /RNase A with glycine

The structure of the reaction product of Im with the  $[\text{Rh}_2(\text{OAc})_4]$ /RNase A adduct in the solid state revealed that a dirhodium centre that is coordinated to a protein side chain reacts differently from an isolated dirhodium centre. To further explore the reactivity of  $[\text{Rh}_2(\text{OAc})_4]$ /RNase A adduct in the solid state, the reaction product derived from the reaction of this adduct with glycine was characterized by X-ray crystallography.

$[\text{Rh}_2(\text{OAc})_4]$ /RNase A adduct was prepared via soaking, as described above. Metal/protein adduct crystals were soaked with a glycine solution prepared dissolving glycine in the crystallization condition. The crystal structure was solved at 1.42 Å. As expected, crystals belong to the C2 space group with two molecules in the asymmetric unit (Figure 4.48, Table E, Appendix).

#### 4.24. X-ray structure of the $[\text{Rh}_2(\text{OAc})_4]$ /RNase A adduct upon reaction with glycine in the solid state

Superimposition of the structure of the  $[\text{Rh}_2(\text{OAc})_4]$ /RNase A adduct before and after soaking with glycine revealed that the binding of the amino acid does not alter the overall conformation of the protein ( $C\alpha$  rmsd= 0.162 for the molecule A and 0.150 for the molecule B).

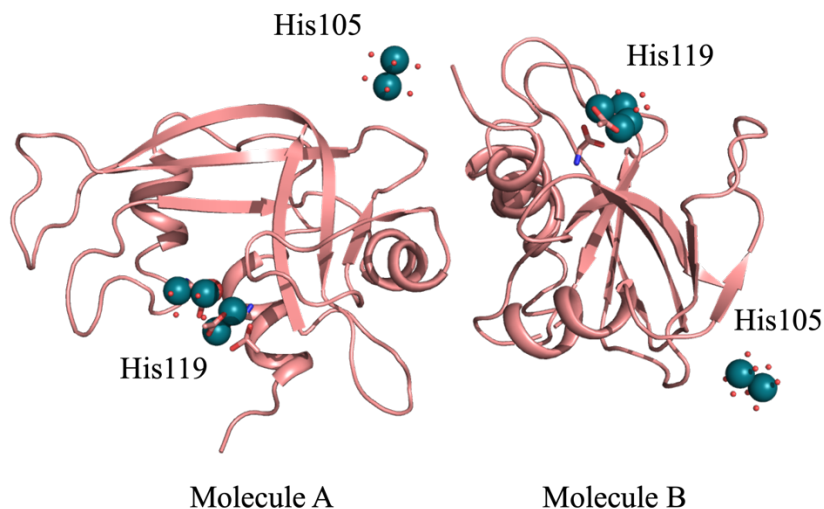


Figure 4.48. Overall structure of the  $[\text{Rh}_2(\text{OAc})_4]/\text{RNase A}$  adduct upon reaction with glycine.

Rh atoms are found close to side chains of His105 and His119 residues in both molecule A and B (Figure 4.49). In both molecules, close to His105 the metal compound is extensively hydrolysed, all the acetate ligands are replaced by water molecules. The Rh-Rh distance ranges from 2.41 to 2.46 Å (Figure 4.49 A and B). Glycine was found as an equatorial ligand of the dirhodium compound close to His119 side chains of the molecule A and B (Figure 4.49 C and D). In molecule A, two glycine molecules were found coordinated to the dirhodium core (Rh-Rh distance 2.41 Å) at equatorial position, in *cis* conformation. Two acetate ligands completed the dirhodium paddlewheel motif. Furthermore, an additional dirhodium fragment with low occupancy (0.30) was found as alternative conformation. In molecule B, a dirhodium core is equatorially coordinated by two glycine molecules in *cis* conformation to each other and to an acetate ligand and two water molecules. Again, a dimetallic fragment with low occupancy (0.30) is found at this binding site. The low occupancy of the alternative conformation of the dimetallic core prevents a detailed description of the Rh ligand in both cases.

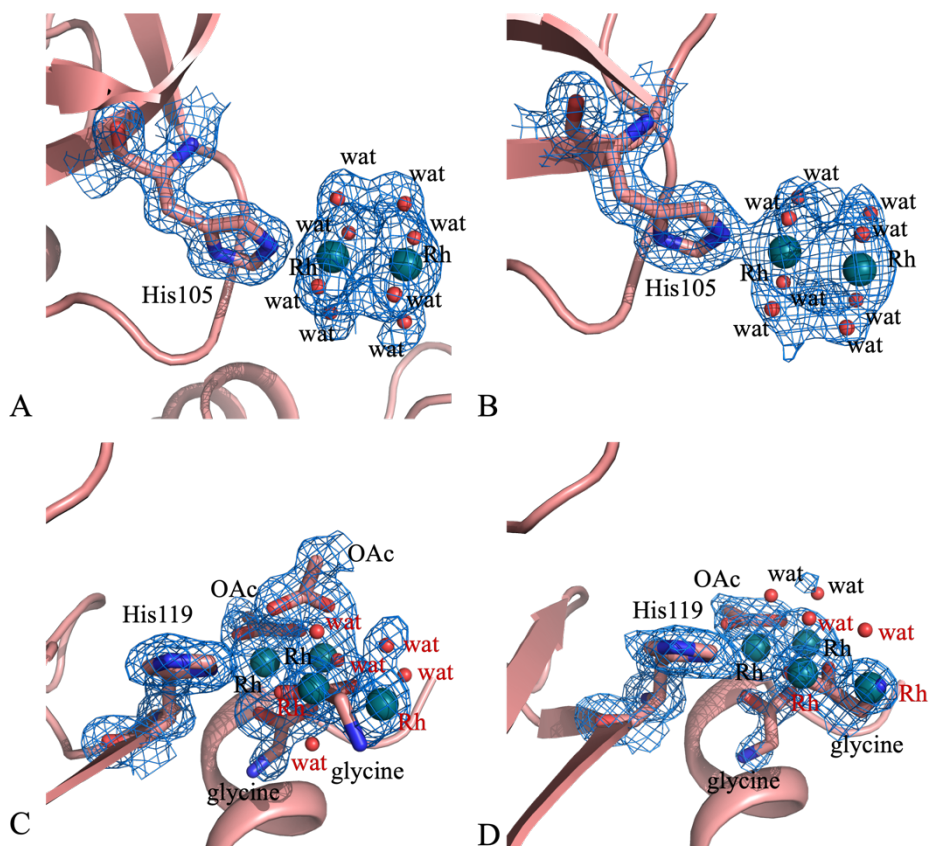


Figure 4.49. Details of Rh binding sites in the molecule A (left side, panel A and C) and in the molecule B (right side, panel B and D). His105 binding sites are shown in panel A and B. His119 binding sites are shown in panels C and D. 2Fo-Fc electron density maps are contoured at  $1.0\sigma$ . Atoms in alternative conformations are indicated in red.

#### 4.25. Summary of the interaction between $[\text{Rh}_2(\text{OAc})_4]/\text{RNase A}$ and glycine

The reactivity of  $[\text{Rh}_2(\text{OAc})_4]/\text{RNase A}$  adduct towards small organic ligands differs from that of the metal compound alone. In fact, when  $[\text{Rh}_2(\text{OAc})_4]$  reacts with imidazole, an adduct is formed in which two Im rings are bound to the dirhodium core at axial positions.<sup>76</sup> When the metal is in adduct with RNase A,

the binding of a second imidazole occurs at equatorial position. Similar results were observed with glycine. In fact, the amino acid binds the dirhodium core at equatorial position. The equatorial ligation could occur following the traditional mechanism of ligand substitution of dirhodium complexes, where the ligand binds the dimetallic centre at axial position and then it transposes to equatorial position releasing an acetate moiety.<sup>8</sup>

This result represents a new synthetic strategy for the formation of metal/protein adducts. In fact, while the adducts of RNase A with *cis*-[Rh<sub>2</sub>(OAc)<sub>2</sub>(tfa)<sub>2</sub>] and [Rh<sub>2</sub>(OAc)(tfa)<sub>3</sub>] have been obtained by reaction of the already fluorinated metal compounds with the protein, in this case the metal/protein adduct was formed by reaction of protein crystals with [Rh<sub>2</sub>(OAc)<sub>4</sub>]; then, the equatorial ligands were modified. These results open the way to new synthetic approaches for the preparation of the metal/protein adducts, which avoid all the purification steps required for synthesis of dimetallic complexes in solution. In fact, once the metal/protein adduct is modified in the solid state, it can be simply dissolved to provide a metal/protein adduct in solution which can be used without further purification steps.

#### **4.26. Development of cross-linked RNase A crystals functionalised with [Rh<sub>2</sub>(OAc)<sub>4</sub>] as biohybrid materials for heterogeneous catalysis**

The structural characterization of the adducts formed upon reaction of HEWL with dirhodium compounds above described suggests that HEWL crystals are not useful for the preparation of CLPCs functionalised with dirhodium compounds, since in the adducts with HEWL dirhodium centres can degrade. On the other hand, in RNase A crystals described in the previous paragraphs (space group C2, with two protein molecules in the asymmetric unit) dirhodium centres are stable, but these crystals do not seem to be useful to prepare CLPCs, since they grow in two weeks and need long soaking time for the formation of the adducts (one week more).<sup>81</sup>

With this in mind, RNase A crystals obtained in other experimental conditions and belonging to another space group were prepared. Crystals of RNase A belonging to the P3<sub>2</sub>21 space group can be used to form adducts with [Rh<sub>2</sub>(OAc)<sub>4</sub>]

and to prepare CLPCs. The protocol for preparing good quality cross-linked (CL) protein crystals of the  $[\text{Rh}_2(\text{OAc})_4]/\text{RNase A}$  adduct was thus developed. The crystal structure of the metal/protein adduct was solved both at  $-173\text{ }^\circ\text{C}$  and  $0\text{ }^\circ\text{C}$  and the metal accumulation mechanism over time was investigated by X-ray crystallography. The catalytic activity of the CL\_**Rh**/RNase A crystals towards olefine cyclopropanation and self-coupling of diazo compounds was assayed through gas chromatography-mass spectrometry (GC-MS). Catalytic performances of the CL\_**Rh**/RNase A crystals towards olefine cyclopropanation were compared with those of  $[\text{Rh}_2(\text{OAc})_4]$  using  $^1\text{H}$  NMR, ICP-OES (Inductively coupled plasma-optical emission spectroscopy) and GC-MS techniques.

#### 4.27. Selection of suitable experimental conditions for the growth of CL\_RNase A crystals

Crystals under two different crystallization conditions of RNase A in the  $\text{P3}_221$  space group were grown using the hanging drop vapor diffusion technique:

- 50% NaCl, 30%  $(\text{NH}_4)_2\text{SO}_4$  and 0.1 M sodium acetate buffer pH 4.8-5.5.
- 2.5 M NaCl, 3.3 M sodium formate, 0.1 M sodium acetate buffer pH 4.7-5.5.

Under these conditions, RNase A crystals in the  $\text{P3}_221$  space group grow in one day.<sup>133</sup> An analysis of crystal solvent channels revealed that these crystals have larger pores than RNase A crystals belonging to the  $\text{C2}$  space group (Figure 4.50). This could be an advantage since the large pores of  $\text{P3}_221$  crystals can help to host not only  $[\text{Rh}_2(\text{OAc})_4]$  but also different substrate molecules within the protein crystals, thus allowing catalysis experiments.

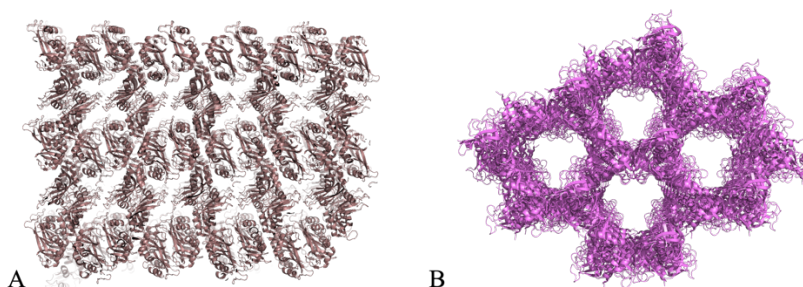


Figure 4.50. RNase A crystals into C2 (panel A) and P3<sub>2</sub>21 (panel B) space groups (PDB codes: 1JVT and 5OGH, respectively).

To prepare CL\_RNase A crystals, GA was used as cross-linking agent. GA percentage and cross-linking time were screened to prepare CLPCs with good mechanical properties. When treated with GA, RNase A crystals that were grown in 50% NaCl, 30% (NH<sub>4</sub>)<sub>2</sub>SO<sub>4</sub> and 0.1 M sodium acetate turn into orange and crack in less than 10 min, even at low GA concentrations (0.5%) (Figure 4.51). CLPCs obtained in this condition do not diffract X-rays and dissolve when they are far from their mother liquor.



Figure 4.51. RNase A crystals grown in 50% NaCl, 30% (NH<sub>4</sub>)<sub>2</sub>SO<sub>4</sub> and 0.1 M sodium acetate upon GA treatment.

Hence, the cross-linking protocol was optimised for crystals grown in 2.5 M NaCl, 3.3 M sodium formate and 0.1 M sodium acetate. The gentle diffusion technique was applied.<sup>98</sup> The best results were obtained when 0.5% GA was added only to

the reservoir and crystals were exposed for less than 2 h to GA vapours. Few cracks are observed on the lattice surface under these conditions, but crystals display good mechanical properties when they are far from their mother liquor and still diffract X-ray (Figure 4.52). When the crystals are exposed to GA more than 2 h, they lose their diffraction power.

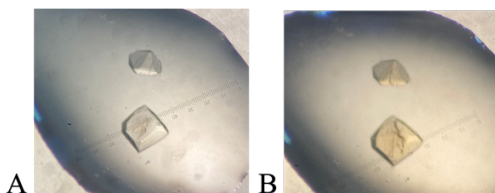


Figure 4.52. RNase A crystals grown in 2.5 M NaCl, 3.3 M sodium formate and 0.1 M sodium acetate before (panel A) and after (panel B) GA treatment using gentle diffusion technique.

#### 4.28. $[\text{Rh}_2(\text{OAc})_4]$ accumulation within RNase A crystals into the $\text{P3}_221$ space group

Once the cross-linking protocol was optimized, it was verified if RNase A crystals in the space group  $\text{P3}_221$ , that possess a single protein molecule in the asymmetric unit, could be used to form adducts with  $[\text{Rh}_2(\text{OAc})_4]$ .

RNase A crystals grown in 2.5 M NaCl, 3.3 M sodium formate and 0.1 M sodium acetate buffer pH 4.8 were used to prepare the metal/protein adduct by soaking techniques. Crystals were exposed to a solution consisting of  $[\text{Rh}_2(\text{OAc})_4]$  dissolved in the crystallization buffer. After 1 h, they turn into light pink. Protein crystals exposed to  $[\text{Rh}_2(\text{OAc})_4]$  after different soaking times (1 h, 2 h and 6 h) were used to collect X-ray diffraction data in order to characterise the binding process of the metal compound to the protein. Thus, three different structures of the  $[\text{Rh}_2(\text{OAc})_4]$ /RNase A adduct into the  $\text{P3}_221$  space group were solved. Data collection and refinement statistics can be found in Table F (Appendix). All the structures were quite similar to each other and to the metal-free RNase A (Table 8, PDB code: 5OGH).<sup>134</sup> Thus, the metal binding does not alter the overall protein

conformation (Figure 4.53), as found in the case of the dirhodium/RNase A adducts obtained in the C2 space group.<sup>81</sup>

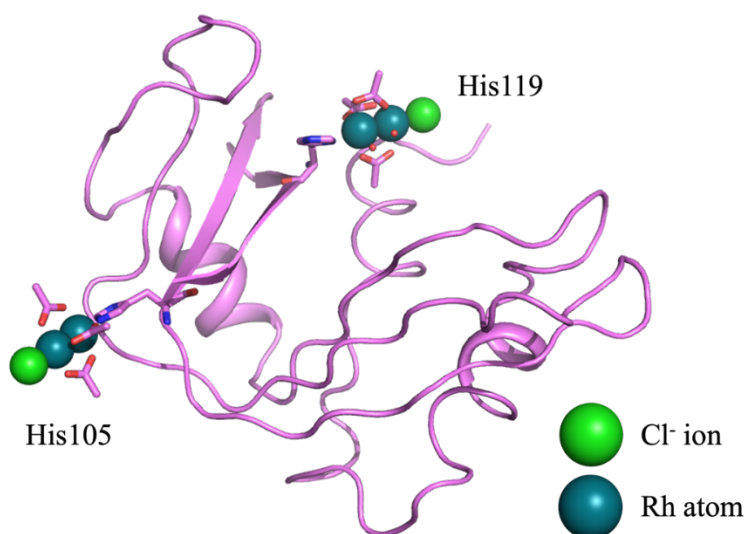


Figure 4.53. Overall structure of the  $[\text{Rh}_2(\text{OAc})_4]/\text{RNase A}$  adduct in the P3<sub>2</sub>21 space group obtained upon exposure of RNase A crystals to  $[\text{Rh}_2(\text{OAc})_4]$  for 2 h, Table 9 and Table F, Appendix).

The structures share common binding sites for the dirhodium tetraacetate. The first binding site was observed close to His105 side chain (occupancy: 0.70-0.80, Figure 4.54) in all the structures. A second binding site was observed close to His119 side chain (Figure 4.55), but with lower occupancy (0.50-0.55). It is worth to note that the binding of the dirhodium compound always occurs close to His105 and His119 side chains, regardless the crystal packing. Details of dimetallic fragments and ligands found in the metal/protein adduct structures are reported in Table 9. The high similarity of the three structures demonstrates that the protein is highly metalated just after 2 h of exposure to the dimetallic complex and no significant variation in protein metalation occurs over time.

His105 binding site contains a  $[\text{Rh}_2(\text{OAc})_4]$  unit that is coordinated to the imidazole ring of His105 ring and a  $\text{Cl}^-$  ion at axial position. The presence of  $\text{Cl}^-$  ion coordinated to the dirhodium core could be explained considering the high concentration of  $\text{NaCl}$  in the crystallization conditions used to grow the metal/protein adduct crystals (Figure 4.54)

Close to His119 side chain a dimetallic fragment coordinated by three acetate ions and two water molecules at equatorial position is observed (Figure 4.55). The dimetallic fragment is axially coordinated to the  $\text{N}\delta$  atom of His119 side chain; a  $\text{Cl}^-$  ion occupies the other at axial position. In the crystal exposed to the metal compound for 1 h (Table 9 and Table F, Appendix) a double conformation of His119 side chain is observed (Figure 4.55 A).

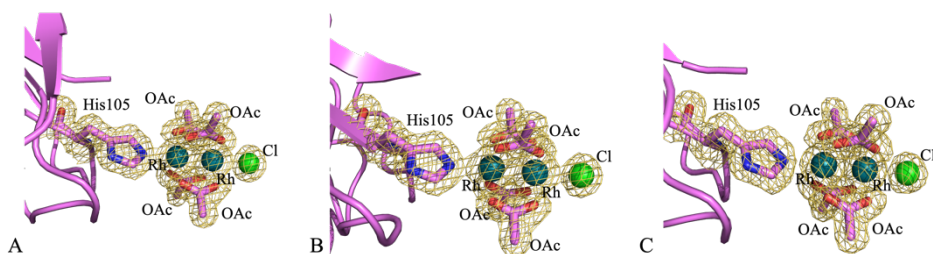


Figure 4.54. Details of His105 binding sites in the crystal structures of the  $[\text{Rh}_2(\text{OAc})_4]/\text{RNase A}$  adduct obtained upon 1 h (panel A), 2 h (panel B) and 6 h (panel C) of soaking of RNase A crystals with  $[\text{Rh}_2(\text{OAc})_4]$ . 2Fo-Fc electron density maps are contoured at  $1.0\sigma$ .

These results indicate that under these crystallization and soaking conditions the  $[\text{Rh}_2(\text{OAc})_4]/\text{RNase A}$  adduct crystals were prepared in shorter times than using protein crystals obtained into C2 space group (26 h against three weeks, respectively).

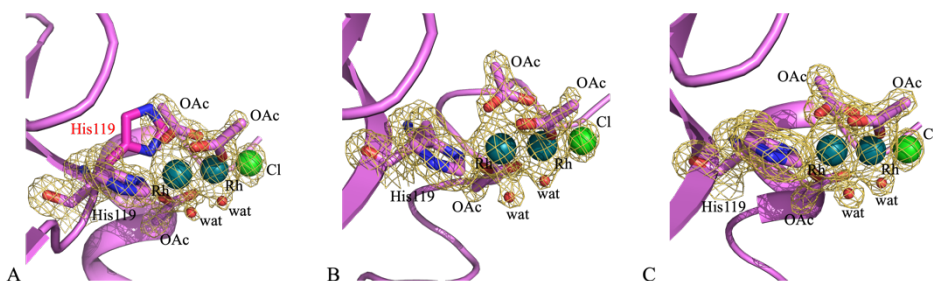


Figure 4.55. Details of His119 binding sites in the crystal structures of the  $[\text{Rh}_2(\text{OAc})_4]/\text{RNase A}$  adduct obtained upon 1 h (panel A), 2 h (panel B) and 6 h (panel C) of soaking of RNase A crystals with  $[\text{Rh}_2(\text{OAc})_4]$ .  $2\text{Fo-Fc}$  electron density maps are contoured at  $1.0\sigma$ . Label in red indicates alternative conformations.

Table 8. Rmsd obtained by superimposition of  $\text{C}\alpha$  of the structures of  $[\text{Rh}_2(\text{OAc})_4]/\text{RNase A}$  adduct each other and the metal-free RNase A.

	1 h	2 h	6 h	5OGH
1 h	0	0.059	0.061	0.336
2 h		0	0.058	0.285
6 h			0	0.302
5OGH				0

Table 9. Rh-containing fragments and ligands bound in the three structures of Rh/protein adducts obtained upon reaction of  $[\text{Rh}_2(\text{OAc})_4]$  with RNase A. Values in parenthesis indicate the occupancy of the metals and ligands. \*

Rh/RNase A adduct binding site	Metal and Ligands in crystal 1 h	Metal and Ligands in crystal 2 h	Metal and Ligands in crystal 6 h
	(1 h soaking)	(2 h soaking)	(6 h soaking)
<b>His119 (His in double conformation in crystal 1 h)</b>	Rh (0.50)	Rh (0.50)	Rh (0.55)
	Rh (0.50)	Rh (0.50)	Rh (0.55)
	OAc (0.50)	OAc (0.50)	OAc (0.55)
	OAc (0.50)	OAc (0.50)	OAc (0.55)
	OAc (0.50)	OAc (0.50)	OAc (0.55)
	H <sub>2</sub> O (0.50)	H <sub>2</sub> O (0.50)	H <sub>2</sub> O (0.55)
	H <sub>2</sub> O (0.50)	H <sub>2</sub> O (0.50)	H <sub>2</sub> O (0.55)
	Cl (0.50)	Cl (0.50)	Cl (0.55)
<b>His105 of molecule A</b>	Rh (0.75)	Rh (0.70)	Rh (0.78)
	Rh (0.75)	Rh (0.70)	Rh (0.78)
	OAc (0.75)	OAc (0.70)	OAc (0.78)
	OAc (0.75)	OAc (0.70)	OAc (0.78)
	OAc (0.75)	OAc (0.70)	OAc (0.78)
	OAc (0.75)	OAc (0.70)	OAc (0.78)
	Cl (0.75)	Cl (0.70)	Cl (0.78)

\* Metal and ligand occupancy in the RNase A crystal exposed to dirhodium tetraacetate for 2 h (0.70) is slightly lower than that observed in the RNase A crystal exposed to the metal compound for 1 h (0.75). This small difference is not significant and could be due to different crystal properties, including volume and ability to diffract X-ray.

ß

#### 4.29. Effect of temperature on $\text{CL}_{-}[\text{Rh}_2(\text{OAc})_4]/\text{RNase A}$ adduct crystals

X-ray data collection usually occurs at  $-173\text{ }^\circ\text{C}$ , a temperature that is far from that used for common chemical applications like catalysis. Before testing if  $\text{CL}_{-}\text{Rh}/\text{RNase A}$  crystals can be used as heterogeneous catalysts, the structure of

the metal/protein adduct from CLPCs was solved by X-ray crystallography at two different temperatures: -173 and 0 °C.

CL\_**Rh**/RNase A crystals for these experiments were prepared as follows: RNase A crystals were grown in 2.5 M NaCl, 3.3 M sodium formate and 0.1M sodium acetate at pH 5.2. The crystals were then exposed to GA for 2 h to form CL\_RNase A crystals. These crystals were then soaked in a solution containing  $[\text{Rh}_2(\text{OAc})_4]$  dissolved in the crystallization buffer for 24 h.

X-ray diffraction data on these crystals were collected at the two temperatures using a Rigaku XtaLAB Synergy-DW diffractometer equipped with HyPix-6000HE detector. The structures obtained from data collected at -173 and 0 °C were refined at 1.5 and 1.6 Å resolution, respectively. Data collection and refinement statistics are reported in Table G (Appendix). The two structures are very similar to each other and to the metal-free protein structure (Table 10). From the overlap of the structures of  $[\text{Rh}_2(\text{OAc})_4]$ /RNase A adducts derived from crystals that were treated or not treated with GA (Table 10) it emerges that the cross-linking does not perturb the overall protein structure. As observed in all the above-mentioned structures of  $[\text{Rh}_2(\text{OAc})_4]$ /RNase A adducts, two metal binding sites are observed, close to His105 and 119 side chains (Figure 4.56).

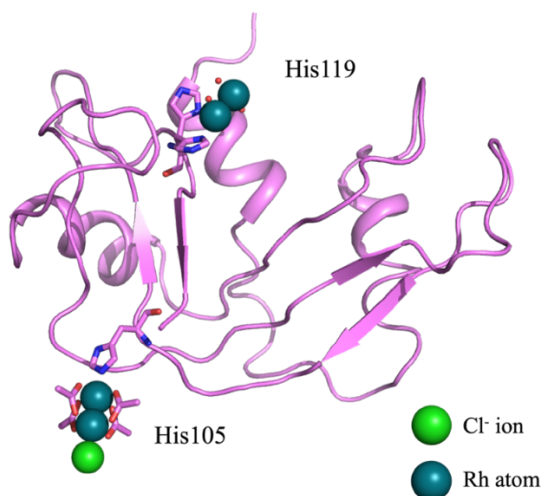


Figure 4.56. Overall structure of  $[\text{Rh}_2(\text{OAc})_4]$ /RNase A adduct in the CL\_**Rh**/RNase A crystal (0 °C).

Table 10. Rmsd obtained by superimposition of C $\alpha$  of the structures of CL\_**Rh**/RNase A crystals, [Rh<sub>2</sub>(OAc)<sub>4</sub>]/RNase A adduct crystals and the metal-free RNase A. -273 °C and 0 °C refer to the temperature of data collection of the CL\_**Rh**/RNase A crystals. 1 h, 2, and 6 h refers to Table 8.

	-273°C	0°C	1 h	2 h	6 h	5OGH
-273°C	0	0.142	0.080	0.064	0.092	0.259
0°C		0	0.139	0.130	0.119	0.318
1 h			0	0.059	0.061	0.336
2 h				0	0.058	0.285
6 h					0	0.302
5OGH						0

In both the structures, a [Rh<sub>2</sub>(OAc)<sub>4</sub>] core (occupancy 0.75-0.80) is found close to His105 side chain, axially coordinated to a Cl<sup>-</sup> ion and to the imidazole ring of the protein residue (Figure 4.57).

Major differences between the two structures are observed close to His119 side chain. In both the structures, His119 presents two different conformations, one axially coordinated to the dirhodium core and the other perpendicular to the Rh-Rh axis (Figure 4.58). The low occupancy of the Rh atoms (0.35 in both the structures) makes the electron density hard to model at this binding site. However, in the structure recorded at low temperature, one acetate ligand and two water molecules were modelled, but the other ligands are missing (Figure 4.58 A). In the structure obtained from data collection at 0 °C only four water molecules can be modelled around the dirhodium core at equatorial positions (Figure 4.58 B), the other ligands are missing. Hence, it seems that the dimetallic core bound to His119 side chain can have a more extensive hydrolysis at higher temperature. However, further studies are needed to confirm this hypothesis.

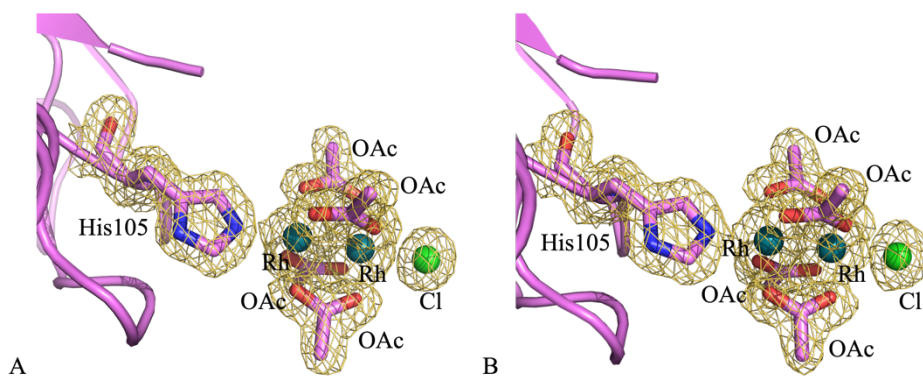


Figure 4.57. 2Fo-Fc electron density maps ( $1.0\sigma$ ) of His105 binding site in CL\_**Rh**/RNase A crystals, as calculated using X-ray diffraction data collected at  $-273\text{ }^{\circ}\text{C}$  (panel A) and  $0\text{ }^{\circ}\text{C}$  (panel B).

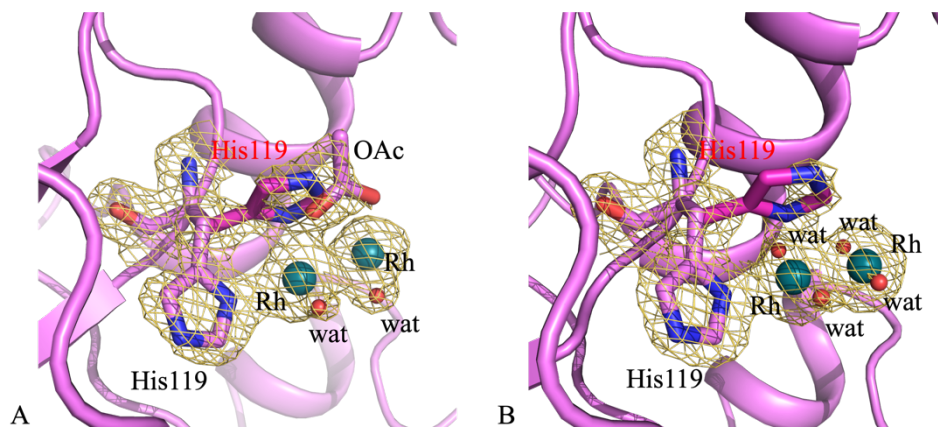


Figure 4.58. 2Fo-Fc electron density maps ( $1.0\sigma$ ) of His119 binding site in CL\_**Rh**/RNase A crystals, as calculated using X-ray diffraction data collected at  $-273\text{ }^{\circ}\text{C}$  (panel A) and  $0\text{ }^{\circ}\text{C}$  (panel B).

Comparison of the results obtained from  $[\text{Rh}_2(\text{OAc})_4]/\text{RNase A}$  and CL\_**Rh**/RNase A crystals indicates that the binding of  $[\text{Rh}_2(\text{OAc})_4]$  to the protein

close to His105 side chain is not affected by the cross-linking, while in the binding site close to His119 side chain the Rh occupancy decreases from 0.55 to 0.35 upon treatment of crystals with GA.

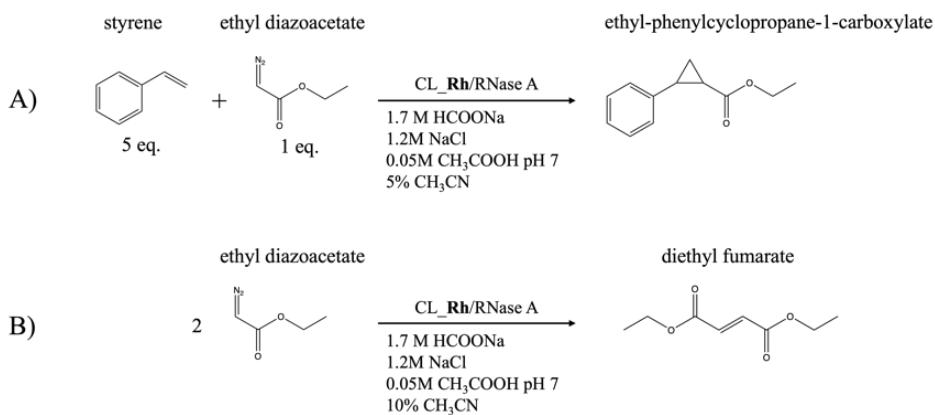
These results reveal that CL\_RNase A crystals can be efficiently metalated by  $[\text{Rh}_2(\text{OAc})_4]$  via soaking and that the metal compound binding to the protein is not significantly affected by temperature.

#### 4.30. CL\_Rh/RNase A as catalysts

The use of CPLCs as catalysts requires a large amount of crystals, that cannot be obtained using hanging drop vapor diffusion technique. To overcome this problem, RNase A crystals were grown using the batch technique and then treated with GA and functionalized with  $[\text{Rh}_2(\text{OAc})_4]$  (see methods).

Catalytic activity of CL\_Rh/RNase A crystals was then assayed toward two reactions that are catalysed by  $[\text{Rh}_2(\text{OAc})_4]$ : the olefin cyclopropanation and the self-coupling of diazo compounds. Styrene and ethyl diazoacetate were used as substrates for cyclopropanation reaction (Scheme 4 A). The diazo compound was also used as a model system for the self-coupling of diazo compounds (Scheme 4 B). The reactions were performed at 4 °C in aqueous media (see Methods for details).

GC-MS analysis of the reaction products revealed that CL\_Rh/RNase A crystals promote both the reactions (Figures 3.59 and 3.60). Indeed, MS analysis of chromatographic peaks of the self-coupling of diazo compounds reaction products revealed the presence of the expected product, the diethyl fumarate, at  $t_R = 9.63$  min, and of its hydrolysed derivative, at  $t_R = 9.34$  min (Table 11). A deeper inspection of the chromatogram also reveals the presence of several by-products of the reaction. Further studies are needed to correctly identify all the species formed upon the reaction. However, a certain amount of the unreacted ethyl diazoacetate at retention time ( $t_R$ ) of 4.33 min can be easily identified (Table 11).



Scheme 4. A: olefin cyclopropanation. B: self-coupling of diazo compounds.

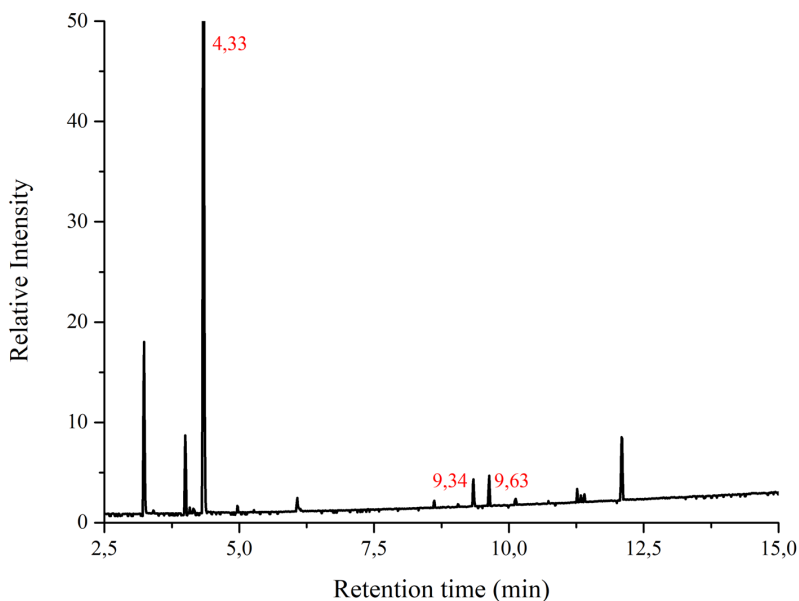


Figure 4.59. Chromatogram of the reaction products derived from the self-coupling of diazo compounds reaction catalysed by CL\_Rh/RNase A crystals. Retention times of identified reaction products are shown in red.

Better results are obtained with the olefin cyclopropanation reaction. MS analysis of chromatographic peaks of this reaction products reveals that styrene is selectively converted into the two *cis* and *trans* isomers of the ethylphenylcyclopropane-1-carboxylate. Two peaks at  $t_R = 13.38$  and  $14.08$  min, assigned to the two isomers of the cyclopropane adduct, are indeed found in the chromatogram, as reported in Figure 4.60 (Table 11). Control experiments using CL\_RNase A crystals as catalysts under the same experimental conditions revealed that without the metal compound the CLPCs don't promote the two studied reactions.

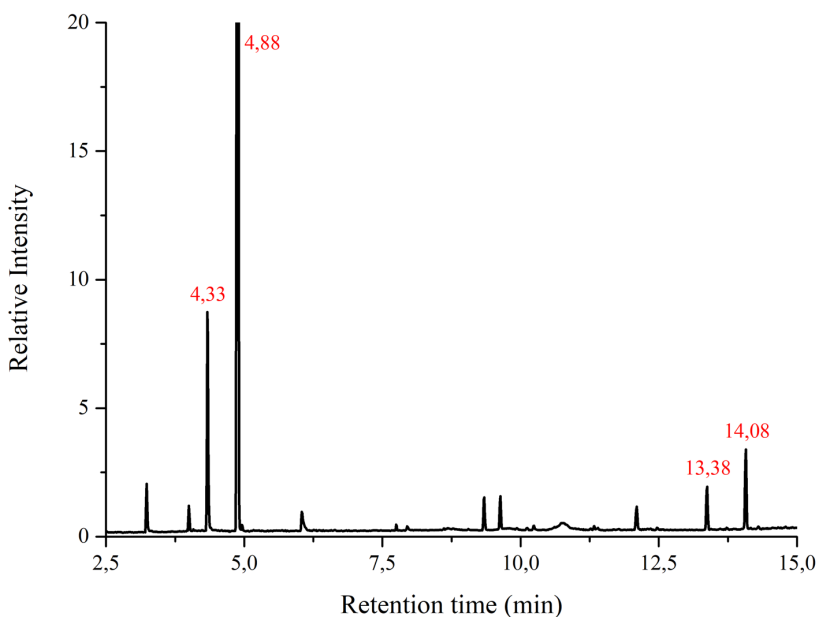


Figure 4.60. Chromatogram of the reaction products derived from the olefin cyclopropanation reaction catalysed by CL\_Rh/RNase A crystals. Retention times of identified reaction products are shown in red.

Table 11.  $t_R$ , theoretical molecular weight and experimental mass of molecular radical cation of the reactants and products obtained upon styrene

cyclopropanation and ethyl diazoacetate coupling reactions catalysed by CL\_Rh/RNase A crystals.

chemical	t <sub>R</sub> (min)	Molecular weight (Da)	Mass of molecular radical cation (m/z)
styrene	4.88	104.15	104
ethyl diazoacetate	4.33	114.10	114
(E)-4-ethoxy-4-oxobut-2-enoic acid (hydrolysis product of the diethyl fumarate)	9.34	144.04	n.o. (b.p. 99)
diethyl fumarate	9.63	172.18	n.o. (b.p. 127)
<i>cis</i> -ethyl-phenylcyclopropane-1-carboxylate	13.38	190.24	190
<i>trans</i> -ethyl-phenylcyclopropane-1-carboxylate	14.08	190.24	190

\*n.o. = not observed. b.p. = base peak.

#### 4.31. Identification of reaction products derived from styrene cyclopropanation promoted by CL\_Rh/RNase A crystals

Inspection of Figure 4.60 shows a different intensity of the two peaks attributed to the *cis* and *trans* isomers of the ethyl-phenylcyclopropane-1-carboxylate. From GC-MS analysis the identity of the two isomers cannot be assigned. Hence, the two compounds were synthesised using [Rh<sub>2</sub>(OAc)<sub>4</sub>] as a catalyst and the *cis* isomer was isolated by column chromatography on silica gel. The identity of the two compounds was confirmed by <sup>1</sup>H-NMR (Figure 4.60) spectra that are in agreement with literature data.<sup>135</sup>

The chromatogram derived by GC-MS of the *cis*-ethyl-phenylcyclopropane-1-carboxylate shows a peak at t<sub>R</sub> = 13.38 min, perfectly matching the results

displayed in Figure 4.60. Hence, the peak at  $t_R = 14.08$  min in Figure 4.60 can be assigned to the *trans*-ethyl-phenylcyclopropane-1-carboxylate. The ratio of these peaks (1.1:1) indicates a slight preference of the CL\_Rh/RNase A crystals in catalysing the formation of the *trans* rather than the *cis* isomer.

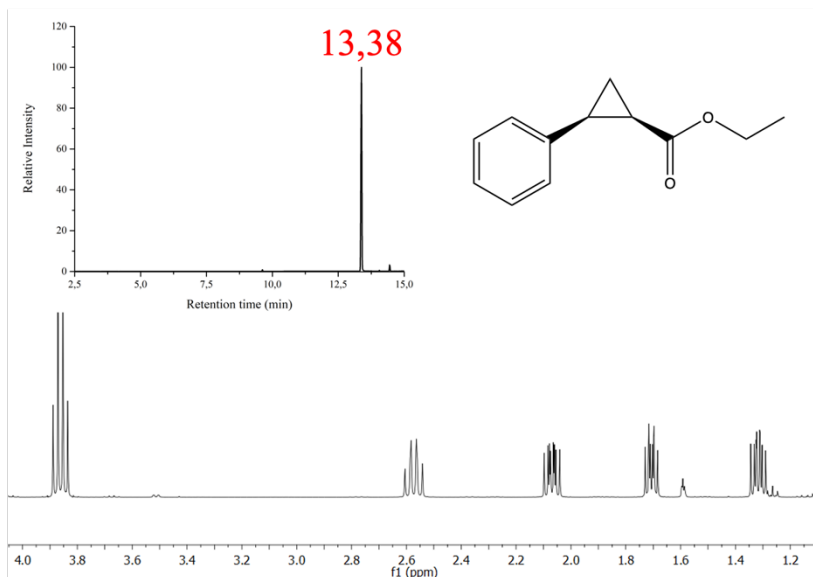


Figure 4.60. Close-up of <sup>1</sup>H-NMR spectrum of the *cis*-ethyl-phenylcyclopropane-1-carboxylate. A snapshot of the GC chromatogram of this compound is shown on the left.

#### 4.32. Summary of the development of CL\_RNase A crystals functionalised with [Rh<sub>2</sub>(OAc)<sub>4</sub>] as biohybrid materials for heterogeneous catalysis

The structure of the adduct formed upon reaction of RNase A with dirhodium tetraacetate derived from crystals in a different space group was solved. The results revealed that the protein is metalated within 2 h of soaking with the metal complex. These data suggest that this crystal form can be used to prepare CLPCs. Thus, cross-linked protein crystals of the [Rh<sub>2</sub>(OAc)<sub>4</sub>]/RNase A adduct were prepared. The structure of the adduct derived from these crystals, also solved at two different temperatures, reveals that the cross-linking does not affect the

binding of the dirhodium core to the His side chains. CL\_**Rh**/RNase A crystals are efficient catalysts for olefin cyclopropanation, while they catalyse self-coupling of diazo compounds reactions leading to the formation of several by-products beyond the expected one. Hence, CL\_**Rh**/RNase A crystals have the potential to be used as biohybrid materials that can be used in catalysis.

## RESULTS AND DISCUSSION

## 5. METHODS

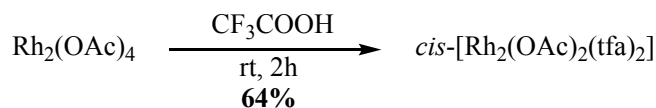
### 5.1. Materials

[Rh<sub>2</sub>(OAc)<sub>4</sub>], CF<sub>3</sub>COOH, buffers, salts, HEWL and RNase A used for preparing protein crystals in the C2 space group were purchased from Sigma Chemical Co. RNase A used for crystallization trials in the P3<sub>2</sub>21 space group and reactants used for catalytic experiments were obtained from TCI (Wako, Nacalai Tesque). All the organic solvents were purchased from VWR (Milan, Italy) or Merck Life Science. All the chemicals used in this thesis were at the highest degree of purity available and were used without further purification.

### 5.2. Synthesis of the compounds used in this thesis

Preparation of *cis*-[Rh<sub>2</sub>(OAc)<sub>2</sub>(tfa)<sub>2</sub>].

*cis*-[Rh<sub>2</sub>(OAc)<sub>2</sub>(tfa)<sub>2</sub>] was synthesised as previously described,<sup>121</sup> following Scheme 5.

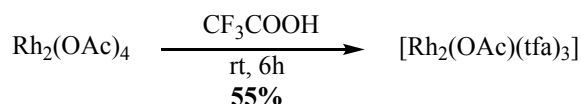


Scheme 5. Synthesis of *cis*-[Rh<sub>2</sub>(OAc)<sub>2</sub>(tfa)<sub>2</sub>].

15.2 mg (0.034 mmol) of [Rh<sub>2</sub>(OAc)<sub>4</sub>] were dissolved in an excess of TFA (2 ml) and the mixture was stirred at room temperature for 2 h. The reaction was monitored by TLC (precoated silica gel F254, Merck, Darmstadt, Germany). Then, the mixture was concentrated under reduced pressure and purified by chromatography (Merck Kieselgel 60) of the crude residue over silica gel (toluene/acetonitrile = 8:2). *cis*-[Rh<sub>2</sub>(OAc)<sub>2</sub>(tfa)<sub>2</sub>] was obtained (22.4 mg, 64% yield) as a purple powder along with a small amount of [Rh<sub>2</sub>(OAc)(tfa)<sub>3</sub>] (2.1 mg). <sup>1</sup>H and <sup>19</sup>F NMR spectra were consistent with those reported in literature.<sup>121</sup>

Preparation of [Rh<sub>2</sub>(OAc)(tfa)<sub>3</sub>].

Synthesis of [Rh<sub>2</sub>(OAc)(tfa)<sub>3</sub>] was performed as summarised in scheme 6.

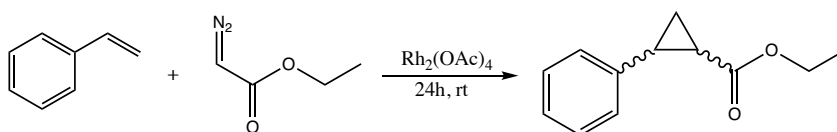


Scheme 6. Synthesis of [Rh<sub>2</sub>(OAc)(tfa)<sub>3</sub>].

[Rh<sub>2</sub>(OAc)<sub>4</sub>] (17.5 mg, 0.039 mmol) was dissolved in an excess of TFA (2 ml). The reaction was monitored as described above for *cis*-[Rh<sub>2</sub>(OAc)<sub>2</sub>(tfa)<sub>2</sub>]. Afterwards, the mixture was concentrated under reduced pressure and the crude residue was purified on silica gel (toluene/acetonitrile = 99:1). Pure [Rh<sub>2</sub>(OAc)(tfa)<sub>3</sub>] was obtained with 55% yield (13.1 mg) as blue powder. <sup>1</sup>H and <sup>19</sup>F NMR spectra were consistent with those reported in literature.<sup>121</sup>

Preparation of ethyl-phenylcyclopropane-1-carboxylate.

*cis* and *trans* mixture of ethyl-phenylcyclopropane-1-carboxylate was prepared accordingly to previous reported data, as shown in scheme 7.<sup>136</sup>



Scheme 7. Synthesis of *cis/trans* mixture of ethyl-phenylcyclopropane-1-carboxylate.

4.5 g (43 mmol) of styrene were dissolved in 5.0 ml of  $\text{CH}_2\text{Cl}_2$ . 6.8 mg of  $[\text{Rh}_2(\text{OAc})_4]$  were added to the solution. A solution of ethyl diazoacetate (7.8 mg, 68 mmol) in  $\text{CH}_2\text{Cl}_2$  (7.2 ml) was added dropwise to the reaction mixture at room temperature over 5 h. An additional  $[\text{Rh}_2(\text{OAc})_4]$  amount (1.0 mg) was added to the solution after 4 h. Upon 24 h, the mixture was concentrated under reduced pressure and purified by chromatography (Merck Kieselgel 60) of the crude residue over silica gel (ethyl acetate/hexane = 9:1). *cis*-ethyl-phenylcyclopropane-1-carboxylate was obtained (39.4 g, 48,6% yield) as a pale-yellow oil.  $^1\text{H}$  spectra were consistent with those reported in literature.<sup>136</sup>

### 5.3. UV-vis absorption spectroscopy

#### Stability of $[\text{Rh}_2(\text{OAc})_4]$ in crystallization buffer.

UV-vis absorption spectra of  $[\text{Rh}_2(\text{OAc})_4]$  were recorded using a Jasco V580 spectrophotometer (Jasco Corp. Milan, Italy). Spectra were acquired over time up to 24 h in 10.0 mM sodium acetate buffer at pH 4.5 and 10.0 mM HEPES buffer at pH 7.5 using a metal concentration of 0.8 mM. UV-vis spectra were collected at room temperature in the 340-700 nm range every 1 nm at a scan rate of 400 nm  $\text{min}^{-1}$ .

#### Stability of *cis*- $[\text{Rh}_2(\text{OAc})_2(\text{tfa})_2]$ and $[\text{Rh}_2(\text{OAc})(\text{tfa})_3]$ in aqueous solutions in the absence and in the presence of proteins.

UV-vis absorption spectra of *cis*- $[\text{Rh}_2(\text{OAc})_2(\text{tfa})_2]$  and  $[\text{Rh}_2(\text{OAc})(\text{tfa})_3]$  were collected at room temperature using a Jasco V750 UV-vis spectrophotometer in the 340-700 nm range. For each metal compound, spectra were recorded in 10.0 mM sodium citrate buffer at pH 5.1 and 5.0 mM HEPES buffer at pH 7.5, using 0.5 mM of each metal compound, in the absence and in the presence of HEWL and RNase A (protein to metal molar ratio 1:3). Spectra were acquired every 1 nm at a scan rate of 200 nm  $\text{min}^{-1}$ .

#### 5.4. Far UV-CD spectroscopy

Circular dichroism spectra of HEWL in the presence of  $[\text{Rh}_2(\text{OAc})_4]$  were registered using samples obtained upon 24 h incubation of the protein with the metal compound at a 1:3 molar ratio in 4.0 mM sodium acetate buffer at pH 4.4 and 4.0 mM HEPES buffer at pH 7.5. Spectra of HEWL and RNase A in the presence of *cis*- $[\text{Rh}_2(\text{OAc})_2(\text{tfa})_2]$  and  $[\text{Rh}_2(\text{OAc})(\text{tfa})_3]$  were recorded in 5.0 mM HEPES at pH 7.5 and 10.0 mM sodium citrate buffer pH at 5.1, respectively. The proteins were incubated with a metal to protein ratio 3:1 for 24 h before the spectroscopic measurement. CD experiments were performed using a Jasco J-810 spectropolarimeter (Jasco Corp. Milan, Italy) at 25 °C. Quartz cells with path length of 0.1 cm were used in the far-UV region from 200 to 250 nm. Three scans were recorded for each spectrum, contributions from the corresponding reference were subtracted and the signal converted to mean residue molar ellipticity in units of  $\text{deg cm}^{-2} \text{dmol}^{-1}$ . Other experimental settings were: 50  $\text{nm min}^{-1}$  scan speed, 2.0 nm band width, 0.2 nm resolution, 50 mdeg sensitivity and 4 s response.

#### 5.5. $^{19}\text{F}$ NMR spectroscopy

$^{19}\text{F}$  NMR spectra of *cis*- $[\text{Rh}_2(\text{OAc})_2(\text{tfa})_2]$  and  $[\text{Rh}_2(\text{OAc})(\text{tfa})_3]$  were recorded at 25 °C using a Bruker AVANCE spectrometer (Billerica, Massachusetts, US) operating at 376 MHz with TOPSPIN using autolocking and auto shimming. Chemical shifts ( $\delta$ ) are reported as parts per million (ppm). To collect spectra of the metal compounds, *cis*- $[\text{Rh}_2(\text{OAc})_2(\text{tfa})_2]$  or  $[\text{Rh}_2(\text{OAc})(\text{tfa})_3]$  were dissolved in  $\text{CDCl}_3$  and analysed by  $^{19}\text{F}$  NMR. Spectra were collected in 10 mM sodium citrate at pH 5.1 and 5 mM HEPES at pH 7.5 (10%  $\text{D}_2\text{O}$ ) using a 5.0 mM concentration of *cis*- $[\text{Rh}_2(\text{OAc})_2(\text{tfa})_2]$  or  $[\text{Rh}_2(\text{OAc})(\text{tfa})_3]$  in the absence and in the presence of RNase A and HEWL (metal/protein ratio = 3:1). Spectra of pure TFA in the same buffer were collected as reference (10 mM sodium citrate at pH 5.1 and 5 mM HEPES at pH 7.5 with 10%  $\text{D}_2\text{O}$ ).

$^{19}\text{F}$  { $^1\text{H}$  dec} NMR data in  $\text{CDCl}_3$  (characterization of dirhodium compounds).

*cis*- $[\text{Rh}_2(\text{OAc})_2(\text{tfa})_2]$ .  $\delta = -74.7$  ppm.

$[\text{Rh}_2(\text{OAc})(\text{tfa})_3]$ .  $\delta = -74.7, -74.9$  ppm.

$^{19}\text{F}$  { $^1\text{H}$  dec} NMR data in 10.0 mM sodium citrate buffer 10%  $\text{D}_2\text{O}$  at pH 5.1.

TFA.  $t = 5$  min,  $\delta = -75.5$  ppm.

*cis*- $[\text{Rh}_2(\text{OAc})_2(\text{tfa})_2]$ .  $t = 5$  min,  $\delta = -75.5, -74.8, -74.7$  ppm,  $t = 4$  h,  $\delta = -75.5, -74.7$  ppm,  $t = 24$  h,  $\delta = -75.5$  ppm.

*cis*- $[\text{Rh}_2(\text{OAc})_2(\text{tfa})_2]$  in the presence of RNase A.  $t = 5$  min,  $\delta = -75.5$  ppm.

$[\text{Rh}_2(\text{OAc})(\text{tfa})_3]$ .  $t = 5$  min,  $\delta = -75.5, -74.8, -74.7, -74.6$  ppm,  $t = 4$  h,  $\delta = -75.5, -74.6$  ppm,  $t = 24$  h,  $\delta = -75.5, -74.6$  ppm.

$[\text{Rh}_2(\text{OAc})(\text{tfa})_3]$  in the presence of RNase A.  $t = 5$  min,  $\delta = -75.5$  ppm.

$^{19}\text{F}$  { $^1\text{H}$  dec} NMR data in 5.0 mM HEPES buffer 10%  $\text{D}_2\text{O}$  at pH 7.5.

TFA.  $t = 5$  min,  $\delta = -75.4$  ppm.

*cis*- $[\text{Rh}_2(\text{OAc})_2(\text{tfa})_2]$ .  $t = 5$  min,  $\delta = -74.8$  ppm,  $t = 4$  h,  $\delta = -74.8, -75.1, -75.4$  ppm,  $t = 24$  h,  $\delta = -75.1, -75.4$  ppm.

*cis*- $[\text{Rh}_2(\text{OAc})_2(\text{tfa})_2]$  in the presence of HEWL.  $t = 5$  min,  $\delta = -74.8, -75.4$  ppm,  $t = 2$  h,  $\delta = -75.4$  ppm.

$[\text{Rh}_2(\text{OAc})(\text{tfa})_3]$ .  $t = 5$  min,  $\delta = -75.5, -74.8, -74.7$ , ppm,  $t = 4$  h,  $\delta = -75.5, -75.1, -74.8, -74.7$  ppm,  $t = 24$  h,  $\delta = -75.5, -75.1, -74.7$  ppm.

$[\text{Rh}_2(\text{OAc})(\text{tfa})_3]$  in the presence of HEWL.  $t = 5$  min,  $\delta = -74.7, -75.5$  ppm,  $t = 2$  h min,  $\delta = -75.5$  ppm.

## 5.6. $^1\text{H}$ NMR spectroscopy

$^1\text{H}$  NMR spectra of *cis*- $[\text{Rh}_2(\text{OAc})_2(\text{tfa})_2]$  and  $[\text{Rh}_2(\text{OAc})(\text{tfa})_3]$  were recorded at 25 °C using a Bruker AVANCE (400 MHz, Billerica, Massachusetts, US) or Varian Inova (500 MHz, Palo Alto, California, US) spectrometer. Chemical shifts ( $\delta$ ) are reported as parts per million (ppm). Spectra were collected upon dissolving *cis*- $[\text{Rh}_2(\text{OAc})_2(\text{tfa})_2]$  or  $[\text{Rh}_2(\text{OAc})(\text{tfa})_3]$  in  $\text{CDCl}_3$ .

$^1\text{H}$  NMR spectrum of *cis*-ethyl-phenylcyclopropane-1-carboxylate was collected at 25 °C using a JNM-ECZL400 spectrometer (400 MHz, JEOL Ltd.) using  $\text{CDCl}_3$  as solvent.

### $^1\text{H}$ NMR data in $\text{CDCl}_3$ (characterization of dirhodium compounds).

*cis*- $[\text{Rh}_2(\text{OAc})_2(\text{tfa})_2]$ .  $\delta = 2.52$  (s, coordinated acetonitrile), 1.99 (6H) ppm.

$[\text{Rh}_2(\text{OAc})(\text{tfa})_3]$ .  $\delta = 2.63$  (s, coordinated acetonitrile), 2.02 (s, 3H). ppm.

*cis*-ethyl-phenylcyclopropane-1-carboxylate.  $\delta = 7.25$  (m, 4H), 7.18 (m, 1H), 3.87 (q, 2H), 2.56 (dd, 1H), 2.06 (m, 1H), 1.70 (m, 1H), 1.30 (m, 1H), 0.95 (t, 3H) ppm.

## 5.7. Crystallization of metal/protein adducts

### $[\text{Rh}_2(\text{OAc})_4]$ /HEWL adduct crystals

Cocrystallization (Crystal 1-4, Table A, Appendix) of  $[\text{Rh}_2(\text{OAc})_4]$  with HEWL was performed using the following procedure. HEWL (14 mg  $\text{ml}^{-1}$ ) and  $[\text{Rh}_2(\text{OAc})_4]$  were mixed in water at room temperature (metal/protein ratio = 10:1) and the solution was stirred for 24 h. Crystals of metal/protein adduct were grown by hanging drop vapor diffusion method using 1  $\mu\text{l}$  of adduct solution and an equal volume of a solution consisting of 20% ethylene glycol, 0.100 M sodium acetate at pH 4.5 and 0.600 M sodium nitrate.

Soaking experiments were performed using HEWL crystals prepared in 20% ethylene glycol, 0.10 M sodium acetate at pH 4.5 and 0.60 M sodium nitrate or 2.0 M sodium formate (Crystal 5, Table A, Appendix) and 0.010 M HEPES at pH 7.5 (Crystal 6, Table A, Appendix). In the former crystallization condition, soaking was performed using a reservoir solution saturated with  $[\text{Rh}_2(\text{OAc})_4]$  for 1 year. In the latter case, HEWL crystals were soaked in a solution of the reservoir saturated with the metal compound for 7 days.

Crystals of the adducts formed upon reaction of *cis*- $[\text{Rh}_2(\text{OAc})_2(\text{tfa})_2]$  and  $[\text{Rh}_2(\text{OAc})(\text{tfa})_3]$  with RNase A (C2 space group) and HEWL

RNase A crystals in the C2 space group were grown at 298 K using the hanging drop vapor diffusion technique, using a protein concentration of 22 mg ml<sup>-1</sup> and a reservoir consisting of 22% PEG 4 K and 0.010 M sodium citrate buffer at pH 5.1.

HEWL crystals (18 mg ml<sup>-1</sup>) were grown at 298 K using 2.00 M sodium formate and 0.10 M HEPES buffer at pH 7.5.

Metal/protein adducts were obtained using the soaking method, exposing the metal-free protein crystals to a reservoir solution containing the metal complex. Details of soaking procedures can be found in Tables B and C (Appendix).

Reaction of  $[\text{Rh}_2(\text{OAc})_4]$ /RNase A adduct crystals with imidazole and glycine.

RNase A crystals in the C2 space group were grown at 298 K using the hanging drop vapor diffusion technique, equilibrating a protein solution (22 mg ml<sup>-1</sup>) against a reservoir consisting of 22% PEG 4 K and 0.010 M sodium citrate buffer at pH 5.1 for two weeks. Crystals were exposed to a saturated solution of  $[\text{Rh}_2(\text{OAc})_4]$  and successively to a saturated solution of imidazole in the reservoir for 44 days (Table D, Appendix). In a similar experiment, crystals were treated with glycine instead of imidazole (Table E, Appendix). In parallel experiments, crystals were treated with serine, methionine, pyridine and KSCN, but X-ray

diffraction data on these crystals do not allow to evaluate if these molecules are bound to dirhodium moiety coordinated to His side chains or not.

#### [Rh<sub>2</sub>(OAc)<sub>4</sub>]/RNase A adduct crystals (P3<sub>2</sub>21 space group).

RNase A crystals in the P3<sub>2</sub>21 space group were grown at 298 K using the hanging drop vapor diffusion technique, using a protein concentration of 50 mg ml<sup>-1</sup> and a reservoir consisting of 50% NaCl, 30% (NH<sub>4</sub>)<sub>2</sub>SO<sub>4</sub> and 0.1 M sodium acetate buffer pH 4.8-5.5 or 2.5 M NaCl, 3.3 M sodium formate, 0.1 M sodium acetate buffer pH 4.7-5.5. Soaking was performed transferring crystals into a solution consisting of 3.3 M sodium formate, 0.1 M sodium acetate buffer pH 4.7-5.5 saturated with [Rh<sub>2</sub>(OAc)<sub>4</sub>] for 1 h, 2 h or 6 h (Table F, Appendix).

#### CL\_[Rh<sub>2</sub>(OAc)<sub>4</sub>]/RNase A adduct crystals (P3<sub>2</sub>21 space group).

RNase A crystals in the P3<sub>2</sub>21 space group, grown as described in the previous paragraph using the crystallization condition containing sodium formate, were washed and equilibrated with a reservoir consisting of 2.5 M NaCl, 3.3 M sodium formate, 0.1 M sodium acetate buffer pH 4.7-5.5 with 0.5% GA. After 2 h of exposure to the cross-linker, CL\_RNase A crystals were formed. These crystals were equilibrated against the original reservoir. To obtain cross-linked crystals of the adduct with [Rh<sub>2</sub>(OAc)<sub>4</sub>], CL\_RNase A crystals were then soaked into a solution consisting of 2.5 M NaCl, 3.3 M sodium formate, 0.1 M sodium acetate buffer pH 4.7-5.5 saturated with [Rh<sub>2</sub>(OAc)<sub>4</sub>] for 24 h (Table G).

#### Preparation of CL\_[Rh<sub>2</sub>(OAc)<sub>4</sub>]/RNase A adduct crystals (P3<sub>2</sub>21 space group) on large scale

A large amount of protein crystals is required for catalytic experiments. Hence, RNase A crystals were prepared using the batch technique as follows: 100 µl of RNase A (300 mg ml<sup>-1</sup>) were diluted up to 500 µl with a solution consisting of 2.5

M NaCl, 3.3 M sodium formate, 0.1 M sodium acetate buffer pH 5.2 (protein final concentration = 60 mg ml<sup>-1</sup>). The solution was equilibrated for 24 h at 293 K. A large amount of crystals was obtained. 0.1 % GA was added to the crystal solution. After 90 minutes CL\_RNase A (yellow) were obtained. CLPCs were washed with crystallization buffer and soaked with the same buffer saturated with [Rh<sub>2</sub>(OAc)<sub>4</sub>] for 6 h. Upon protein metalation, pink crystals were observed.

### 5.8. X-ray diffraction data collection, structure solution and refinement

#### [Rh<sub>2</sub>(OAc)<sub>4</sub>]/HEWL adduct structures

X-ray diffraction data collection on crystals of the [Rh<sub>2</sub>(OAc)<sub>4</sub>]/HEWL adducts was performed at 100 K. Crystals 1 and 2 were flash frozen without cryoprotectant. Crystals 3-6 were flash-frozen using 30% (V/V) glycerol as cryoprotectant.

Data collection on Crystals 1 and 2 was carried out at the CNR Institute of Biostructure and Bioimaging in Naples, Italy, using a Saturn944 CCD detector equipped with CuK $\alpha$  X-ray radiation generator from a Rigaku Micromax 007 HF generator. X-ray diffraction data on Crystals 3 and 6 were collected at the XRD2 Beamline of Elettra synchrotron in Trieste, Italy. Data collection on Crystals 4 and 5 was carried out at Diamond Light Source synchrotron in Oxfordshire, UK. Data were scaled using HKL2000,<sup>137</sup> Mosflm/Scala,<sup>138</sup> or AutoPROC.<sup>139</sup> Data collection and refinement statistics are reported in Table A (Appendix). The structures were solved in the P4<sub>3</sub>2<sub>1</sub>2 space group by molecular replacement method using Phaser.<sup>140</sup> Metal-free HEWL (PDB code: 193L)<sup>112</sup> was used as starting model. Refmac5<sup>141</sup> was used for restrained refinement and model building was carried out using Coot.<sup>142</sup> Rh positions in the electron density maps were confirmed by inspection of anomalous difference maps. PDB validation server (www.rcsb.org) was used for structure validation. Structures were deposited on PDB with accession codes: 7BDZ, 7BE0, 7BE1, 7BE2, 7BEB and 7BEC.

Structures derived from the adducts obtained upon reaction of *cis*-[Rh<sub>2</sub>(OAc)<sub>2</sub>(tfa)<sub>2</sub>] with RNase A and HEWL

Four different crystals of RNase A and one crystal of HEWL in adduct with *cis*-[Rh<sub>2</sub>(OAc)<sub>2</sub>(tfa)<sub>2</sub>] were exposed to X-ray radiation at the XRD2 beamline of Elettra synchrotron in Trieste, Italy. AutoPROC<sup>139</sup> pipeline was used for data processing and scaling. Data collection and refinement statistics are reported in Table B (Appendix). Crystal structures were solved by molecular replacement using Phaser.<sup>140</sup> PDB code 1JVT<sup>122</sup> (chain A without waters) and 193L<sup>112</sup> were used as molecular search models of RNase A and HEWL, respectively. Structures of the metal/RNase A adduct were solved in the C2 space group with two molecules in the asymmetric unit, while the metal/HEWL structure was solved in the P4<sub>3</sub>2<sub>1</sub>2 space group. Coot was used for building models and for electron density maps visualization.<sup>142</sup> Refinement was carried out using Refmac5.<sup>141</sup> Structure 1 was refined anisotropically, while the remaining structures were refined isotropically. PDB validation server was used for structural validation. Rh atom positions were validated by anomalous electron density maps. The structures of *cis*-[Rh<sub>2</sub>(OAc)<sub>2</sub>(tfa)<sub>2</sub>]/RNase A adduct were deposited in the PDB with accession codes 7QPW, 7QQ0, 7QPY, and 7QPZ. *cis*-[Rh<sub>2</sub>(OAc)<sub>2</sub>(tfa)<sub>2</sub>]/HEWL adduct structure was deposited in the PDB under the accession code 7QQ1.

Structures derived from the adducts obtained upon reaction of [Rh<sub>2</sub>(OAc)(tfa)<sub>3</sub>] with RNase A and HEWL

X-ray diffraction data on adducts of [Rh<sub>2</sub>(OAc)(tfa)<sub>3</sub>] with RNase A and HEWL were collected at the XRD2 beamline of Elettra synchrotron in Trieste, Italy. Before data collection, 20% (V/V) glycerol was added to the mother liquor solution of crystals. Afterwards, crystals were flash-cooled with liquid N<sub>2</sub>.

Data processing, structure solution and refinement were performed as described above for the of *cis*-[Rh<sub>2</sub>(OAc)<sub>2</sub>(tfa)<sub>2</sub>]/protein structures. Data collection and refinement statistics are reported in Table C (Appendix). [Rh<sub>2</sub>(OAc)(tfa)<sub>3</sub>]/RNase A and [Rh<sub>2</sub>(OAc)(tfa)<sub>3</sub>]/HEWL adduct structures were deposited in the PDB under the accession code 7Z6D, 7Z6G and 7Z6G, respectively.

[Rh<sub>2</sub>(OAc)<sub>4</sub>]/RNase A adduct crystals upon reaction with imidazole and glycine

X-ray diffraction data on [Rh<sub>2</sub>(OAc)<sub>4</sub>]/RNase A adduct crystals treated with imidazole and glycine were collected at 100 K at Elettra synchrotron in Trieste, Italy. Before data collection, 20% (V/V) glycerol was added to the mother liquor and crystals were flash cooled with liquid N<sub>2</sub>. Data processing, structure resolution and refinement were performed as described in previous paragraphs. Data collection and refinement statistics are reported in Table D and E (Appendix). The crystal structure from crystals ntreated with imidazole was deposited in the PDB under the accession code 7QHR.

[Rh<sub>2</sub>(OAc)<sub>4</sub>]/RNase A adduct structures in the P3<sub>2</sub>21 space group

X-ray diffraction data on [Rh<sub>2</sub>(OAc)<sub>4</sub>]/RNase A adduct crystals in the P3<sub>2</sub>21 space group were collected using a Rigaku XtaLAB Synergy-DW diffractometer equipped with HyPix-6000HE detector at the School of Life Science and Technology of the Tokyo Institute of Technology, Yokohama, Japan. Data processing and scaling were carried out using Aimless.<sup>143</sup> Data collection and refinement statistics are reported in Table E (Appendix). Crystal structures were solved and refined as described in previous paragraphs (Table F). PDB code 5OGH was used as search model for molecular replacement.<sup>134</sup>

CL\_Rh/RNase A adduct structures

X-ray diffraction data were collected at 100 K and at 273 K on two crystals of the CL\_Rh/RNase A adduct using a Rigaku XtaLAB Synergy-DW diffractometer equipped with HyPix-6000HE detector at the School of Life Science and Technology of the Tokyo Institute of Technology, Yokohama, Japan. Data processing, structure solution and refinement were carried out as described in the previous paragraph. Data collection and refinement statistics are reported in Table G (Appendix).

## 5.9. CLPCs catalysis

### Olefin cyclopropanation reaction

CL\_**Rh**/RNase A crystals prepared on large scale as described above were dissolved in 500  $\mu\text{l}$  of a solution consisting of 1.25 M NaCl, 1.75 M sodium formate and 0.50 M sodium acetate. pH was adjusted at 7.8. 25  $\mu\text{l}$  of styrene (stock solution 0.97 M in acetonitrile) were added to the solution. Finally, 25  $\mu\text{l}$  of ethyl diazoacetate (stock solution 0.50 M in acetonitrile) were mixed in the solution (final concentrations: styrene = 4.4 mM, ethyl diazoacetate = 8.7 mM, acetonitrile = 10%). The reaction was stirred at 4  $^{\circ}\text{C}$  for 17 h. Reaction was quenched with  $\text{CHCl}_3$  and extracted three times with 600  $\mu\text{l}$  of  $\text{CHCl}_3$ . Reaction mixture was analysed by GC-MS. Rh concentration (0.5 mM) in the reaction mixture was determined by ICP-OES.

### Self-coupling of diazo compounds reaction

15  $\mu\text{l}$  of ethyl diazoacetate (stock solution 0.50 M in acetonitrile) were added to 285  $\mu\text{l}$  of a solution containing of CL\_**Rh**/RNase A crystals, 1.25 M NaCl, 1.75 M sodium formate and 0.50 M sodium acetate at pH 7 (final concentrations: ethyl diazoacetate = 2.5 mM, acetonitrile = 5%). The reaction was stirred at 4  $^{\circ}\text{C}$  for 17 h. Reaction was quenched with  $\text{CHCl}_3$  and extracted three times with  $\text{CHCl}_3$ . Reaction mixture was analysed by GC-MS. Rh concentration (0.9 mM) in the reaction mixture was determined by ICP-OES as described below.

## 5.10. GC-MS analysis

GC-MS data were collected using a Shimadzu GC-MS QP2010 spectrometer equipped with a Shimadzu SH-Rxi-5Sil MS column (inner diameter: 0.25 mm, film thickness: 0.25  $\mu\text{m}$ ). A temperature gradient of 10  $^{\circ}\text{C min}^{-1}$  was applied starting from 35  $^{\circ}\text{C}$  up to 320  $^{\circ}\text{C}$ . Before cooling down, final temperature was maintained for 2 min.

### 5.11. ICP-OES measurements

CL\_Rh/RNase A crystals were dissolved in HNO<sub>3</sub> (1 ml, 70% V/V) and diluted up to 5 ml. 77  $\mu$ l of this solution were diluted up to 10 ml. The metal concentration in the solution was determined by ICP-OES (PerkinElmer Japan, ELAN DRC-es). ICP Standard solution G (Rh concentration = 10 mg L<sup>-1</sup>, purchased by Kanto Chemical Co.) was used as calibration standard.

### 5.12. Density functional theory calculations

Gaussian16<sup>144</sup> was used for DFT calculations. C, N, H and O atoms were modelled with the TZVP basis set and the SDD effective core potential (ECP) as basis set for Rh.

Structural optimization, molecular frequencies, and thermochemistry data were collected at B3LYP level of theory,<sup>145,146</sup> including Grimme's dispersion correction D3 with the Becke-Johnson damping function.<sup>147,148</sup> Water was considered as solvent with the polarizable continuum model (PCM).<sup>149</sup> The default maximum force and displacement tolerance parameters in Gaussian were used for the ground-state minimum-energy structures. Molecular frequencies were computed within the harmonic oscillator approximation. Thermochemical data were computed at room temperature.



## 6. SUMMARY

Dirhodium paddlewheel complexes proved to be very interesting compounds in several application fields, ranging from catalysis to medicinal chemistry.<sup>9</sup> Conjugation of these complexes with proteins revealed that these complexes not only interact with these biological macromolecules forming metal/protein adducts, but also preserve and in some cases improve their performances as catalysts.<sup>80,78</sup> Despite the huge versatility that arises by the functionalization of proteins with dirhodium paddlewheel complexes, little is known about the interaction of dirhodium compounds with these macromolecules. In the last decades, X-ray crystallography has provided useful information on the interaction between proteins and metal compounds.<sup>66</sup> Recently, the stabilization of protein crystals through cross-linking techniques has expanded their range of applicability going beyond the structural determination of protein 3D structure. CLPCs have proven to be very promising materials for solid phases of chromatography, biosensing and heterogeneous catalysis.<sup>100</sup>

Hence, the purposes of this thesis were to shed light on the dirhodium complexes/proteins recognition process by X-ray crystallography and to develop CLPCs functionalized with dirhodium complexes as biohybrid materials that can be used for catalytic applications.

The interaction between  $[\text{Rh}_2(\text{OAc})_4]$ , *cis*- $[\text{Rh}_2(\text{OAc})_2(\text{tfa})_2]$  and  $[\text{Rh}_2(\text{OAc})(\text{tfa})_3]$  with two model proteins, HEWL and RNase A, was investigated both in solution and in the solid state. The reactivity of the  $[\text{Rh}_2(\text{OAc})_4]$ /RNase A adduct toward imidazole and glycine was also studied in the solid state, providing information on the reactivity of  $[\text{Rh}_2(\text{OAc})_4]$  within protein crystals.

X-ray structures of the  $[\text{Rh}_2(\text{OAc})_4]$ /HEWL adduct obtained by soaking or cocrystallization revealed similar results. The metal compound degrades upon interaction with the protein, and both monometallic and bimetallic fragments are observed within the protein scaffold (close to His15, Asp18, Lys33, Asn93/Lys96, Asp101 and C-terminal tail). Crystallization conditions play a non-innocent role in directing the reactivity of the metal compound with the protein. Upon degradation, the dirhodium compound can act as a cross-linking agent, as observed by SDS-PAGE experiments performed on dissolved crystals of the metal/protein adduct. In solution experiments revealed that the metal compound

is stable in the crystallization buffer used for growing protein crystals and that the interaction between the complex and the protein leaves the secondary structure of the macromolecule unperturbed.

When OAc is replaced by tfa in the dirhodium paddlewheel scaffold, the properties of the metal compound in aqueous solution dramatically change. *cis*-[Rh<sub>2</sub>(OAc)<sub>2</sub>(tfa)<sub>2</sub>] loses its fluorinated ligands in aqueous solutions, and this process is accelerated in the presence of HEWL and RNase A. When *cis*-[Rh<sub>2</sub>(OAc)<sub>2</sub>(tfa)<sub>2</sub>] reacts with HEWL in the solid state both Rh and Rh<sub>2</sub> units are observed close to His15 and Asp101 side chains. The X-ray structure of the adduct that *cis*-[Rh<sub>2</sub>(OAc)<sub>2</sub>(tfa)<sub>2</sub>] forms with RNase A reveals that the dimetallic core is retained upon the protein binding, but tfa ligands are hydrolysed, coherently with in solution data. The protein hosts the metal compound close to His105 and His119 side chain, via axial ligation of imidazole rings.

Similar results are observed when [Rh<sub>2</sub>(OAc)(tfa)<sub>3</sub>] reacts with the two model proteins. The metal complex releases tfa ligands slower than *cis*-[Rh<sub>2</sub>(OAc)<sub>2</sub>(tfa)<sub>2</sub>] in solution; the presence of the proteins accelerates the process. The structure of the [Rh<sub>2</sub>(OAc)(tfa)<sub>3</sub>] adduct with HEWL shows that the metal compound degrades upon interaction with the protein, as observed in the case of [Rh<sub>2</sub>(OAc)<sub>4</sub>] and *cis*-[Rh<sub>2</sub>(OAc)<sub>2</sub>(tfa)<sub>2</sub>]. Rh fragments are observed close to His15, Lys33, Asp101 and C-terminal tail. In the structure of [Rh<sub>2</sub>(OAc)(tfa)<sub>3</sub>]/RNase A adduct dirhodium fragments are observed close to His105 and His119, as in the structures of the [Rh<sub>2</sub>(OAc)<sub>4</sub>]/RNase A and *cis*-[Rh<sub>2</sub>(OAc)<sub>2</sub>(tfa)<sub>2</sub>]/RNase A adducts.<sup>81</sup> However, dirhodium unit from [Rh<sub>2</sub>(OAc)(tfa)<sub>3</sub>] binds His imidazole rings both at axial and equatorial binding sites, in contrast to what was found in the case of [Rh<sub>2</sub>(OAc)<sub>4</sub>] and *cis*-[Rh<sub>2</sub>(OAc)<sub>2</sub>(tfa)<sub>2</sub>].

These results demonstrate that equatorial ligands strongly influence the reactivity of the dirhodium paddlewheel complexes towards proteins; thus, desired binding sites could be obtained by tuning these ligands.

Overall, these data demonstrate that the interaction of dirhodium tetracarboxylates with HEWL leads to a degradation of the metal complexes, while the interaction with RNase A produces metal/protein adducts that preserves the dimetallic core.

Since the interaction between  $[\text{Rh}_2(\text{OAc})_4]$  and RNase A leaves the metal compound unperturbed,<sup>81</sup> its reactivity toward imidazole and glycine as a model ligand was investigated in the solid state.

Surprisingly, imidazole binds the dirhodium tetraacetate at equatorial rather than axial position. Three acetate ligands are replaced by six water molecules. DFT studies clarified that this unexpected reactivity is triggered upon hydrolysis of the dirhodium core, once that the metal compound is axially bound to a first molecule of imidazole (provided by His residues). Electronic structure analysis reveals that the Rh atom that is coordinated to the protein acts as a better Lewis acid than the other Rh atom. Glycine also binds the equatorial position.

From these data, it emerges that the dirhodium centre in the adduct with RNase A, in the solid state, retains a certain degree of reactivity with small molecules. Thus, crystals of the  $[\text{Rh}_2(\text{OAc})_4]$ /RNase A adduct are ideal candidates for preparing CLPCs functionalised with the dirhodium compound. Unfortunately, the preparation of crystals of the adduct into C2 space group requires a long time (about 3 weeks). Hence, new crystals of dirhodium/RNase A were prepared in a different space group (P3<sub>2</sub>21), that allows the protein crystal growth and functionalization with  $[\text{Rh}_2(\text{OAc})_4]$  in shorter times (26 h). X-ray structures of the  $[\text{Rh}_2(\text{OAc})_4]$ /RNase A adduct collected over time reveal that the protein is extensively metalated within 2 h of soaking with the metal compound. It is unperturbed upon protein binding and axially coordinated to His105 and His119 side chains, as observed for the metal/protein adduct crystals obtained in the C2 space group.<sup>81</sup>

A cross-linking protocol for preparing CL\_RNase A crystals using GA was then developed, using the gentle diffusion technique. CL\_RNase A crystals were soaked with  $[\text{Rh}_2(\text{OAc})_4]$  and analysed by X-ray crystallography at two different temperatures (-173 and 0 °C). The results reveal that the protein can be still metalated upon cross-linking, but the occupancy of the dirhodium centre close to His119 side chain is decreased when compared to untreated crystals.

The reactivity of CL\_Rh/RNase A crystals as a catalyst towards olefine cyclopropanation and self-coupling of diazo compounds reactions was investigated using styrene and ethyl diazoacetate as model reagents. The results revealed that the CLPCs catalyse both the reactions. While several by-products

are observed upon ethyl diazoacetate self-coupling reaction, the styrene cyclopropanation occurs producing the ethyl-phenylcyclopropane-1-carboxylate with high selectivity.

In conclusion, results collected in this Ph.D. thesis provide insightful information about the reactivity of dirhodium paddlewheel complexes with proteins and the reactivity of the metal/protein adducts formed upon reaction of dirhodium tetraacetate with RNase A in the solid state. Overall, these data could help the prediction of potential dirhodium binding sites in proteins and provide useful insights into the Rh compound/protein recognition process, opening new perspectives in the synthesis of Rh-based artificial enzymes and in the preparation of CLPCs functionalized with dirhodium compounds.

## CONCLUSIONS

## 7. APPENDIX

## 7.1. Data collection and refinement statistics

**Table A.** Data collection and refinement statistics of the [Rh<sub>2</sub>(OAc)<sub>4</sub>]/HEWL adduct structures.

	Crystal 1	Crystal 2	Crystal 3	Crystal 4	Crystal 5	Crystal 6
Procedure	Cocrystallization	Cocrystallization	Cocrystallization	Cocrystallization	Soaking	Soaking
Soaking procedure	-				Soaking with a saturated solution of [Rh <sub>2</sub> (OAc) <sub>4</sub> ]	Soaking with a saturated solution of [Rh <sub>2</sub> (OAc) <sub>4</sub> ]
Soaking time	-				1 year	7 days
Crystallization condition	20% ethylene glycol, 0.100 M sodium acetate at pH 4.5 and 0.6 M sodium nitrate					10 mM HEPES pH 7.5 and 2.00 M sodium formate
Data collection Temperature (K)	100					
<i>Data collection</i>						
Space group	P4 <sub>3</sub> 2 <sub>1</sub> 2	P4 <sub>3</sub> 2 <sub>1</sub> 2	P4 <sub>3</sub> 2 <sub>1</sub> 2	P4 <sub>3</sub> 2 <sub>1</sub> 2	P4 <sub>3</sub> 2 <sub>1</sub> 2	P4 <sub>3</sub> 2 <sub>1</sub> 2
a=b (Å)	77.964	77.948	78.360	78.604	78.007	78.930
c (Å)	37.291	37.380	37.610	37.307	37.245	37.120
Resolution range (Å)	25.48-1.94 (1.97-1.94)	26.99-1.62 (1.65-1.62)	78.36-1.40 (1.47-1.40)	55.58-1.32 (1.37-1.32)	35.19-1.74 (1.83-1.74)	55.81-1.65 (1.80-1.65)
Unique reflections	8895 (426)	15018 (623)	22922 (3274)	26513 (1327)	11348 (567)	11800 (591)
Completeness (%)	99.0 (97.1)	98.7 (86.6)	100 (100)	95.4 (51.1)	91.1 (36.0)	94.0 (52.6)

## APPENDIX

Redundancy	5.3 (3.7)	9.0 (1.9)	19.6 (16.6)	25.8 (25.9)	25.0 (27.6)	24.5 (22.4)
†Rmerge (%)	0.095 (0.440)	0.068 (0.190)	0.099 (2.00)	0.047 (2.55)	0.070 (3.12)	0.120 (3.23)
Rpim	0.045 (0.249)	0.021 (0.152)	0.023 (0.519)	0.013 (0.720)	0.020 (0.848)	0.025 (0.680)
Average I/σ(I)	14.9 (2.2)	56.7 (3.4)	10.2 (1.0)	28.8 (1.1)	24.7 (1.1)	22.5 (1.3)
CC <sub>1/2</sub>	0.997 (0.808)	0.999 (0.942)	0.999 (0.701)	1.00 (0.612)	1.00 (0.474)	1.00 (0.51)
Anomalous Completeness (%)	99.1 (94.1)	96.8 (67.3)	100 (100)	95.3 (52.1)	90.8 (36.6)	93.8 (51.4)
Anom. Redundancy	2.9 (2.0)	5.0 (1.3)	10.3 (8.5)	13.8 (13.4)	13.7 (14.5)	13.4 (12.0)
<i>Refinement</i>						
Resolution range (Å)	25.48-1.94	26.99-1.62	55.41-1.40	55.58-1.32	35.19-1.74	55.81-1.65
N. of reflections (working set)	8445	14241	22453	25227	10794	11205
N. of reflections (test set)	430	736	1212	1286	555	595
R-factor/R-free (%)	15.6/21.7	16.4/20.2	19.0/20.9	17.7/22.3	18.5/22.8	18.1/23.4
N. of atoms	1221	1231	1283	1275	1129	1139
Average B-factors (Å <sup>2</sup> )						
All atoms	21.1	21.4	16.8	27.3	42.9	30.6
Rh occupancy	0.70/0.35/0.40/ 0.40	0.65/0.50/0.20/ 0.20	0.65/0.30	0.70/0.30	0.25/0.40/ 0.20	0.40/0.45/0.35/0.20/ 0.30/0.30/0.40
Rh atoms	31.7/33.7/67.9/ 75.3	30.8/46.9/39.3/ 42.5	23.1/26.7	35.5/41.7	81.1/73.9/ 65.2	59.6/69.0/66.9/49.3/ 68.7/57.4/79.8
R.m.s. deviations						
Bond lengths (Å)	0.009	0.013	0.013	0.013	0.008	0.008
Bond angles (°)	2.38	1.96	1.87	2.39	1.55	1.55

Ramachandran statistics (Coot analysis)						
N. of residues in Allowed/Disallowed regions	4/0	4/0	3/0	3/0	4/0	3/0

† $R_{\text{merge}} = \frac{\sum_h \sum_i |I(h,i) - \langle I(h) \rangle|}{\sum_h \sum_i I(h,i)}$ , where  $I(h,i)$  is the intensity of the  $i^{\text{th}}$  measurement of reflection  $h$  and  $\langle I(h) \rangle$  is the mean value of the intensity of reflection  $h$ .

**Table B.** Data collection and refinement statistics of the *cis*-[Rh<sub>2</sub>(OAc)<sub>2</sub>(tfa)<sub>2</sub>]/RNase A and *cis*-[Rh<sub>2</sub>(OAc)<sub>2</sub>(tfa)<sub>2</sub>]/HEWL adduct structures.

Protein	RNase A	RNase A	RNase A	RNase A	HEWL
	Structure 1	Structure 2	Structure 3	Structure 4	
Soaking procedure	Soaking with a saturated solution of <i>cis</i> -[Rh <sub>2</sub> (OAc) <sub>2</sub> (tfa) <sub>2</sub> ]	Soaking with a 5 mM solution of <i>cis</i> -[Rh <sub>2</sub> (OAc) <sub>2</sub> (tfa) <sub>2</sub> ]	Soaking with a 8 mM solution of <i>cis</i> -[Rh <sub>2</sub> (OAc) <sub>2</sub> (tfa) <sub>2</sub> ]	Soaking with a saturated solution of <i>cis</i> -[Rh <sub>2</sub> (OAc) <sub>2</sub> (tfa) <sub>2</sub> ]	Soaking with a 5 mM solution of <i>cis</i> -[Rh <sub>2</sub> (OAc) <sub>2</sub> (tfa) <sub>2</sub> ]
Soaking time	3 days	4 days	3 days	3 days	4 days
Crystallization conditions	22% PEG 4K, 10 mM sodium citrate at pH 5.1				10 mM HEPES pH 7.5 and 2.000 M sodium formate
Data collection Temperature (K)	100				
<i>Data collection</i>					
Space group	C2	C2	C2	C2	P4 <sub>3</sub> 2 <sub>1</sub> 2
a (Å)	100.35	100.21	100.39	101.18	77.59
b (Å)	32.87	32.57	32.54	32.95	77.59
c (Å)	72.97	72.61	72.51	73.28	37.94
Resolution range (Å)	73.06-1.15 (1.15-1.17)	41.14-1.32 (1.35-1.32)	50.11-1.42 (1.44-1.42)	50.86-1.45 (1.48-1.45)	54.86-1.48 (1.50-1.48)
Unique reflections	84723 (4212)	49880 (2752)	44454 (2037)	43428 (2151)	19342 (918)
Completeness (%)	99.6 (100.0)	99.5 (100.0)	99.1 (92.8)	99.9 (100.0)	96.3 (93.0)

## APPENDIX

Redundancy	6.1 (5.4)	5.5 (5.8)	6.0 (4.4)	5.2 (5.6)	23.3 (24.9)
Rmerge (%)	0.078 (0.699)	0.138 (0.862)	0.076 (0.523)	0.185 (0.796)	0.058 (1.33)
Rpim	0.051 (0.479)	0.100 (0.570)	0.050 (0.406)	0.135 (0.557)	0.017 (0.380)
Average I/ $\sigma$ (I)	10.3 (2.2)	10.8 (2.2)	12.7 (2.3)	11.8 (3.1)	29.2 (2.7)
CC <sub>1/2</sub>	0.997 (0.738)	0.996 (0.704)	0.996 (0.790)	0.988 (0.670)	0.999 (0.950)
Anom. completeness (%)	98.6 (97.2)	98.3 (96.3)	98.8 (91.1)	97.9 (99.4)	97.1 (93.3)
Anom. Redundancy	3.1 (2.8)	2.8 (3.0)	3.1 (2.3)	2.7 (2.9)	12.7 (13.1)
<i>Refinement</i>					
Asymmetric unit content	Two protein molecules	Two protein molecules	Two protein molecules	Two protein molecules	One protein molecule
Resolution range (Å)	73.06-1.15	41.14-1.32	50.11-1.42	50.86-1.45	39.05-1.47
N. of reflections (working set)	80792	52632	41857	40445	18518
N. of reflections (test set)	5840	3855	2955	2936	1225
R-factor/R-free (%)	13.6/16.6	16.4/21.3	17.7/21.2	16.2/20.2	18.6/22.4
N. of atoms	2598	2449	2355	2499	1250
Average B-factors (Å <sup>2</sup> )					
All atoms	18.1	17.3	20.7	16.1	21.4
Rh occupancy	0.55/0.20/0.20/ 0.40	0.40/0.40/0.40	0.80/0.30/0.30/ 0.70/0.40	0.75/0.30/0.30/ 0.55	0.50/0.50/0.30
Rh atoms	15.7/22.4/19.0/ 20.5/17.0/21.3/ 20.0/29.6	19.0/24.7/22.3 28.2/26.3/36.8	17.7/22.5/16.5/ 19.7/17.7/21.2/ 21.5/38.8/ 17.7/22.5	11.8/16.7/13.0/ 16.7/13.7/18.5/ 13.5/21.3	54.4/73.5/59.8
R.m.s. deviations					

## APPENDIX

Bond lengths (Å)	0.17	0.013	0.013	0.013	0.012
Bond angles (°)	3.40	3.13	3.69	2.80	1.92
Ramachandran statistics (Coot analysis)					
N. of residues in Allowed/Disallowed regions	6/2	7/0	6/1	6/2	4/0

**Table C.** Data collection and refinement statistics of the  $[\text{Rh}_2(\text{OAc})(\text{tfa})_3]/\text{RNase A}$  and  $[\text{Rh}_2(\text{OAc})(\text{tfa})_3]/\text{HEWL}$  adduct structures.

Protein	RNase A	RNase A	HEWL
	Adduct 1	Adduct 2	
Soaking procedure	Soaking with a 5 mM solution of $[\text{Rh}_2(\text{OAc})(\text{tfa})_3]$	Soaking with a 5 mM solution of $[\text{Rh}_2(\text{OAc})(\text{tfa})_3]$	Soaking with a 5 mM solution of $[\text{Rh}_2(\text{OAc})(\text{tfa})_3]$
Soaking time	4 days		
Crystallization conditions	22% PEG 4K, 10 mM sodium citrate at pH 5.1		10 mM HEPES pH 7.5 and 2.000 M sodium formate
Data collection Temperature (K)	100		
<i>Data collection</i>			
Space group	C2	C2	$P4_32_12$
a (Å)	101.18	100.12	78.55
b (Å)	32.95	32.41	78.59
c (Å)	73.28	72.27	37.39
Resolution range (Å)	50.85-1.45 (1.48-1.45)	30.99-1.71 (1.74-1.71)	39.31-1.53 (1.56-1.53)
Unique reflections	43428 (2151)	25642 (1242)	18041 (899)
Completeness (%)	99.0 (100.0)	99.9 (100.0)	98.8 (100.0)
Redundancy	5.2 (5.6)	6.3 (6.2)	23.3 (25.1)
Rmerge (%)	0.185 (0.796)	0.079 (0.795)	0.052 (1.749)
Rpim	0.135 (0.557)	0.052 (0.521)	0.015 (0.500)

Average I/ $\sigma$ (I)	11.8 (3.1)	12.5 (2.2)	32.1 (2.1)
CC <sub>1/2</sub>	0.998 (0.670)	0.997 (0.782)	1.000 (0.752)
Anom. completeness (%)	97.9 (99.4)	99.5 (99.7)	98.9 (100.0)
Anom. Redundancy	2.7 (2.9)	3.3 (3.2)	12.6 (13.2)
<i>Refinement</i>			
Asymmetric unit content	Two protein molecules	Two protein molecules	One protein molecule
Resolution range (Å)	50.85-1.45	30.99-1.71	39.31-1.53
N. of reflections (working set)	41357	24495	17071
N. of reflections (test set)	3054	1755	1218
R-factor/R-free (%)	20.1/23.2	18.3/23.6	19.5/24.8
N. of atoms	2365	2207	1240
Average B-factors (Å <sup>2</sup> )			
All atoms	19.1	26.9	27.3
Rh occupancy	0.50/0.50/0.40/ 0.40/0.20/0.20/ 0.40/0.40	0.70/0.70/0.55/ 0.55/0.30/0.30/ 0.55/0.55	0.25/0.25/0.30/ 0.25/0.30
Rh atoms	30.7/38.9/36.4/ 44.2/22.9/25.2/ 26.9/28.1	35.7/57.0/52.1/ 68.0/34.2/41.1/ 45.2/56.1	61.2/59.8/58.7/ 54.7/47.9
R.m.s. deviations			
Bond lengths (Å)	0.013	0.011	0.010
Bond angles (°)	1.83	2.22	1.74
Ramachandran statistics (Coot analysis)			

APPENDIX

N. of residues in Allowed/Disallowed regions	9/3	7/4	6/0
--	-----	-----	-----

**Table D.** Data collection and refinement statistics of the  $[\text{Rh}_2(\text{OAc})_4]/\text{RNase A}$  adduct upon reaction with imidazole.

Soaking procedure	Soaking with a saturated solution of imidazole
Soaking time	44 days
Data collection Temperature (K)	100
<i>Data collection</i>	
Space group	C2
a (Å)	100.49
b (Å)	32.53
c (Å)	72.19
$\beta$ (°)	90.29
Resolution range (Å)	50.3-1.40 (1.43-1.40)
Unique reflections	43550
Observations	280144
Completeness (%)	94.3 (92.5)
Redundancy	6.4 (6.8)
R <sub>meas</sub> (%)	0.058 (1.079)
Average I/ $\sigma$ (I)	15.4 (2.2)
CC <sub>1/2</sub>	1.0 (0.8)
Anomalous completeness	94.7

Anomalous redundancy	3.3
<i>Refinement</i>	
Asymmetric unit content	Two protein molecules
Resolution range (Å)	50.30-1.40
N. of reflections	41609
<i>R</i> -factor/ <i>R</i> -free (%)	18.9/23.1
N. of atoms	2323
Average B-factors (Å <sup>2</sup> )	
All atoms	24.9
Rh occupancy	0.80/0.80/0.70/ 0.70/0.55/0.55/ 0.50/0.50/0.50/ 0.50
Rh atoms	24.8/30.5/25.0/ 37.4/20.0/25.0/ 25.4/23.1/20.6/ 53.3
R.m.s. deviations	
Bond lengths (Å)	0.014
Bond angles (°)	3.95
Ramachandran statistics (Coot analysis)	
N. of residues in Allowed/Disallowed regions	9/1

**Table E.** Data collection and refinement statistics of the  $[\text{Rh}_2(\text{OAc})_4]/\text{RNase A}$  adduct upon reaction with glycine.

Soaking procedure	Soaking with a saturated solution of glycine
Soaking time	44 days
Data collection Temperature (K)	100
<i>Data collection</i>	
Space group	C2
a (Å)	101.31
b (Å)	32.83
c (Å)	72.94
$\beta$ (°)	90.71
Resolution range (Å)	73.1-1.42 (1.45-1.42)
Unique reflections	45025
Observations	269705
Completeness (%)	98.8 (97.1)
Redundancy	5.9 (4.7)
R <sub>meas</sub> (%)	0.130 (1.126)
Average I/ $\sigma$ (I)	9.5 (1.9)
CC <sub>1/2</sub>	1.0 (0.8)
Anomalous completeness	98.1
Anomalous redundancy	3.1

<i>Refinement</i>	
Asymmetric unit content	Two protein molecules
Resolution range (Å)	73.1-1.42
N. of reflections	43025
<i>R</i> -factor/ <i>R</i> -free (%)	20.3/26.0
N. of atoms	2286
Average B-factors (Å <sup>2</sup> )	
All atoms	19.6
Rh occupancy	0.70/0.70/0.70/ 0.70/0.50/0.50/ 0.45/0.45
Rh atoms	26.2/39.4/21.7/ 27.5/27.9/38.8/ 22.3-28.1
R.m.s. deviations	
Bond lengths (Å)	0.010
Bond angles (°)	3.03
Ramachandran statistics (Coot analysis)	
N. of residues in Allowed/Disallowed regions	11/3

**Table F.** Data collection and refinement statistics of the  $[\text{Rh}_2(\text{OAc})_4]/\text{RNase A}$  adduct from crystals in the  $\text{P3}_221$  space group collected upon different soaking times.

Protein	RNase A	RNase A	RNase A
	Crystal 1 h	Crystal 2 h	Crystal 6 h
Soaking procedure	Soaking with a saturated solution of $[\text{Rh}_2(\text{OAc})_4]$	Soaking with a saturated solution of $[\text{Rh}_2(\text{OAc})_4]$	Soaking with a saturated solution of $[\text{Rh}_2(\text{OAc})_4]$
Soaking time	1 h	2 h	6 h
Data collection Temperature (K)	100		
<i>Data collection</i>			
Space group	$\text{P3}_221$	$\text{P3}_221$	$\text{P3}_221$
a = b (Å)	67.13	67.14	66.79
c (Å)	64.98	64.79	64.90
$\beta$ (°)	90.00	90.00	90.00
$\gamma$ (°)	120.00	120.00	120.00
Resolution range (Å)	21.97-1.50 (1.53-1.50)	21.98-1.54 (1.56-1.54)	21.86-1.50 (1.53-1.50)
Unique reflections	27554 (1345)	25583 (1242)	27269 (1349)
Completeness (%)	100.0 (100.0)	100.0 (99.8)	100.0 (99.8)
Redundancy	11.1 (6.8)	4.1 (2.6)	8.5 (5.1)
Rmerge (%)	0.074 (2.144)	0.077 (2.388)	0.079 (2.022)
Rpim	0.022 (0.875)	0.041 (1.763)	0.028 (0.975)
Average $I/\sigma(I)$	22.6 (0.9)	12.3 (0.4)	20.0 (0.8)
$\text{CC}_{1/2}$	0.999 (0.325)	0.998 (0.087)	0.999 (0.223)

Anom. completeness (%)	99.8 (98.7)	89.3 (81.6)	99.8 (97.3)
Anom. Redundancy	5.6 (3.4)	1.9 (1.4)	4.2 (2.6)
<i>Refinement</i>			
Asymmetric unit content	One protein molecule	One protein molecule	One protein molecule
Resolution range (Å)	21.98-1.50	21.65-1.54	21.60-1.50
N. of reflections	26141	24258	25873
<i>R</i> -factor/ <i>R</i> -free (%)	18.0/21.8	19.6/22.2	17.8/21.5
N. of atoms	1290	1271	1253
Average B-factors (Å <sup>2</sup> )			
All atoms	20.1	22.0	18.8
Rh occupancy	0.75/0.75 0.50/0.50	0.70/0.70 0.50/0.50	0.78/0.78 0.55/0.55
Rh atoms	14.2/15.5 23.9/28.3	16.4/17.8 21.1/37.3	12.6/13.9 24.1/29.5
R.m.s. deviations			
Bond lengths (Å)	0.010	0.008	0.010
Bond angles (°)	1.71	1.48	1.70
Ramachandran statistics (Coot analysis)			
N. of residues in Allowed/Disallowed regions	0/0	2/0	1/2

**Table G.** Data collection (100 and 273 K) and refinement statistics of the  $[\text{Rh}_2(\text{OAc})_4]$ /RNase A adduct from CL\_crystals in the  $P3_221$  space group collected upon 24 h soaking.

Protein	RNase A	RNase A
Soaking procedure	Soaking with a saturated solution of $[\text{Rh}_2(\text{OAc})_4]$	Soaking with a saturated solution of $[\text{Rh}_2(\text{OAc})_4]$
Soaking time	24 h	24 h
Data collection Temperature (K)	100	273
<i>Data collection</i>		
Space group	$P3_221$	$P3_221$
a = b (Å)	67.39	67.28
c (Å)	64.42	65.90
$\beta$ (°)	90.00	90.00
$\gamma$ (°)	120.00	120.00
Resolution range (Å)	22.06-1.50 (1.53-1.50)	22.02-1.60 (1.63-1.60)
Unique reflections	27241 (1303)	23142 (1111)
Completeness (%)	99.3 (97.6)	99.9 (99.2)
Redundancy	1.9 (1.8)	1.8 (1.8)
Rmerge (%)	0.056 (1.296)	0.079 (1.062)
Rpim	0.056 (1.296)	0.079 (1.062)
Average I/ $\sigma$ (I)	17.4 (0.6)	6.9 (0.6)
$\text{CC}_{1/2}$	0.998 (0.199)	0.994 (0.339)

## APPENDIX

Anom. completeness (%)	90.5 (86.3)	89.3 (81.6)
Anom. Redundancy	1.0 (1.0)	0.9 (1.0)
<i>Refinement</i>		
Asymmetric unit content	One protein molecule	One protein molecule
Resolution range (Å)	22.06 -1.50	22.02-1.60
N. of reflections	25847	21978
<i>R</i> -factor/ <i>R</i> -free (%)	18.3/22.3	18.1/19.8
N. of atoms	1331	1207
Average B-factors (Å <sup>2</sup> )		
All atoms	19.5	21.2
Rh occupancy	0.75/0.75 0.35/0.35	0.80/0.80 0.35/0.35
Rh atoms	15.4/17.0 51.6/59.0	13.5/15.7 46.3/50.6
R.m.s. deviations		
Bond lengths (Å)	0.009	0.009
Bond angles (°)	1.55	1.55
Ramachandran statistics (Coot analysis)		
N. of residues in Allowed/Disallowed regions	1/0	1/2



## 8. PUBLICATIONS

Some experiments and data here reported were published on peer reviewed international journals.

Loreto, D.; Ferraro, G.; Merlino, A. Unusual Structural Features in the Adduct of Dirhodium Tetraacetate with Lysozyme. *International Journal of Molecular Sciences* **2021**, *22* (3), 1496.

Loreto, D.; Merlino, A. The Interaction of Rhodium Compounds with Proteins: A Structural Overview. *Coordination Chemistry Reviews* **2021**, *442*, 213999.

Loreto, D.; Esposito, A.; Demitri, N.; Guaragna, A.; Merlino, A. Reactivity of a Fluorine-Containing Dirhodium Tetracarboxylate Compound with Proteins. *Dalton Trans.* **2022**, *51* (9), 3695–3705.

Loreto, D.; Esposito, A.; Demitri, N.; Guaragna, A.; Merlino, A. Digging into Protein Metalation Differences Triggered by Fluorine Containing-Dirhodium Tetracarboxylate Analogues. *Dalton Trans.* **2022**, *51* (18), 7294–7304.

Loreto, D.; Fasulo, F.; Muñoz-García, A. B.; Pavone, M.; Merlino, A. Unexpected Imidazole Coordination to the Dirhodium Center in a Protein Environment: Insights from X-Ray Crystallography and Quantum Chemistry. *Inorg. Chem.* **2022**, *61* (22), 8402–8405.

## REFERENCES

**9. REFERENCES**

- (1) Bertrand, J. A.; Cotton, F. A.; Dollase, W. A. The Metal-Metal Bonded, Polynuclear Complex Anion in CsReCl<sub>4</sub>. *J. Am. Chem. Soc.* **1963**, *85* (9), 1349-1350. ACS Publications.
- (2) Nair A. K.; Harisomayajula S.; Tsai Yi-C. Theory, synthesis and reactivity of quintuple bonded complexes. *Dalton Trans.* **2014**, 43, 5618-5638.
- (3) Cotton, F. A.; Murillo, C. A.; Walton, R. A. Introduction and Survey. In *Multiple Bonds Between Metal Atoms*; Eds.; Springer US: Boston, MA, 2005; 1–21.
- (4) Norman, J. G. Jr.; Renzoni, G. E.; Case, D. A. Electronic structure of Ru<sub>2</sub>(O<sub>2</sub>CR)<sup>4+</sup> and Rh<sub>2</sub>(O<sub>2</sub>CR)<sup>4+</sup> complexes. *J. Am. Chem. Soc.* **1979**, *101* (18), 5256-5257.
- (5) Cotton, F. A. Centenary Lecture. Quadruple Bonds and Other Multiple Metal to Metal Bonds. *Chem. Soc. Rev.* **1975**, *4* (1), 27–53.
- (6) Porai-Koshits M. A.; Antsyshkina A. S. The structure of rhodium acetate complexes. *Dokl. Akad. Nauk SSSR* **1962**, *146* (5), 1102–1105.
- (7) Prater, M. E.; Pence, L. E.; Clérac, R.; Finnis, G. M.; Campana, C.; Auban-Senzier, P.; Jérôme, D.; Canadell, E.; Dunbar, K. R. A Remarkable Family of Rhodium Acetonitrile Compounds Spanning Three Oxidation States and with Nuclearities Ranging from Mononuclear and Dinuclear to One-Dimensional Chains. *J. Am. Chem. Soc.* **1999**, *121* (35), 8005–8016.
- (8) Hrdina, R. Dirhodium(II,II) Paddlewheel Complexes. *European Journal of Inorganic Chemistry* **2021**, *6*, 501–528.
- (9) Chifotides, H. T.; Dunbar, K. R. Rhodium Compounds. In *Multiple Bonds Between Metal Atoms*; Cotton, F. A., Murillo, C. A., Walton, R. A., Eds.; Springer US: Boston, MA, 2005; 465–589.
- (10) Cotton, F. A.; Hillard, E. A.; Murillo, C. A. The First Dirhodium Tetracarboxylate Molecule without Axial Ligation: New Insight into the Electronic Structures of Molecules with Importance in Catalysis and Other Reactions. *J. Am. Chem. Soc.* **2002**, *124* (20), 5658–5660.
- (11) Cotton, F. A.; Felthouse, T. R. Seven Dinuclear Rhodium(II) Complexes

- with o-Oxypyridine Anions as Ligands. *Inorg. Chem.* **1981**, *20* (2), 584–600.
- (12) Boyar, E. B.; Robinson, S. D. Rhodium(II) Carboxylates. *Coordination Chemistry Reviews* **1983**, *50* (1), 109–208.
- (13) Cotton, F. A.; DeBoer, B. G.; Laprade, M. D.; Pipal, J. R.; Ucko, D. A. Multiple chromium(II)-chromium(II) and rhodium(II)-rhodium(II) bonds. *J. Am. Chem. Soc.* **1970**, *92* (9), 2926-2927.
- (14) Christoph, G. G.; Koh, Y. B. Metal-metal bonding in dirhodium tetracarboxylates. Trans influence and dependence of the rhodium-rhodium bond distance upon the nature of the axial ligands. *J. Am. Chem. Soc.* **1979**, *101* (6), 1422-1434.
- (15) Nomran, J. G. Jr.; Kolari, H. J. Strength and trans influence of the rhodium-rhodium bond in rhodium(II) carboxylate dimers. *J. Am. Chem. Soc.* **1978**, *100* (3), 791-799.
- (16) Trexler J. W. Jr.; Schreiner, A. F.; Cotton, F. A. Electronic excitation MO assignment of rhodium carboxylato complexes,  $\text{Rh}_2(\text{O}_2\text{CR})_4(\text{L}_{\text{ax}})_2$ , using MCD experiment and theory. *Inorg. Chem.* **1988**, *27* (19), 3265-3267.
- (17) Warzecha, E.; Berto, T. C.; Wilkinson, C. C.; Berry, J. F. Rhodium Rainbow: A Colorful Laboratory Experiment Highlighting Ligand Field Effects of Dirhodium Tetraacetate. *J. Chem. Educ.* **2019**, *96* (3), 571–576.
- (18) Ezerskaya, N. A.; Toropchenova, E. S.; Kubrakova, I. V.; Krasheninnikova, S. V.; Kudinova, T. F.; Fomina, T. A.; Kiseleva, I. N. Preparation of Binuclear Rhodium(II) Tetraacetate (Initial Compound for the Coulometric Determination of Rhodium) under the Action of Microwave Radiation. *J. Anal. Chem.* **2000**, *55* (12), 1132-1135.
- (19) Kataoka, Y.; Yano, N.; Kawamoto, T.; Handa, M.; Isolation of a Tetranuclear Intermediate Complex in the Synthesis of Paddlewheel-Type Dirhodium Tetraacetate. *Eur. J. Inorg. Chem.* **2015**, *34*, 5650-5655.
- (20) Callot, H. J.; Albrecht-Gary, A. M.; Al Joubbeh, M.; Metz, B.; Metz, F. Crystallographic Study and Ligand Substitution Reactions of Dirhodium(II) Tris- and Tetrakis(Tritolylbenzoate). *Inorg. Chem.* **1989**, *28* (19), 3633–3640.
- (21) Cotton, F. A.; Thompson, J. L. Preparation and Structural

Characterization of Three Tetracarboxylato Dirhodium (Rh-Rh) Compounds with Bulky Ligands. *Inorg. Chim. Acta* **1984**, *81*, 193–203.

(22) Roos, G. H. P.; McKervey, M. A. A Facile Synthesis of Homochiral Rh(II) Carboxylates. *Synthetic Communications* **1992**, *22* (12), 1751–1756.

(23) Vohidov, F.; Knudsen, S. E.; Leonard, P. G.; Ohata, J.; Wheadon, M. J.; Popp, B. V.; Ladbury, J. E.; Ball, Z. T. Potent and Selective Inhibition of SH<sub>3</sub> Domains with Dirhodium Metalloinhibitors. *Chem. Sci.* **2015**, *6* (8), 4778–4783.

(24) Cotton, F. A.; Dikarev, E. V.; Petrukhina, M. A. Coordinated and Clathrated Molecular Diiodine in [Rh<sub>2</sub>(O<sub>2</sub>CCF<sub>3</sub>)<sub>4</sub>I<sub>2</sub>] $\cdot$ I<sub>2</sub>. *Angewandte Chemie International Edition* **2000**, *39* (13), 2362–2364.

(25) Dikarev, E. V.; Goroff, N. S.; Petrukhina, M. A. Expanding the Scope of Solvent-Free Synthesis: Entrapment of Thermally Unstable Species. *Journal of Organometallic Chemistry* **2003**, *683* (2), 337–340.

(26) Cotton, F. A.; Felthouse, T. R. Ambidentate Character of Dimethyl Sulfoxide in Adducts of Tetrakis(Propionato)- and Tetrakis(Trifluoroacetato)Dirhodium(II). *Inorg. Chem.* **1980**, *19* (8), 2347–2351.

(27) Maspero, F.; Taube, H. The Aquorhodium(II) Ion. *J. Am. Chem. Soc.* **1968**, *90* (26), 7361–7363.

(28) Dunbar, K. R. Spectroscopic and Structural Investigation of the Unbridged Dirhodium Cation [Rh<sub>2</sub>(CH<sub>3</sub>CN)<sub>10</sub>]<sup>4+</sup>. *J. Am. Chem. Soc.* **1988**, *110* (24), 8247–8249.

(29) Feng, M.; Chan, K. S. Synthesis and Reactivity of the Non-Bridged Metal–Metal Bonded Rhodium Octamethoxyporphyrin Dimer. *Journal of Organometallic Chemistry* **1999**, *584* (2), 235–239.

(30) Sizova, O. V. The Valence Structure Analysis for Dirhodium(II) Tetracarboxylato Complexes with Nitric Oxide as Axial Ligand. *J. Mol. Struct.: THEOCHEM* **2006**, *760* (1), 183–187.

(31) Uemura, S.; Spencer, A.; Wilkinson, G. M<sup>3</sup>-Oxotrimetal Acetato-Complexes of Chromium, Manganese, Iron, Cobalt, Rhodium, and Iridium. *Dalton Trans.* **1973**, No. 23, 2565–2571.

(32) Nomran, J. G. Jr.; O. Fey, E. Reactions of Tetra-Acetatodirhodium( II )

with Arenesulphinates. *Dalton Transactions* **1976**, 0 (9), 765–767.

(33) Collins, L. R.; van Gastel, M.; Neese, F.; Fürstner, A. Enhanced Electrophilicity of Heterobimetallic Bi–Rh Paddlewheel Carbene Complexes: A Combined Experimental, Spectroscopic, and Computational Study. *J. Am. Chem. Soc.* **2018**, *140* (40), 13042–13055.

(34) Cotton, F. A.; Lin, C.; Murillo, C. A. Supramolecular Structures Based on Dimetal Units: Simultaneous Utilization of Equatorial and Axial Connections. *Chem. Commun.* **2001**, *1*, 11–12.

(35) Cotton, F. A.; Lin, C.; Murillo, C. A. Supramolecular Arrays Based on Dimetal Building Units. *Acc. Chem. Res.* **2001**, *34* (10), 759–771.

(36) Schiavo, S. L.; Piraino, P.; Bonavita, A.; Micali, G.; Rizzo, G.; Neri, G. A Dirhodium(II,II) Molecular Species as a Candidate Material for Resistive Carbon Monoxide Gas Sensors. *Sensors and Actuators B: Chemical* **2008**, *129* (2), 772–778.

(37) Schiavo, S. L.; Cardiano, P.; Donato, N.; Latino, M.; Neri, G. A Dirhodium(II,II) Complex as a Highly Selective Molecular Material for Ammonia Detection: QCM Studies. *J. Materials Chem.* **2011**, *21* (44), 18034–18041.

(38) Hilderbrand, S. A.; Lim, M. H.; Lippard, S. J. Dirhodium Tetracarboxylate Scaffolds as Reversible Fluorescence-Based Nitric Oxide Sensors. *J. Am. Chem. Soc.* **2004**, *126* (15), 4972–4978.

(39) Burgos, A. E.; Belchior, J. C.; Sinisterra, R. D. Controlled Release of Rhodium (II) Carboxylates and Their Association Complexes with Cyclodextrins from Hydroxyapatite Matrix. *Biomaterials* **2002**, *23* (12), 2519–2526.

(40) Chifotides, H. T.; Fu, P. K.-L.; Dunbar, K. R.; Turro, C. Effect of Equatorial Ligands of Dirhodium(II,II) Complexes on the Efficiency and Mechanism of Transcription Inhibition in Vitro. *Inorg. Chem.* **2004**, *43* (3), 1175–1183.

(41) Aoki, K.; Salam, Md. A. Interligand Interactions Affecting Specific Metal Bonding to Nucleic Acid Bases: The Tetrakis( $\mu$ -Trifluoroacetamido)Dirhodium(II)–Cytosine System. Crystal Structures of  $[\text{Rh}_2(\text{CF}_3\text{CONH})_4(\text{Cytosine})]$  and  $[\text{Rh}_2(\text{CF}_3\text{CONH})_4(1\text{-Methylcytosine})_2]\cdot 2\text{H}_2\text{O}$ . *Inorganica Chimica Acta* **2001**, *316* (1), 50–58.

- (42) Aoki, K.; Salam, Md. A. Interligand Interactions Affecting Specific Metal Bonding to Nucleic Acid Bases. A Case of [[Rh<sub>2</sub>(OAc)<sub>4</sub>]], [Rh<sub>2</sub>(HNOCCF<sub>3</sub>)<sub>4</sub>], and [Rh<sub>2</sub>(OAc)<sub>2</sub>(HNOCCF<sub>3</sub>)<sub>2</sub>] toward Purine Nucleobases and Nucleosides. *Inorganica Chimica Acta* **2002**, *339*, 427–437.
- (43) Chifotides, H. T.; Koomen, J. M.; Kang, M.; Tichy, S. E.; Dunbar, K. R.; Russell, D. H. Binding of DNA Purine Sites to Dirhodium Compounds Probed by Mass Spectrometry. *Inorg. Chem.* **2004**, *43* (20), 6177–6187.
- (44) Dunham, S. U.; Chifotides, H. T.; Mikulski, S.; Burr, A. E.; Dunbar, K. R. Covalent Binding and Interstrand Cross-Linking of Duplex DNA by Dirhodium(II,II) Carboxylate Compounds. *Biochemistry* **2005**, *44* (3), 996–1003.
- (45) Doyle, M. P.; Protopopova, M. N. New Aspects of Catalytic Asymmetric Cyclopropanation. *Tetrahedron* **1998**, *54* (28), 7919–7946.
- (46) Davies, H. M. L.; Liao, K. Dirhodium Tetracarboxylates as Catalysts for Selective Intermolecular C–H Functionalization. *Nat. Rev. Chem.* **2019**, *3* (6), 347–360.
- (47) Keipour, H.; Carreras, V.; Ollevier, T. Recent Progress in the Catalytic Carbene Insertion Reactions into the Silicon–Hydrogen Bond. *Org. Biomol. Chem.* **2017**, *15* (26), 5441–5456.
- (48) Ford, A.; Miel, H.; Ring, A.; Slattery, C. N.; Maguire, A. R.; McKerverey, M. A. Modern Organic Synthesis with  $\alpha$ -Diazocarbonyl Compounds. *Chem. Rev.* **2015**, *115* (18), 9981–10080.
- (49) Maas, G. New Syntheses of Diazo Compounds. *Ang. Chem. Int. Ed.* **2009**, *48* (44), 8186–8195.
- (50) Wong, F. M.; Wang, J.; Hengge, A. C.; Wu, W. Mechanism of Rhodium-Catalyzed Carbene Formation from Diazo Compounds. *Org. Lett.* **2007**, *9* (9), 1663–1665.
- (51) Timmons, D. J.; Doyle, M. P. Chiral Dirhodium(II) Catalysts and Their Applications. In *Multiple Bonds Between Metal Atoms*; Cotton, F. A., Murillo, C. A., Walton, R. A., Eds.; Springer US: Boston, MA, 2005; 591–632.
- (52) Davies, H. M. L.; Bruzinski, P. R.; Lake, D. H.; Kong, N.; Fall, M. J. Asymmetric Cyclopropanations by Rhodium(II) N-(Arylsulfonyl)Prolinate

- Catalyzed Decomposition of Vinylidiazomethanes in the Presence of Alkenes. Practical Enantioselective Synthesis of the Four Stereoisomers of 2-Phenylcyclopropan-1-Amino Acid. *J. Am. Chem. Soc.* **1996**, *118* (29), 6897–6907.
- (53) Doyle, M. P.; Peterson, C. S.; Protopopova, M. N.; Marnett, A. B.; Parker, Dann L.; Ene, D. G.; Lynch, V. Macrocyclic Formation by Catalytic Intramolecular Cyclopropanation. A New General Methodology for the Synthesis of Macrolides. *J. Am. Chem. Soc.* **1997**, *119* (38), 8826–8837.
- (54) Harding, M. M.; Nowicki, M. W.; Walkinshaw, M. D. Metals in Protein Structures: A Review of Their Principal Features. *Crystallography Reviews* **2010**, *16* (4), 247–302.
- (55) Marzo, T.; Ferraro, G.; Merlino, A.; Messori, L. Protein Metalation by Inorganic Anticancer Drugs. In *Encyclopedia of Inorganic and Bioinorganic Chemistry*; John Wiley & Sons, Ltd, 2020; 1–17.
- (56) Fukumoto, K.; Onoda, A.; Mizohata, E.; Bocola, M.; Inoue, T.; Schwaneberg, U.; Hayashi, T. Rhodium-Complex-Linked Hybrid Biocatalyst: Stereo-Controlled Phenylacetylene Polymerization within an Engineered Protein Cavity. *ChemCatChem* **2014**, *6* (5), 1229–1235.
- (57) Wilson, M. E.; Whitesides, G. M. Conversion of a Protein to a Homogeneous Asymmetric Hydrogenation Catalyst by Site-Specific Modification with a Diphosphinerhodium(I) Moiety. *J. Am. Chem. Soc.* **1978**, *100* (1), 306–307.
- (58) Hyster, T. K.; Knörr, L.; Ward, T. R.; Rovis, T. Biotinylated Rh(III) Complexes in Engineered Streptavidin for Accelerated Asymmetric C–H Activation. *Science* **2012**, *338* (6106), 500–503.
- (59) Monti, D. M.; Ferraro, G.; Merlino, A. Ferritin-Based Anticancer Metallodrug Delivery: Crystallographic, Analytical and Cytotoxicity Studies. *Nanomedicine: Nanotech., Biol. Med.* **2019**, *20*, 101997.
- (60) Park, C. R.; Kim, H. Y.; Song, M. G.; Lee, Y.-S.; Youn, H.; Chung, J.-K.; Cheon, G. J.; Kang, K. W. Efficacy and Safety of Human Serum Albumin–Cisplatin Complex in U87MG Xenograft Mouse Models. *Int. J. Mol. Sci.* **2020**, *21* (21), 7932.

- (61) Arnesano, F.; Natile, G. “Platinum on the Road”: Interactions of Antitumoral Cisplatin with Proteins. *Pur. Appl. Chem.* **2008**, *80* (12), 2715–2725.
- (62) Rilak Simović, A.; Masnikosa, R.; Bratsos, I.; Alessio, E. Chemistry and Reactivity of Ruthenium(II) Complexes: DNA/Protein Binding Mode and Anticancer Activity Are Related to the Complex Structure. *Coord. Chem. Rev.* **2019**, *398*, 113011.
- (63) Das, D.; Dutta, S.; Dowerah, D.; Deka, R. C. Unveiling the Role of Hydrogen Bonding and G-Tensor in the Interaction of Ru-Bis-DMSO with Amino Acid Residue and Human Serum Albumin. *J. Phys. Chem. B* **2020**, *124* (30), 6459–6474.
- (64) Cetinbas, N.; Webb, M. I.; Dubland, J. A.; Walsby, C. J. Serum-Protein Interactions with Anticancer Ru(III) Complexes KP1019 and KP418 Characterized by EPR. *J. Biol. Inorg. Chem.* **2010**, *15* (2), 131–145.
- (65) Dieterich, D. C.; Link, A. J. Click Chemistry in Protein Engineering, Design, Detection and Profiling. In *Click Chemistry for Biotechnology and Materials Science*; Lahann, J., Ed.; John Wiley & Sons, Ltd: Chichester, UK, 2009; 309–325.
- (66) Merlino, A. Recent Advances in Protein Metalation: Structural Studies. *Chem. Commun.* **2021**, *57* (11), 1295–1307.
- (67) Sullivan, M. P.; Groessl, M.; Meier, S. M.; Kingston, R. L.; Goldstone, D. C.; Hartinger, C. G. The Metalation of Hen Egg White Lysozyme Impacts Protein Stability as Shown by Ion Mobility Mass Spectrometry, Differential Scanning Calorimetry, and X-Ray Crystallography. *Chem. Commun.* **2017**, *53* (30), 4246–4249.
- (68) Krauss, I. R.; Messori, L.; Cinellu, M. A.; Marasco, D.; Sirignano, R.; Merlino, A. Interactions of Gold-Based Drugs with Proteins: The Structure and Stability of the Adduct Formed in the Reaction between Lysozyme and the Cytotoxic Gold(III) Compound Auoxo3. *Dalton Trans.* **2014**, *43* (46), 17483–17488.
- (69) Russo Krauss, I.; Ferraro, G.; Merlino, A. Cisplatin–Protein Interactions: Unexpected Drug Binding to N-Terminal Amine and Lysine Side Chains. *Inorg. Chem.* **2016**, *55* (16), 7814–7816.

- (70) Fitriyanto, N. A.; Fushimi, M.; Matsunaga, M.; Pertiwinigrum, A.; Iwama, T.; Kawai, K. Molecular Structure and Gene Analysis of  $Ce^{3+}$ -Induced Methanol Dehydrogenase of Bradyrhizobium Sp. MAFF211645. *J. Bioscience and Bioeng.* **2011**, *111* (6), 613–617.
- (71) Loreto, D.; Ferraro, G.; Merlino, A. Protein-Metallodrugs Interactions: Effects on the Overall Protein Structure and Characterization of Au, Ru and Pt Binding Sites. *International Journal of Biological Macromolecules* **2020**, *163*, 970–976.
- (72) Wong, D. L.; Stillman, M. J. Destructive Interactions of Dirhodium(II) Tetraacetate with  $\beta$  Metallothionein Rh1a. *Chem. Commun.* **2016**, *52* (33), 5698–5701.
- (73) Scheller, J. S.; Irvine, G. W.; Stillman, M. J. Unravelling the Mechanistic Details of Metal Binding to Mammalian Metallothioneins from Stoichiometric, Kinetic, and Binding Affinity Data. *Dalton Trans.* **2018**, *47* (11), 3613–3637.
- (74) Wong, D. L.; Stillman, M. J. Metallothionein: An Aggressive Scavenger—The Metabolism of Rhodium(II) Tetraacetate ( $Rh_2(CH_3CO_2)_4$ ). *ACS Omega* **2018**, *3* (11), 16314–16327.
- (75) Trynda-Lemiesz, L.; Pruchnik, F. P. Studies on the Interaction between Human Serum Albumin and  $[Rh_2(OAc)_2(Bpy)_2(H_2O)_2](OAc)_2$ . *Journal of Inorganic Biochemistry* **1997**, *66* (3), 187–192.
- (76) Jalilehvand, F.; Enriquez Garcia, A.; Niksirat, P.; Finfrook, Y. Z.; Gelfand, B. S. Binding of Histidine and Human Serum Albumin to Dirhodium(II) Tetraacetate. *J. Inorg. Biochem.* **2021**, *224*, 111556.
- (77) Chen, J.; Kostic, N. M. Binuclear Transition-Metal Complexes as New Reagents for Selective Cross-Linking of Proteins. Coordination of Cytochrome c to Dirhodium(II)- $\mu$ -Tetraacetate. *Inorg. Chem.* **1988**, *27* (15), 2682–2687.
- (78) Zhao, J.; Bachmann, D. G.; Lenz, M.; Gillingham, D. G.; Ward, T. R. An Artificial Metalloenzyme for Carbene Transfer Based on a Biotinylated Dirhodium Anchored within Streptavidin. *Catal. Sci. Technol.* **2018**, *8* (9), 2294–2298.
- (79) Srivastava, P.; Yang, H.; Ellis-Guardiola, K.; Lewis, J. C. Engineering a Dirhodium Artificial Metalloenzyme for Selective Olefin Cyclopropanation. *Nat.*

*Commun.* **2015**, *6* (1), 7789.

(80) Upp, D. M.; Huang, R.; Li, Y.; Bultman, M. J.; Roux, B.; Lewis, J. C. Engineering Dirhodium Artificial Metalloenzymes for Diazo Coupling Cascade Reactions. *Angew. Chem. Int. Ed.* **2021**, *60* (44), 23672–23677.

(81) Ferraro, G.; Pratesi, A.; Messori, L.; Merlino, A. Protein Interactions of Dirhodium Tetraacetate: A Structural Study. *Dalton Trans.* **2020**, *49* (8), 2412–2416.

(82) Abe, S.; Ueno, T. Design of Protein Crystals in the Development of Solid Biomaterials. *RSC Adv.* **2015**, *5* (27), 21366–21375.

(83) Margolin, A. L.; Navia, M. A. Protein Crystals as Novel Catalytic Materials. *Angew. Chem. Int. Ed. Engl.* **2001**, *40* (12), 2204–2222.

(84) Krauss, I. R.; Ferraro, G.; Pica, A.; Márquez, J. A.; Helliwell, J. R.; Merlino, A. Principles and Methods Used to Grow and Optimize Crystals of Protein–Metallo drug Adducts, to Determine Metal Binding Sites and to Assign Metal Ligands. *Metallomics* **2017**, *9* (11), 1534–1547.

(85) Müller, I. Guidelines for the Successful Generation of Protein–Ligand Complex Crystals. *Acta. Crystallogr. D Struct. Biol.* **2017**, *73* (2), 79–92.

(86) Pontillo, N.; Pane, F.; Messori, L.; Amoresano, A.; Merlino, A. Cisplatin Encapsulation within a Ferritin Nanocage: A High-Resolution Crystallographic Study. *Chem. Commun.* **2016**, *52* (22), 4136–4139.

(87) Picone, D.; Donnarumma, F.; Ferraro, G.; Gotte, G.; Fagagnini, A.; Butera, G.; Donadelli, M.; Merlino, A. A Comparison Study on RNase A Oligomerization Induced by Cisplatin, Carboplatin and Oxaliplatin. *J. Inorg. Biochem.* **2017**, *173*, 105–112.

(88) Picone, D.; Donnarumma, F.; Ferraro, G.; Russo Krauss, I.; Fagagnini, A.; Gotte, G.; Merlino, A. Platinated Oligomers of Bovine Pancreatic Ribonuclease: Structure and Stability. *J. Inorg. Biochem.* **2015**, *146*, 37–43.

(89) Nguyen, T. K.; Pham, T. T.; Ueno, T. Engineering of Protein Crystals for Development of Bionanomaterials. *Jpn. J. Appl. Phys.* **2019**, *58* (SI), SI0802.

(90) Yan, E.-K.; Cao, H.-L.; Zhang, C.-Y.; Lu, Q.-Q.; Ye, Y.-J.; He, J.; Huang, L.-J.; Yin, D.-C. Cross-Linked Protein Crystals by Glutaraldehyde and Their

Applications. *RSC Adv.* **2015**, *5* (33), 26163–26174.

(91) Richards, F. M.; Knowles, J. R. Glutaraldehyde as a Protein Cross-Linkage Reagent. *J. Mol. Biol.* **1968**, *37* (1), 231–233.

(92) Khalaf, N.; Govardhan, C. P.; Lalonde, J. J.; Persichetti, R. A.; Wang, Y.-F.; Margolin, A. L. Cross-Linked Enzyme Crystals as Highly Active Catalysts in Organic Solvents. *J. Am. Chem. Soc.* **1996**, *118* (23), 5494–5495.

(93) Carlsson, J.; Drevin, H.; Axén, R. Protein Thiolation and Reversible Protein-Protein Conjugation. N-Succinimidyl 3-(2-Pyridyldithio)Propionate, a New Heterobifunctional Reagent. *Biochem. J.* **1978**, *173* (3), 723–737.

(94) Thust, M.; Schöning, M. J.; Schroth, P.; Malkoc, Ü.; Dicker, C. I.; Steffen, A.; Kordos, P.; Lüth, H. Enzyme Immobilisation on Planar and Porous Silicon Substrates for Biosensor Applications. *J. Mol. Cat. B: Enzymatic* **1999**, *7* (1), 77–83.

(95) Govardhan, C. P. Crosslinking of Enzymes for Improved Stability and Performance. *Current Opinion in Biotechnology* **1999**, *10* (4), 331–335.

(96) Migneault, I.; Dartiguenave, C.; Bertrand, M. J.; Waldron, K. C. Glutaraldehyde: Behavior in Aqueous Solution, Reaction with Proteins, and Application to Enzyme Crosslinking. *BioTechniques* **2004**, *37* (5), 790–802.

(97) Salem, M.; Mauguén, Y.; Prangé, T. Revisiting Glutaraldehyde Cross-Linking: The Case of the Arg-Lys Intermolecular Doublet. *Acta. Crystallogr. Sect. F Struct. Biol. Cryst. Commun.* **2010**, *66* (3), 225–228.

(98) Lusty, C. J. A Gentle Vapor-Diffusion Technique for Cross-Linking of Protein Crystals for Cryocrystallography. *J. Appl. Cryst.* **1999**, *32* (1), 106–112.

(99) Persichetti, R. A.; Lalonde, J. J.; Govardhan, C. P.; Khalaf, N. K.; Margolin, A. L. Candida Rugosa Lipase: Enantioselectivity Enhancements in Organic Solvents. *Tetrahedron Lett.* **1996**, *37* (36), 6507–6510.

(100) Vilenchik, L. Z.; Griffith, J. P.; St. Clair, N.; Navia, M. A.; Margolin, A. L. Protein Crystals as Novel Microporous Materials. *J. Am. Chem. Soc.* **1998**, *120* (18), 4290–4294.

(101) St. Clair, N.; Wang, Y.-F.; Margolin, A. L. Cofactor-Bound Cross-Linked Enzyme Crystals (CLEC) of Alcohol Dehydrogenase. *Angew. Chem. Int. Ed.*

**2000**, *39* (2), 380–383.

(102) Tabe, H.; Abe, S.; Hikage, T.; Kitagawa, S.; Ueno, T. Porous Protein Crystals as Catalytic Vessels for Organometallic Complexes. *Chem. As. J.* **2014**, *9* (5), 1373–1378.

(103) Kowalski, A. E.; Johnson, L. B.; Dierl, H. K.; Park, S.; Huber, T. R.; Snow, C. D. Porous Protein Crystals as Scaffolds for Enzyme Immobilization. *Biomater. Sci.* **2019**, *7* (5), 1898–1904.

(104) Ueno, T.; Abe, S.; Koshiyama, T.; Ohki, T.; Hikage, T.; Watanabe, Y. Elucidation of Metal-Ion Accumulation Induced by Hydrogen Bonds on Protein Surfaces by Using Porous Lysozyme Crystals Containing RhIII Ions as the Model Surfaces. *Chem. Eur. J.* **2010**, *16* (9), 2730–2740.

(105) England, M. W.; Lambert, M. E.; Li, M.; Turyanska, L.; Patil, J. A.; Mann, S. Fabrication of Polypyrrole Nano-Arrays in Lysozyme Single Crystals. *Nanoscale* **2012**, *4* (21), 6710–6713.

(106) Wei, H.; Wang, Z.; Zhang, J.; House, S.; Gao, Y.-G.; Yang, L.; Robinson, H.; Tan, L. H.; Xing, H.; Hou, C.; Robertson, I. M.; Zuo, J.-M.; Lu, Y. Time-Dependent, Protein-Directed Growth of Gold Nanoparticles within a Single Crystal of Lysozyme. *Nature Nanotech* **2011**, *6* (2), 93–97.

(107) Abe, S.; Tsujimoto, M.; Yoneda, K.; Ohba, M.; Hikage, T.; Takano, M.; Kitagawa, S.; Ueno, T. Porous Protein Crystals as Reaction Vessels for Controlling Magnetic Properties of Nanoparticles. *Small* **2012**, *8* (9), 1314–1319.

(108) Abe, S.; Ijiri, H.; Negishi, H.; Yamanaka, H.; Sasaki, K.; Hirata, K.; Mori, H.; Ueno, T. Design of Enzyme-Encapsulated Protein Containers by In Vivo Crystal Engineering. *Adv. Mat.* **2015**, *27* (48), 7951–7956.

(109) Luiz de Mattos, I.; Lukachova, L. V.; Gorton, L.; Laurell, T.; Karyakin, A. A. Evaluation of Glucose Biosensors Based on Prussian Blue and Lyophilised, Crystalline and Cross-Linked Glucose Oxidases (CLEC®). *Talanta* **2001**, *54* (5), 963–974.

(110) Roy, J. J.; Abraham, T. E.; Abhijith, K. S.; Kumar, P. V. S.; Thakur, M. S. Biosensor for the Determination of Phenols Based on Cross-Linked Enzyme Crystals (CLEC) of Laccase. *Biosens. Bioelectr.* **2005**, *21* (1), 206–211.

- (111) Maity, B.; Taher, M.; Mazumdar, S.; Ueno, T. Artificial Metalloenzymes Based on Protein Assembly. *Coord. Chem. Rev.* **2022**, *469*, 214593.
- (112) Vaney, M. C.; Maignan, S.; Riès-Kautt, M.; Ducruix, A. High-Resolution Structure (1.33 Å) of a HEW Lysozyme Tetragonal Crystal Grown in the APCF Apparatus. Data and Structural Comparison with a Crystal Grown under Microgravity from SpaceHab-01 Mission. *Acta. Cryst. D* **1996**, *52* (3), 505–517.
- (113) Panzner, M. J.; Bilinovich, S. M.; Youngs, W. J.; Leeper, T. C. Silver Metallation of Hen Egg White Lysozyme: X-Ray Crystal Structure and NMR Studies. *Chem. Commun.* **2011**, *47* (46), 12479–12481.
- (114) Enriquez Garcia, A.; Jalilehvand, F.; Niksirat, P.; Gelfand, B. S. Methionine Binding to Dirhodium(II) Tetraacetate. *Inorg. Chem.* **2018**, *57* (20), 12787–12799.
- (115) Enriquez Garcia, A.; Jalilehvand, F.; Niksirat, P. Reactions of  $\text{Rh}_2(\text{CH}_3\text{COO})_4$  with Thiols and Thiolates: A Structural Study. *J. Synchrotron. Rad.* **2019**, *26* (2), 450–461.
- (116) Tabe, H.; Fujita, K.; Abe, S.; Tsujimoto, M.; Kuchimaru, T.; Kizaka-Kondoh, S.; Takano, M.; Kitagawa, S.; Ueno, T. Preparation of a Cross-Linked Porous Protein Crystal Containing Ru Carbonyl Complexes as a CO-Releasing Extracellular Scaffold. *Inorg. Chem.* **2015**, *54* (1), 215–220.
- (117) Brink, A.; Helliwell, J. R. Formation of a Highly Dense Tetra-Rhenium Cluster in a Protein Crystal and Its Implications in Medical Imaging. *IUCrJ* **2019**, *6* (4), 695–702.
- (118) Messori, L.; Marzo, T.; Sanches, R. N. F.; Hanif-Ur-Rehman; de Oliveira Silva, D.; Merlino, A. Unusual Structural Features in the Lysozyme Derivative of the Tetrakis(Acetato)Chloridodiruthenium(II,III) Complex. *Angew. Chem. Int. Ed.* **2014**, *53* (24), 6172–6175.
- (119) Ball, Z. T. Designing Enzyme-like Catalysts: A Rhodium(II) Metallopeptide Case Study. *Acc. Chem. Res.* **2013**, *46* (2), 560–570.
- (120) Liu, J.; Groszewicz, P. B.; Wen, Q.; Thankamony, A. S. L.; Zhang, B.; Kunz, U.; Sauer, G.; Xu, Y.; Gutmann, T.; Buntkowsky, G. Revealing Structure Reactivity Relationships in Heterogenized Dirhodium Catalysts by Solid-State NMR Techniques. *J. Phys. Chem. C* **2017**, *121* (32), 17409–17416.

- (121) Lou, Y.; Remarchuk, T. P.; Corey, E. J. Catalysis of Enantioselective [2+1]-Cycloaddition Reactions of Ethyl Diazoacetate and Terminal Acetylenes Using Mixed-Ligand Complexes of the Series  $Rh_2(RCO_2)_n$  ( $L^*_{4-n}$ ). Stereochemical Heuristics for Ligand Exchange and Catalyst Synthesis. *J. Am. Chem. Soc.* **2005**, *127* (41), 14223–14230.
- (122) Vitagliano, L.; Merlino, A.; Zagari, A.; Mazzarella, L. Reversible Substrate-Induced Domain Motions in Ribonuclease A. *Proteins* **2002**, *46*, 97–104.
- (123) Chifotides, H. T.; Dunbar, K. R. Interactions of Metal–Metal-Bonded Antitumor Active Complexes with DNA Fragments and DNA. *Acc. Chem. Res.* **2005**, *38* (2), 146–156.
- (124) Aguirre, J. D.; Angeles-Boza, A. M.; Chouai, A.; Pellois, J.-P.; Turro, C.; Dunbar, K. R. Live Cell Cytotoxicity Studies: Documentation of the Interactions of Antitumor Active Dirhodium Compounds with Nuclear DNA. *J. Am. Chem. Soc.* **2009**, *131* (32), 11353–11360.
- (125) Trindade, A. F.; Coelho, J. A. S.; Afonso, C. A. M.; Veiros, L. F.; Gois, P. M. P. Fine Tuning of Dirhodium(II) Complexes: Exploring the Axial Modification. *ACS Catal.* **2012**, *2* (3), 370–383.
- (126) Laconsay, C. J.; Pla-Quintana, A.; Tantillo, D. J. Effects of Axial Solvent Coordination to Dirhodium Complexes on the Reactivity and Selectivity in C–H Insertion Reactions: A Computational Study. *Organometallics* **2021**, *40* (24), 4120–4132.
- (127) Ohnishi, R.; Ohta, H.; Mori, S.; Hayashi, M. Cationic Dirhodium Complexes Bridged by 2-Phosphinopyridines Having an Exquisitely Positioned Axial Shielding Group: A Molecular Design for Enhancing the Catalytic Activity of the Dirhodium Core. *Organometallics* **2021**, *40* (15), 2678–2690.
- (128) Loreto, D.; Merlino, A. The Interaction of Rhodium Compounds with Proteins: A Structural Overview. *Coor. Chem. Rev.* **2021**, *442*, 213999.
- (129) Telser, J.; Drago, R. S. Reactions of Rhodium Trifluoroacetate with Various Lewis Bases. Formation of 4:1 Complexes with Pyridine and Tert-Butyl Isocyanide and Bond Cleavage with Phosphorus Donors. *Inorg. Chem.* **1984**, *23* (17), 2599–2606.

- (130) Webb, T. R.; Dong, T. Y. Solution Chemistry of Molybdenum(II) Trifluoroacetate. *Inorg. Chem.* **1982**, *21* (1), 114–116.
- (131) Himo, F. Recent Trends in Quantum Chemical Modeling of Enzymatic Reactions. *J. Am. Chem. Soc.* **2017**, *139* (20), 6780–6786.
- (132) Siegbahn, P. E. M.; Himo, F. The Quantum Chemical Cluster Approach for Modeling Enzyme Reactions. *WIREs Comput. Mol. Sci.* **2011**, *1* (3), 323–336.
- (133) Fedorov, A. A.; Joseph-McCarthy, D.; Fedorov, E.; Sirakova, D.; Graf, I.; Almo, C.S. Ionic Interactions in Crystalline Bovine Pancreatic Ribonuclease A. *Biochem.* **1996**, *35* (50), 15962-15979.
- (134) Prats-Ejarque, G.; Blanco, J. A.; Salazar, V. A.; Nogués, V. M.; Moussaoui, M.; Boix, E. Characterization of an RNase with Two Catalytic Centers. Human RNase6 Catalytic and Phosphate-Binding Site Arrangement Favors the Endonuclease Cleavage of Polymeric Substrates. *Biochim. Biophys. Acta (BBA) – Gen. Sub.* **2019**, *1863* (1), 105–117.
- (135) Rosenberg, M. L.; Krivokapic, A.; Tilset, M. Highly Cis-Selective Cyclopropanations with Ethyl Diazoacetate Using a Novel Rh(I) Catalyst with a Chelating N-Heterocyclic Iminocarbene Ligand. *Org. Lett.* **2009**, *11* (3), 547–550.
- (136) Davies, H. M. L.; Panaro, S. A. Effect of Rhodium Carbenoid Structure on Cyclopropanation Chemoselectivity. *Tetrahedron* **2000**, *56* (28), 4871–4880.
- (137) Otwinowski, Z.; Minor, W. [20] Processing of X-Ray Diffraction Data Collected in Oscillation Mode. In *Method in Enzymology; Macromolecular Crystallography Part A*; Academic Press, 1997; Vol. 276, 307–326.
- (138) Battye, T. G. G.; Kontogiannis, L.; Johnson, O.; Powell, H. R.; Leslie, A. G. W. IMOSFLM: A New Graphical Interface for Diffraction-Image Processing with MOSFLM. *Acta Cryst. D* **2011**, *67* (4), 271–281.
- (139) Vonrhein, C.; Flensburg, C.; Keller, P.; Sharff, A.; Smart, O.; Paciorek, W.; Womack, T.; Bricogne, G. Data Processing and Analysis with the AutoPROC Toolbox. *Acta Cryst. D* **2011**, *67* (4), 293–302.
- (140) McCoy, A. J.; Grosse-Kunstleve, R. W.; Adams, P. D.; Winn, M. D.; Storoni, L. C.; Read, R. J. Phaser Crystallographic Software. *J. Appl. Cryst.* **2007**, *40* (4), 658–674.

- (141) Murshudov, G. N.; Vagin, A. A.; Dodson, E. J. Refinement of Macromolecular Structures by the Maximum-Likelihood Method. *Acta Cryst. D* **1997**, *53* (3), 240–255.
- (142) Emsley, P.; Cowtan, K. Coot: Model-Building Tools for Molecular Graphics. *Acta Cryst. D Biol. Cryst.* **2004**, *60* (Pt 12 Pt 1), 2126–2132.
- (143) Evans, P. R.; Murshudov, G. N. How Good Are My Data and What Is the Resolution? *Acta Cryst. D* **2013**, *69* (7), 1204–1214.
- (144) Frisch, M. J.; Trucks, G. W.; Schlegel, H. B.; Scuseria, G. E.; Robb, M. A.; Cheeseman, J. R.; Scalmani, G.; Barone, V.; Petersson, G. A.; Nakatsuji, H.; Li, X.; Caricato, M.; Marenich, A. V.; Bloino, J.; Janesko, B. G.; Gomperts, R.; Mennucci, B.; Hratchian, H. P.; Ortiz, J. V.; Izmaylov, A. F.; Sonnenberg, J. L.; Williams-Young, D.; Ding, F.; Lipparini, F.; Egidi, F.; Goings, J.; Peng, B.; Petrone, A.; Henderson, T.; Ranasinghe, D.; Zakrzewski, V. G.; Gao, J.; Rega, N.; Zheng, G.; Liang, W.; Hada, M.; Ehara, M.; Toyota, K.; Fukuda, R.; Hasegawa, J.; Ishida, M.; Nakajima, T.; Honda, Y.; Kitao, O.; Nakai, H.; Vreven, T.; Throssell, K.; Montgomery, J. A. Jr., Peralta, J. E.; Ogliaro, F.; Bearpark, M. J.; Heyd, J. J.; Brothers, E. N.; Kudin, K. N.; Staroverov, V. N.; Keith, T. A.; Kobayashi, R.; Normand, J.; Raghavachari, K.; Rendell, A. P.; Burant, J. C.; Iyengar, S. S.; Tomasi, J.; Cossi, M.; Millam, J. M.; Klene, M.; Adamo, C.; Cammi, R.; Ochterski, J. W.; Martin, R. L.; Morokuma, K.; Farkas, O.; Foresman, J. B.; Fox, D. J.; -Gaussian 16. 2016.
- (145) Becke, A. D. A New Mixing of Hartree–Fock and Local Density-functional Theories. *J. Chem. Phys.* **1993**, *98* (2), 1372–1377.
- (146) Lee, C.; Yang, W.; Parr, R. G. Development of the Colle-Salvetti Correlation-Energy Formula into a Functional of the Electron Density. *Phys. Rev. B* **1988**, *37* (2), 785–789.
- (147) Becke, A. D.; Johnson, E. R. A Simple Effective Potential for Exchange. *J. Chem. Phys.* **2006**, *124* (22), 221101.
- (148) Grimme, S.; Antony, J.; Ehrlich, S.; Krieg, H. A Consistent and Accurate Ab Initio Parametrization of Density Functional Dispersion Correction (DFT-D) for the 94 Elements H-Pu. *J. Chem. Phys.* **2010**, *132* (15), 154104.
- (149) Tomasi, J.; Mennucci, B.; Cammi, R. Quantum Mechanical Continuum

## REFERENCES

Solvation Models. *Chem. Rev.* **2005**, *105* (8), 2999–3094.